FACULTY OF MATHEMATICS AND PHYSICS
Charles University

DOCTORAL THESIS

Martin Rejhon

Point defects in materials for detection of X-ray and gamma radiation

Institute of Physics of Charles University

Prague 2019

I declare that I carried out this doctoral thesis independently, and only with the cited sources, literature and other professional sources.

I understand that my work relates to the rights and obligations under the Act No. 121/2000 Sb., the Copyright Act, as amended, in particular the fact that the Charles University has the right to conclude a license agreement on the use of this work as a school work pursuant to Section 60 subsection 1 of the Copyright Act.

In Prague date ....   signature: RNDr. Martin Rejhon

Název Práce: Bodové defekty v materiálech pro detekci Rentgenova a gama záření

Autor: Martin Rejhon

Katedra: Institute of Physics of Charles University

Školitel: prof. Ing. Jan Franc, DrSc., Fyzikální ústav Univerzity Karlovy

Abstrakt: Telurid kademnatý a jeho sloučeniny jsou vhodnými materiály pro výrobu detektorů rentgenového a gamma záření pracujících za pokojové teploty. Kvalita detektoru je ovlivněna nedokonalostí materiálu, jako jsou krystalové defekty a nečistoty. To vede k formování hlubokých hladin, které působí jako rekombinační a záchytná centra. Poté nahromaděný prostorový náboj na hlubokých hladinách ovlivňuje elektrické a spektroskopické vlastnosti detektoru. Což v konečném důsledku může vést k polarizačnímu efektu, kdy elektrické pole je lokalizováno v blízkosti jednoho kontaktu a detekční vlastnosti jsou snížené.

Tato práce se zabývá komplexním studiem pásové struktury detektoru za pomoci rozlišných metod se zaměřením na rozdílnosti mezi CdTe, CdZnTe, CdTeSe a CdZnTeSe. Elektro-optický Pockelsův jev je použit na zkoumaní vlivu osvětlení v rozmezí $900 - 1800$ nm na vnitřní elektrické pole. Teplotní a časové vývoje elektrického pole po zapnutí napětí nebo vypnutí přídavného světla o vlnové délce 940 nm byly změřeny k určení hlubokých hladiny odpovědných za dynamiku prostorového náboje.

Několik numerických simulací založených na řešení drift-difuzní rovnice a Poissonovy rovnice, zahrnující Shockley-Read-Hallův model bylo provedeno za účelem potvrzení našich závěrů.

Klíčová slova: Elektrooptický Pockelsův jev, detektor rentgenového a gamma záření, CdTe, hluboké hladiny

Title: Point defects in materials for detection of X-ray and gamma radiation

Author: Martin Rejhon

Department: Institute of Physics of Charles University

Supervisor: prof. Ing. Jan Franc, DrSc., Institute of Physics of Charles University

Abstract: Cadmium telluride and its compounds are suitable materials for production of X-ray and gamma-ray detectors working at room temperature. However, the detector quality is affected by material imperfections, such as crystal defects and impurities. It results into forming of deep levels which act as recombination and trapping centers. Then, the accumulated space charge at these deep levels influences electric and spectroscopic properties of the detector. In the end it may result in the polarization effect, when the electric field is localized in vicinity of one contact and detection properties are decreased.

This thesis reports a complex study of a detector band structure by various methods with focus on differences between CdTe, CdZnTe, CdTeSe and CdZnTeSe. The electro-optic Pockels effect is used to investigate the influence of the illumination in range $900 - 1800$ nm on the inner electric field. The temperature and time evolutions of the electric field after application of bias or switching of the additional light at 940 nm were measured to determine deep levels responsible for space charge dynamics.

Several numerical simulations based on solution of the drift-diffusion and Poisson equations, including the Shockley-Read-Hall model are performed in order to confirm our conclusions.

Keywords: Electro-optic Pockels effect, X-ray and gamma-ray detector, CdTe, deep levels

Contents

Introduction

CdTe and its alloys

Cadmium telluride (CdTe) is a direct-band-gap semiconductor of the II-VI group, which crystallizes in the cubic zinc-blende structure (Figure 1) with a lattice constant $a = 0.648$ nm. This material has become material of choice in applications such as room-temperature spectroscopic X-ray and gamma-ray detectors [2, 3], photovoltaics [4], security [5] and medicine [6]. It has been studied as an X-ray and gamma-ray detector since the 1960s [7] due to its promising properties such as a relatively high band-gap around 1.5 eV at room temperature [8], which keeps the signal-to-noise ratio low and a high average atomic number $Z = 50$ ($Z_{Cd} = 48$ and $Z_{Te} = 52$), which increases the probability of the photoelectric absorption of high energy radiation. The probability depends on the atomic number as $\approx Z^{4-5}$ [9]. The semi-insulating material with resistivity 10^9 Ωcm can be prepared by the suitable technological process of compensation of shallow defects. However, CdTe contains structural defects, impurities, and vacancies [10]. Trapping and recombination on these defects lead to a decreased value of the mobility-lifetime product. One of the main problems of CdTe is time instability under bias (polarization effect[1]) [11, 12]

Figure 1: Cubic zinc-blende structure. [1]

The ternary modifications $Cd_{1-x}Zn_x Te$ (CZT) and $CdTe_{1-x}Se_x$ (CTS) are formed by substituting Cd with zinc (Zn) and Te with selenium (Se), respectively. The addition of zinc leads to the increase of the energy band-gap (Figure 2). It makes CZT a more suitable material for room temperature radiation detectors due to the lower band-to band thermal generation of free electrons and holes that results in a lower leakage current, if the compensation of shallow defects is performed properly [13, 14]. Therefore, the CZT offers a higher resistivity and a lower dislocation density in comparison with CdTe. The lower leakage current allows the application of a higher voltage bias. Also, the CZT material does not exhibit the bias induced polarization effect. However, the segregation coefficient for zinc is greater than 1 [15], which implies the zinc concentration in CZT solid as a function of position. It causes variations of concentration of defects along the crystal growth axis which typically leads to the result that detector-grade material properties are achieved only in part of the crystal and a high cost of the fabricated detectors.

In order to enhance the yield of acceptable crystals for detector applications, Se is added to the CdTe lattice due to the segregation coefficient for Se that is close to 1 [16, 17]. It results in a more uniform crystal [18, 19], which is an advantage in comparison with CZT. Another advantage of CTS over CZT is the lower concentration of dislocations [16]. It was reported that the efficiency of solar
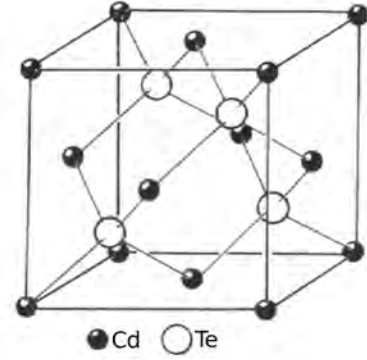
---

[1]More details in section 1.6

cells based on CdTe matrix is improved by adding of Se due to the passivation of critical defects in the bulk [20]. However, the energy band-gap decreases with a small concentration of Se which results in a higher dark current and therefore the signal-to-noise ratio is worse.

Recently, the quaternary modification $Cd_{1-x}Zn_xTe_{1-y}Se_y$ (CZTS) was prepared with a goal to obtain larger yield of high-quality material with comparable electrical and spectroscopic properties as CdTe and CZT materials and a potentially higher yield of spectroscopic material [21, 22, 23, 24].
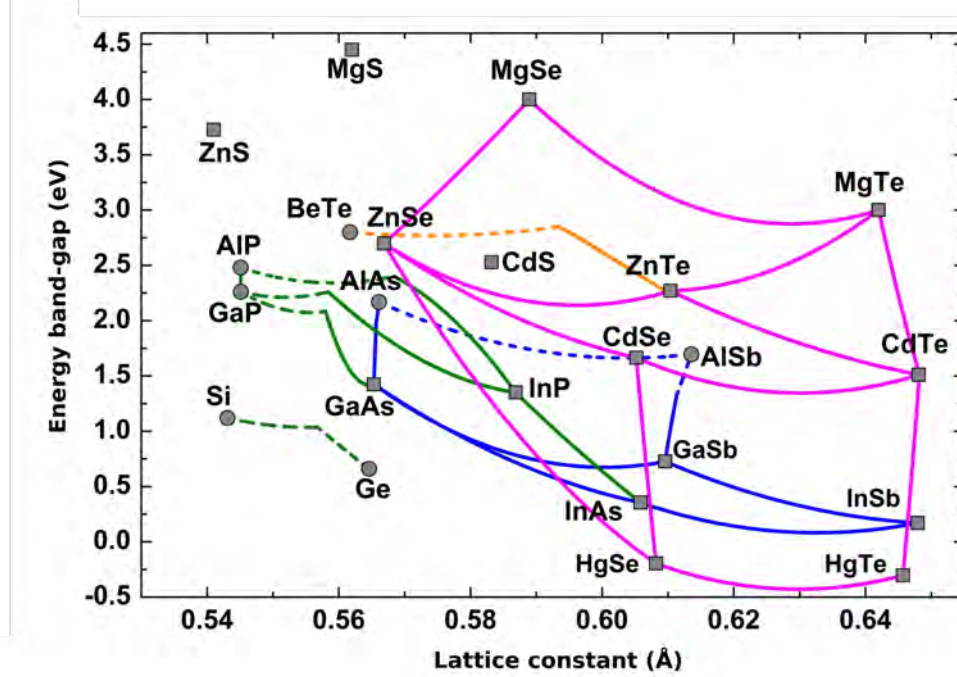
Figure 2: The energy band-gap versus lattice constant for common semiconductor materials and their compounds [25].

The Vertical High Pressure Bridgman Method (HPB), and Traveling Heater Method (THM) and Vertical Gradient Freeze Method (VGF) are the most used method for growing the CdTe material and its compounds [26, 27, 28, 29, 30, 31]. The crystals normally contain defects and impurities, which are formed during the growth process. These defects create shallow or deep levels inside the energy band-gap, which can act as donor or acceptor levels. The shallow levels are localized close to the valence or conduction band with activation energy comparable with the thermal energy kT. The deep levels are deeply positioned in the energy band-gap. They can act as a recombination or trap centers and strongly affect the electrical and optoelectrical properties of detectors.

Semiconductor detector

The simplest form of a semiconductor detector is represented by a slice of a homogeneous material with two planar electrodes. The incident X-ray photons are absorbed in the semiconductor and create electron-hole pairs. The external applied bias splits the pairs and forces the electrons and holes to drift towards

4

the electrodes. A material with a high mobility-lifetime ($\mu\tau$) product is required to eliminate the charge loss caused by trapping or recombination at deep levels during the drift.

The detector with a good performance is described by the following equation

$$t_d \ll \tau, \tag{1}$$

where t_d is the drift time of carriers and τ is the lifetime of carriers.

The carrier mobility μ and applied electric field $\mathbf{E}$ define the carrier velocity $\mathbf{v_d}$ by

$$\mathbf{v_d} = \mu\mathbf{E}. \tag{2}$$

Charge collection efficiency (CCE) is in the case of a constant electric field profile described by the Hecht equation [32]

$$CCE(\mathcal{E}) = \frac{Q}{Q_0} = \frac{\mu_e \tau_n \mathcal{E}}{d} \left[1 - \exp\left(-\frac{d-x}{\mu_e \tau_n \mathcal{E}} \right) \right]$$
$$+ \frac{\mu_h \tau_p \mathcal{E}}{d} \left[1 - \exp\left(-\frac{x}{\mu_p \tau_h \mathcal{E}} \right) \right], \tag{3}$$

where Q is the collected charge and Q_0 is the photogenerated charge, d is the distance between electrodes (detector thickness), x is the location of the creation of the electron-hole pair from the cathode, $\mu_{e,h}$ is the mobility of electrons respectively holes, $\tau_{n,p}$ is the lifetime of carriers and $\mathcal{E}$ is the intensity of the electric field.

In the case that the charge is generated in a vicinity of the cathode (case of α particle), the equation (3) can be rewritten as

$$CCE = \frac{\mu_e \tau_n \mathcal{E}}{d} \left[1 - \exp\left(-\frac{d-x}{\mu_e \tau_n \mathcal{E}} \right) \right]. \tag{4}$$

Here the $\mu\tau\mathcal{E}$ product describes the carrier drift length $\mathcal{L}$, which must be greater than the detector thickness to ensure complete charge collection required for good spectral resolution.

The detectors are mostly designed in special configurations that eliminate charge transport of holes and rely only on charge collection of electrons (coplanar grid, Frisch grid [33]). The reason is a low mobility of holes compared to electrons causing an increased trapping and recombination, which results in worsening of spectral resolution. In this case, the electric field is a function of the space coordinate x and equation (3) is not valid. Then the general form of the equation must be taken into the account [34, 35]

$$CCE = \frac{1}{d} \int_x^d \exp\left(-\int_x^{x_n} \frac{\mathrm{d}\xi}{\mu_e \tau_n \mathcal{E}(\xi)} \right) \mathrm{d}x_n$$
$$+ \frac{1}{d} \int_0^x \exp\left(-\int_{x_p}^x \frac{\mathrm{d}\xi}{\mu_p \tau_p \mathcal{E}(\xi)} \right) \mathrm{d}x_p, \tag{5}$$

where x_n (x_p) describes the distance of the electron (hole) from the anode.

Let us assume that a constant positive space charge is present in the sample. Then the electric field can be written in the linear form as

$$\mathcal{E} = \mathcal{E}_0 - as, \tag{6}$$

where s is the distance from the cathode and a is the slope of the electric field. Assuming that the electron-hole pairs are generated nearby the cathode and the holes are immediately extracted by the cathode, the CCE can be written as [34]

$$CCE(\mathcal{E}, a) = \begin{cases} 0 & \text{for } \pm a \leq 0 \text{ and } \mathcal{E} \leq \mathcal{E}_{th}, \\[2ex] \frac{1}{d}\frac{\mu\tau a}{\mu\tau a \pm 1}\sqrt{\frac{2\mathcal{E}d}{|a|}} & \text{for } \pm a > 0 \text{ and } \mathcal{E} \leq \mathcal{E}_{th}, \\[2ex] \frac{1}{d}\frac{\mu\tau a}{\mu\tau a \pm 1} \times \\ \left[\left(\frac{d}{2} \pm \frac{\mathcal{E}}{a}\right)\left(\frac{\pm\frac{\mathcal{E}}{a}-\frac{d}{2}}{\pm\frac{\mathcal{E}}{a}+\frac{L}{2}}\right)^{\pm\frac{1}{\mu\tau a}} + \frac{d}{2} \pm \frac{\mathcal{E}}{a}\right] & \text{for } \mathcal{E} > \mathcal{E}_{th}, \end{cases} \tag{7}$$

where $\mathcal{E}_{th}$ is defined as

$$\mathcal{E}_{th} = \frac{|a|d}{2}. \tag{8}$$

In summary, the room-temperature detector based on the semiconductor material must have relatively higher energy band-gap and high electric resistivity to decrease the thermal noise, which is critical for room temperature operation. The high resistivity material can be prepared by compensation of impurities and fixing the Fermi level E_F close to the mid-gap during crystal growth. The material with higher atomic number assures the higher probability of photoelectric absorption. Also an optimal choice of metal used for preparation of contacts can decrease the dark current by depletion of majority carriers (Schottky barrier) [36, 37].

Deep levels and spectroscopic methods used for their investigation

The electrical properties are affected by the presence of microscopic crystal defects. These defects, such as point, line, planar, and bulk defects, are formed during the crystal growth. This study is focused on the influence of point defects on detector properties. The point defects in the CdTe and its compounds generate deep levels in the energy band-gap. In general, it is desirable to minimize the concentration of deep levels and this way to decrease the trapping and recombination of photo-generated free carriers. However, a certain concentration of deep levels close to the mid-gap is necessary to stabilize the position of the Fermi level which leads to stable compensation conditions and high resistivity in the crystals.

In this section, the primary point defects and their deep levels are summarized as well as the experimental methods used for their investigation.

The deep levels can be investigated by many methods based on the measurement of the temperature dependence of current or/and capacitance time constant.

One of those methods is deep level transient spectroscopy (DLTS) [38, 39, 40, 41, 42], which is based on measurement of a capacitance response on voltage pulse in a wide temperature range (4 K-300 K). Other methods are photo-induced current transient spectroscopy (PICTS) [43, 44] and photoconductivity (PhC) [45], when a current change is forced by light and time and temperature (PICTS) or wavelength dependences (PhC) are measured. The thermoelectric effect spectroscopy (TEES) [46, 47, 48, 49, 50] applies measurement of electric current caused by temperature gradient in the sample. The discharge current measurements (DCM) [51] analyse electric current evolution after switching off the bias voltage. Other methods are based on measurement of spectral and temperature dependences of light emitted from material after excitation such as photoluminescence spectroscopy (PL) [38, 52, 53, 54]. There are many other techniques or modifications of the listed methods [55, 56, 57, 58, 59, 60, 61].

The point defects that influence charge transport in CdTe and related compounds are both native (vacancies and interstitials) as well as originating from foreign impurities (residual as well as intentionally introduced). Intentionally doping is done in order to prepare high resistive material. The goal is to achieve the state when the concentration difference of shallow donors and acceptors is compensated with the help of energy levels located close to mid-gap. This way the Fermi energy is fixed there and high resistivity state is reached [62, 63]. One of the most common point defects in CdTe lattice is cadmium vacancy V_{Cd}. This defect has two shallow levels at $E_t = 0.10$ eV [39, 46] and at $E_t = 0.21$ eV [47]. Also, the cadmium vacancy is responsible for two deep acceptor levels with activation energy $E_t = 0.40$ eV [39, 64, 48] and $E_t = 0.78$ eV [60, 10], respectively. Another native defect is cadmium interstitial Te_I, which forms donor levels with $E_t = 0.54$ eV [43] and $E_t = 0.64$ eV [39, 60]. The tellurium vacancy V_{Te} causes the donor level at $E_t = 1.10$ eV [39]. Summary of the most often observed levels is presented in Table 1.

Table 1: Summary of deep levels in CdTe material and its compounds.

E_t (eV)	Type	Origin	Method	Ref.
0.22	acceptor	In	DLTS	[40, 65]
0.26	acceptor	Au	PL	[53]
0.36	acceptor	Cu	PICTS	[43, 66]
0.39-0.43	donor	Te_{Cd}	TEES	[46]
0.40	donor	V_{Te}	DLTS, PICTS	[39, 48]
0.40	acceptor	V_{Cd}	theory	[64]
0.43-0.49	acceptor	Te_{Cd}-$2V_{Cd}$	TEES	[48]
0.50	donor	V_{Te}	theory	[67, 68]
0.54	donor	Cd_I	DLTS, PICTS	[39, 60]
0.68	acceptor	In	DLTS	[40]
0.73	acceptor	V_{Cd}	TEES	[49, 50]
0.73	donor	V_{Cd}	TEES	[47]
0.78	acceptor	V_{Cd}	PICTS	[60]
0.86	acceptor	In	DLTS	[40]
1.10	donor	V_{Te}	DLTS, PICTS	[39]
1.10	donor	dislocation	DLTS, PL	[69]

Motivation and goals

The detector materials based on CdTe and its compounds have been examined at the Institute of Physics of Charles University for many years. Many methods such as Hall-effect measurement, transient current technique, photoluminescence spectroscopy, Pockels effect measurement, etc. have been used to study commercial detectors and detector materials which were grown at our institute.

The electrical detector properties are affected by the deep levels as it is mentioned in previous sections. In order to understand the influence of deep levels, this thesis is primarily focused on evolution of electric field in the samples by measuring the time and temperature Pockels effect. The measurement of Pockels effect was performed after application of the bias (section 3.3.2) or after switching off the additional illumination at the wavelength of 940 nm (section 3.3.5). The measurement of I-V characteristics and ellipsometry measurements (section 3.1) were used to determine the resistivity of the samples, the influence of the metal-semiconductor interface and the energy band-gap.

This thesis aim is to increase our understanding of influence of deep levels on charge transport and detector performance and to search for differences among several CdTe based compounds (CdTe, CdZnTe, CdTeSe, CdZnTeSe). The work also included theoretical simulations using experimentally determined input data (section 3.4).

The set of 7 different samples (CdTe, CdZnTe, CdTeSe, CdZnTeSe) was investigated.

1. Theory

This section briefly summarizes the theory used in the thesis to evaluate the obtained experimental data and to numerically simulate influence of deep levels and metal contact properties on charge transport in CdTe based semiconductor detectors.

The solution of the Schrödinger equation in a one-electron approximation with periodical potential energy, which describes the periodicity of the lattice, gives information about the band structure of a solid crystalline [70, 71, 72].

The ideal semiconductor band structure is formed by the valence band (E_v), the conduction band (E_c) and the energy band-gap (E_G). The valence band is fully occupied by electrons and the conduction band is fully empty at absolute zero temperature. The energy band-gap describes the energetic range between the valence band and the conduction band that contains no energy states.

The detector properties are affected by the levels in the energy band-gap, which are formed due to the defects in the crystal matrix.

The probability that the energy level in the conduction band is occupied by an electron is described by Fermi-Dirac distribution function

$$f(E)_n = \frac{1}{1 + \exp\left(\frac{E - E_F}{k_B T}\right)} \tag{1.1}$$

where k_B is Boltzmann constant, T is the absolute temperature, and E_F is the Fermi energy. The definition of the Fermi level is based on fact that for $E = E_F$ the equation (1.1) is equal to $f(E) = 1/2$ regardless of the temperature.

The probability of occupation of an energy state in the valence band with a hole (missing electron) is described by a distribution

$$f(E)_p = 1 - f(E)_n = \frac{1}{1 + \exp\left(\frac{E_F - E}{k_B T}\right)}. \tag{1.2}$$

For the case that the Fermi level lies more than $3k_B T$ below the conduction band, the equation (1.1) can be simplified to the Boltzmann function

$$f(E)_n = \exp\left(-\frac{E - E_F}{k_B T}\right). \tag{1.3}$$

In this case, the electron density near the bottom of the conduction band is given by

$$n = N_c \exp\left(-\frac{E_c - E_F}{k_B T}\right). \tag{1.4}$$

Similarly, the hole density in the valence band can be calculated by

$$p = N_v \exp\left(-\frac{E_v - E_F}{k_B T}\right), \tag{1.5}$$

where N_c and N_v is the effective density of states in the conduction band and the effective density of states in the valence band, respectively.

$$N_{c/v} = 2\left(\frac{2\pi m_{e/h}^* k_B T}{h^2}\right)^{\frac{3}{2}}, \tag{1.6}$$

where h is the Planck constant, and m_e^* and m_h^* is the effective mass of electron in the conduction band and the effective mass of hole in the valence band, respectively. In the case of CdTe the m_e^* (m_h^*) equals to $0.096 m_e$ ($0.83 m_e$) [73]. Here m_e is the mass of a free electron.

1.1 Acceptors and Donors

The semiconductor can contain donor or acceptor levels in the energy band-gap. These levels are created in the semiconductor by doping with impurities. The shallow donor levels are located close to the conduction band and increase the number of electrons there by thermal emission at $T > 0$. Therefore, doping with donors causes a shift of the Fermi level closer to the conduction band. On the other hand, the acceptor levels increase the density of holes in the valence band, and the Fermi level is shifted towards the valence band. According to the position of the Fermi level, the semiconductor is called N-type or P-type semiconductor. The Fermi level is located above (below) the mid-gap for N-type (P-type).

The concentrations of donor and acceptor atoms are labelled as N_D and N_A, respectively. The probability of occupancy of the donor or acceptor levels by electron is given by

$$f(E_{D/A}) = \left[\frac{1}{g_{D/A}} \exp \left(\frac{E_{D/A} - E_F}{k_B T} \right) \right]^{-1}, \tag{1.7}$$

where $g_{D/A}$ is the degeneracy factor of donor or acceptor impurity level.

The concentration of donor (acceptor) atoms is equal to the sum of ionized N_D^+ (N_A^-) and non-ionized donor (acceptor) concentrations N_D^0 (N_A^0):

$$\begin{aligned} N_D &= N_D^+ + N_D^0, \\ N_A &= N_A^- + N_A^0. \end{aligned} \tag{1.8}$$

The degeneration factor is $g_D = 2$ for donor impurities due to the Pauli exclusion principle. The acceptor degeneration factor is $g_A = 4$ due to the Pauli exclusion principle and due to the fact that electron at the top of the valence band can occupy 4 positions - two with opposite spins in the heavy-holes band an two in the light-holes band. By considering that the equation (1.7) is equal to the ratio $N_{D/A}^0 / N_{D/A}$ and substituting the equation (1.7) in (1.8) the concentration of ionized donor/acceptor atoms can be computed by

$$\begin{aligned} N_D^+ &= N_D - N_D^0 = N_D(1 - f(E_D)) = N_D \frac{1}{1 + 2 \exp \left(\frac{E_F - E_D}{k_B T} \right)}, \\ N_A^- &= N_A - N_A^0 = N_A(1 - f(E_A)) = N_A \frac{1}{1 + 4 \exp \left(\frac{E_A - E_F}{k_B T} \right)}. \end{aligned} \tag{1.9}$$

The doped semiconductor must be charge neutral. Assuming the simple case of presence of one type of donors and acceptors in the material, the charge neutrality equation holds

$$n + N_A^- = p + N_D^+ \tag{1.10}$$

1.2 Drift-diffusion equation

If the electron concentration in the conduction band is n, the $\mathbf{E}$ is the electric field, T is the temperature and μ_e is the electron mobility, then the electron current density ($\mathbf{j_e}$) in the conduction band is described by the drift-diffusion equation

$$\mathbf{j_e} = e\mu_e n\mathbf{E} + \mu_e k_B T\nabla n + \mu_e k_B n\nabla T. \tag{1.11}$$

Similarly, the drift-diffusion equation can be written for the hole current density ($\mathbf{j_h}$)

$$\mathbf{j_h} = e\mu_h p\mathbf{E} - \mu_h k_B T\nabla p + \mu_h k_B p\nabla T, \tag{1.12}$$

where μ_p is the hole mobility and p is the hole concentration in the valence band.

The sum of the current densities is equal to the total density of the current at any point in the semiconductor

$$\mathbf{j} = \mathbf{j_e} + \mathbf{j_h}. \tag{1.13}$$

The semiconductor conductivity σ is connected with electron and hole mobility by the following equation

$$\sigma = e(n\mu_e + p\mu_h). \tag{1.14}$$

Therefore, the semiconductor resistivity ϱ is given by

$$\varrho = \frac{1}{\sigma} = \frac{1}{e(n\mu_e + p\mu_h)}. \tag{1.15}$$

Let us now analyse the equation (1.11). The first term $e\mu_e n\mathbf{E}$ corresponds with the drift of carries caused by an external bias and resulting electric field. The second and the third terms are related to the diffusion of free carriers from a place with a higher concentration toward a place with a lower concentration (2nd term) or from an area with a higher temperature to an area with a lower temperature (3rd term).

These equations (1.11) an (1.12) can be simplified for the case when the temperature is constant. Then the 3rd term equals zero and the equations are reduced to

$$\mathbf{j_e} = e\mu_e n\mathbf{E} + \mu_e k_B T\nabla n \tag{1.16}$$

and

$$\mathbf{j_h} = e\mu_h p\mathbf{E} - \mu_h k_B T\nabla p. \tag{1.17}$$

Let us now focus only on the drift term in equation (1.11) and let us assume a homogeneous semiconductor.

The applied electric field is described by

$$\mathbf{E} = -\nabla\phi. \tag{1.18}$$

Here ϕ is a scalar electrostatic potential. Considering the fact that the Lorentz force $\mathbf{F}$ in the absence of magnetic field causing the electron movement is given by

$$\mathbf{F} = -e\mathbf{E}, \tag{1.19}$$

the charge carriers drift to the place with a lower potential energy. Thus electrons move towards the anode and holes move towards the cathode.

The total energy of electron W is a sum of the kinetic energy and potential energy

$$\mathsf{W} = \frac{p_e^2}{2m_e^*} - eU, \tag{1.20}$$

where p_e is the electron momentum, m_e^* is the effective mass of electron, and U is the applied bias.

A homogeneous electric field $\mathcal{E} = U/d$ is formed in the homogeneous semiconductor with the length d due to the application of the bias U.
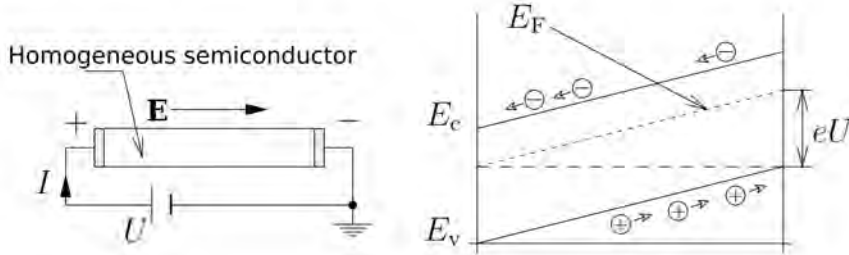
Figure 1.1: The scheme on the left shows the application of the bias on the homogeneous semiconductor. The tilted bands are depicted at the scheme on the right. The difference between the Fermi level position at the anode and at the cathode is given by the applied bias.

Figure 1.1 shows the application of the bias on the homogeneous semiconductor. The direction of the electric field vector $\mathbf{E}$ is from the anode $(+)$ towards the cathode $(-)$. The semiconductor bands are tilted because of the applied bias. The difference between the Fermi level position at the anode and the cathode is equal to the applied bias multiplied by elementary charge e

$$\Delta E_F = E_F(+) - E_F(-) = eU. \tag{1.21}$$

1.3 Poisson's equation

If a space charge is present in the semiconductor, the Poisson's equation must be taken into account:

$$\Delta\phi(x, y, z) = -\frac{\rho(x, y, z)}{\varepsilon}, \tag{1.22}$$

where ρ is a space charge density, and ε is the permittivity (a product of permittivity of vacuum ε_0 and the relative permittivity ε_r)

$$\varepsilon = \varepsilon_0 \varepsilon_r. \tag{1.23}$$

The space charge ρ is connected with the inner electric field $\mathbf{E}$ by the Gauss law

$$\nabla \cdot \mathbf{E}(x, y, z) = \frac{\rho(x, y, z)}{\varepsilon}. \tag{1.24}$$

The total space charge density in the semiconductor is given by the sum

$$\rho = -e(p - n - N_A^- + N_D^+). \qquad (1.25)$$

1.4 Shockley-Read-Hall model

The deep levels can act as recombination or trapping centers. The Shockley-Read-Hall model describes statistically the generation/recombination events in the semiconductor [74, 75].

The simplified scheme of a semiconductor with one deep level E_t is depicted in Figure 1.2. The model includes six generation/recombination processes. There are two direct transitions between the valence and the conduction band: electron-hole generation (1) and electron-hole recombination (6). Also, there are four transitions that include the deep level, which are capture of an electron (2), capture of a hole (3), de-trapping of an electron (4), and de-trapping of a hole (5).
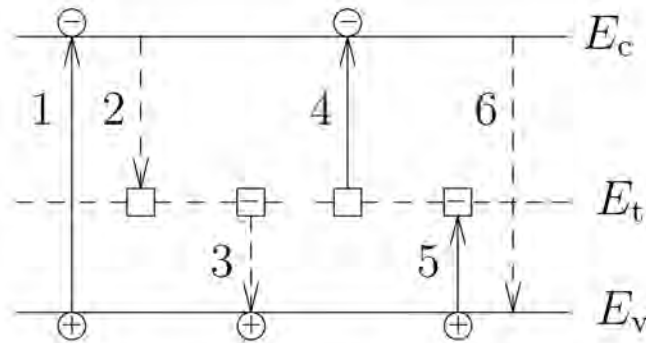
Figure 1.2: The Shockley-Read-Hall model of generation and recombination processes. electron-hole pairs generation (1); capture of electron (2); capture of hole (3); de-trapping of electron (4); de-trapping of hole (5); band-to-band recombination (6). [76]

The deep level E_t is described by following parameters: the total concentration of the deep level N_t, the capture cross sections σ_n and σ_p for electrons and holes, respectively, and the concentration of electrons n_t and of holes p_t on the deep level.

The sum of the electron concentration and the concentration of holes on the deep level E_t is equal to the total concentration of deep level

$$N_t = n_t + p_t \qquad (1.26)$$

The electron concentration n_t can be obtained from

$$n_t = \frac{N_t}{\exp\left(\frac{E_t - E_F}{k_B T}\right) + 1} \qquad (1.27)$$

Out of equilibrium, the time changes of the concentrations are described by the following equations

$$
\begin{aligned}
\frac{dn}{dt} &= G + \gamma_n n_t n_1 - \gamma_n (N_t - n_t), \\
\frac{dp}{dt} &= G + \gamma_p (N_t - n_t) p_1 - \gamma_p n_t p, \\
\frac{dn_t}{dt} &= \gamma_n (N_t - n_t) - \gamma_n n_t n_1 + \gamma_p (N_t - n_t) p_1 - \gamma_p n_t p.
\end{aligned}
\tag{1.28}
$$

Here G is the generation rate, γ_n is a coefficient that represents the probability of electron capture on the level. Similarly, γ_p is a coefficient that represents the probability of hole capture, and n_1 and p_1 are the equilibrium concentrations of electrons and holes, in the case when $E_F = E_t$.

The coefficient of the electron or hole capture probability on a deep level is given by

$$
\gamma_n = \sigma_n v_n \quad , \quad \gamma_p = \sigma_p v_p,
\tag{1.29}
$$

where v_n and v_p is thermal velocity of electrons and holes, respectively. Thermal velocity is given by

$$
v_{n/p} = \sqrt{\frac{8 k_B T}{\pi m_{e/h}^*}}.
\tag{1.30}
$$

The capture cross-sections are used to separate deep levels into three groups:

- $\sigma_n \approx \sigma_p \ldots$ recombination level

- $\sigma_n < \sigma_p \ldots$ hole trap

- $\sigma_n > \sigma_p \ldots$ electron trap

In the steady-state, the lifetime of free electrons τ_n and free holes τ_p in the conduction band and in the valence band is

$$
\tau_n = \frac{1}{\gamma_n (N_t - n_t)} \quad \text{and} \quad \tau_p = \frac{1}{\gamma_p (N_t - p_t)}, \text{ respectively.}
\tag{1.31}
$$

1.5 Optical absorption

The results of experimental methods that use light for excitation of the sample often critically depend on the absorption coefficient.

The absorption of light with intensity $\mathcal{I}_0$ is characterized by the Lambert-Beer law [77, 78]

$$
\mathcal{I}(x) = \mathcal{I}_0 \exp(-\alpha x),
\tag{1.32}
$$

where $\mathcal{I}(x)$ is the light intensity at the depth x from the surface, and α is the absorption coefficient, which depends on the material and the photon energy of incident light. The photon energy of the monochromatic light in electronvolts is given by

$$
E_{light}(\text{eV}) = h\nu \doteq \frac{1239}{\lambda(\text{nm})},
\tag{1.33}
$$

here ν is the photon frequency, and the λ is the wavelength.

In the case of the illumination of the semiconductor, the absorption depends on the photon energy of the incident light, band-gap energy and types of energy levels in the band-gap.

The incident light with photon energy above the semiconductor energy band-gap ($h\nu > E_G$) creates electron-hole pairs close to the surface, mostly in the distance of $1/\alpha$ (Figure 1.3(a)). In this thesis we apply in all cases illumination through the cathode. The applied electric field separates electron-hole pairs and holes immediately recombine on the cathode, while electrons drift toward the anode. They can be trapped at deep levels during the drift and affect the space charge distribution in the detector.

On the other hand, the photon energy of incident light below the energy band-gap ($h\nu < E_G$) penetrates though the material and electron-hole pairs are photo-generated in the whole volume (Figure 1.3(b)). In this case both electrons and holes drift toward the corresponding electrode and can be trapped at deep levels. The trapped charge can therefore be both positive or negative. Depending on the position of generation of free carriers and the parameters of deep levels including their equilibrium occupation, volumes with both types of space charge can be present even in a homogeneous sample. The space charge then modifies the internal electric field (Gauss law equation 1.24).
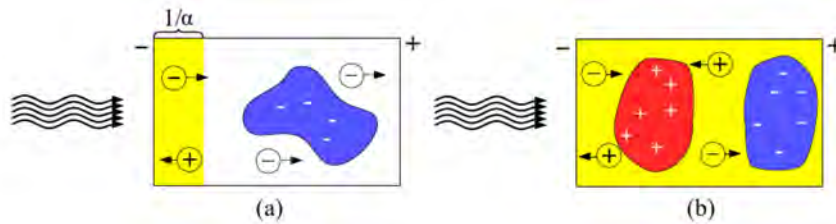
Figure 1.3: The scheme (a) shows the generation of electron-hole pairs by the photons with energy higher than energy band-gap ($h\nu > E_G$). Photons are mostly absorbed in the distance ($1/\alpha$) from the surface. In the case of the applied bias, the electron-hole pairs are separated and the carriers drift towards the corresponding electrode. The scheme (a) describes the illumination through the cathode. Holes immediately recombine at the cathode and electrons drift through the sample towards the anode. They can be trapped at deep levels and affect the space charge distribution in the detector. In the case of the illumination with photon energy lower than the energy band-gap ($h\nu < E_G$) (scheme (b)), the illumination penetrates into the material. It allows the interaction of the light with deep levels in the whole volume and the positive or negative space charge can be formed according to the nature of the photo-generated electron transitions.

1.6 Polarization effect on the inner electric field

The inner electric field is given by the distribution of the space charge in the semiconductor (eq. (1.24)). The space charge is proportional to the occupation of deep levels that can be affected by bending of the bands at the metal-semiconductor interfaces or by the capture of the photo-generated charge carriers. Both these processes could lead to the deformation of the electric field. If the space charge is high enough, the so-called dead layer can be formed, where the

electric field is close to zero. This effect is commonly called polarization of detector [79, 80, 81, 82].

The situation of non-polarized and polarized detector is depicted in Figure 1.4). The red line shows the polarized detector with strongly deformed electric field, when the dead layer is formed (area (a)). The electric field is concentrated in area (b). In this situation the charge collection efficiency (CCE) is decreased due to a strong trapping and recombination of free carriers during a very slow drift through the dead layer.
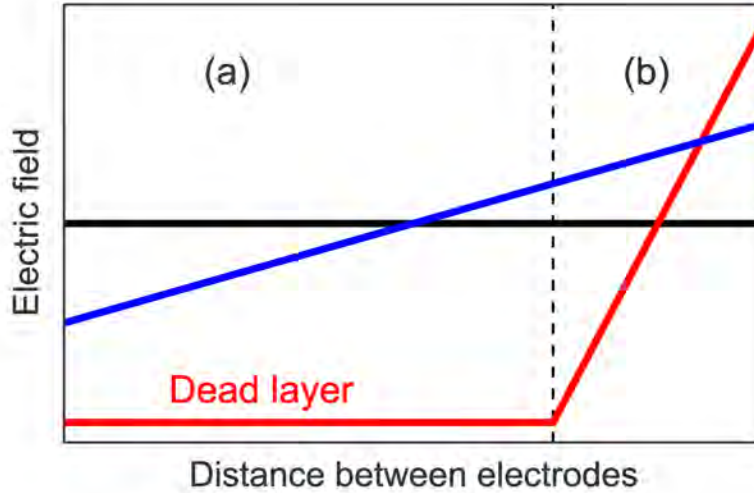
Figure 1.4: Black line shows a constant electric field profile corresponding to the sample without space charge. Blue line represents a linear profile when a constant space charge is present. The detector is slightly polarized. Red line shows a situation when the electric field is concentrated close to one of the electrodes (close to the cathode if the space charge is positive and close to the anode, if it is negative) which is a sign of strong polarization. This area (b) is called the depletion layer. The electric field in the area (a) is very small (close to zero), and this area is called the dead layer.

1.7 Evaluation of parameters of deep levels from temporal and temperature evolution of electric field profiles

In this thesis we present our modified approach for evaluation of parameters of deep levels analyzing the electric field profiles from Pockels effect measurements instead of measuring electric capacity or electric current. The advantage of the method is the simplicity of determination, whether the deep trap communicates with the conduction or valence band and the possibility to extract data from a homogeneous part of the sample. We present first the theoretical substantiation of the method.

The inner electric field profiles are mainly defined by the space charge localized on deep levels in the semi-insulating semiconductor (space charge originating from free carriers is negligible in equilibrium and at low illumination intensity). If the

dead layer is not formed and the electric field can be described by a linear profile (blue line in Figure 1.4), we can assume a homogeneous space charge density ρ in the sample. Then the electric field can be described as

$$\mathcal{E}(x) = \mathcal{E}(d) - \frac{\rho}{\varepsilon_0 \varepsilon_r}(d - x). \tag{1.34}$$

Here $\mathcal{E}(d)$ is the electric field at the cathode and d is the sample thickness. Assuming equation (1.25), the space charge density relates to deep levels occupation via the formula

$$\rho = e \sum_i (n_{t0i} - n_{ti}), \tag{1.35}$$

where n_{t0i} is the electron density on the i-th level in sample in thermodynamic equilibrium and n_{ti} is an actual electron density on the i-th level. Integrating equation (1.34) in x we obtain the final formula connecting the measured electric field at the cathode $\mathcal{E}(d)$ and level occupancies n_{ti} in the form

$$\mathcal{E}(d) = \frac{U}{d} + \frac{ed}{2\varepsilon_0 \varepsilon_r} \sum_i (n_{t0i} - n_{ti}). \tag{1.36}$$

U is the applied bias.

The investigation of space charge ρ time evolutions of dependence on temperature and bias allows to determine the properties of deep levels responsible for the space charge formation in the sample.

Generalizing Shockley-Read-Hall model (section 1.4), we can express the dynamics of the i-th level occupancy with the formulas

$$
\begin{aligned}
\frac{\partial n_{ti}}{\partial t} &= \sigma_{ni} v_e [(N_{ti} - n_{ti})n - n_{ti} n_{1i}] - \\
&\quad \sigma_{pi} v_h [n_{ti} p - (N_{ti} - n_{ti})p_{1i}] \\
&= -n_{ti}[\sigma_{ni} v_e(n_{1i} + n) + \sigma_{pi} v_h(p_{1i} + p)] + \\
&\quad N_{ti}(\sigma_{ni} v_e n + \sigma_{pi} v_h p_{1i}).
\end{aligned}
\tag{1.37}
\tag{1.38}
$$

Here the parameters of the model are the electron (hole) capture cross-section $\sigma_{n(p)i}$ and $n(p)_{1i} = N_{c(v)} \exp(-\frac{E_{ti}}{k_B T})$, where E_{ti} is the energy of the i-th trap measured from the conduction (valence) band.

The effective density of states for electrons (holes) in the conduction (valence) band is described with equation (1.6).

Let us focus on the term in square brackets and the follow-up term in equation (1.38), these terms are independent of n_{ti}. For that they may be taken as constant, and we may immediately write down the solution of equation(1.38) as

$$n_{ti}(t) = (n_{t0i} - n_{ti}(\infty)) \exp\left(-\frac{t}{\tau_i}\right) + n_{ti}(\infty), \tag{1.39}$$

where the relaxation time

$$\tau_i = [\sigma_{ni} v_e(n_{1i} + n) + \sigma_{pi} v_h(p_{1i} + p)]^{-1} \tag{1.40}$$

and the final level occupancy

$$n_{ti}(\infty) = N_{ti} \tau_i (\sigma_{ni} v_e n + \sigma_{pi} v_h p_{1i}). \tag{1.41}$$

Substituting equation (1.39) into equation (1.36) and measuring $\mathcal{E}(d)(t)$ in the dynamical regime at different T, we can apply conventional procedure to analyze thermally activation processes and identify properties of deep levels responsible for space charge changes. Neglecting free carriers density in the depleted sample and assuming that the deep levels trap dominantly only one type carriers, i.e. defining electron (hole) trap putting $\sigma_{p(n)} = 0$, the equations (1.40) and (1.41) can be simplified. Then, the relaxation rates describing the electron and hole trap τ_n and τ_p, respectively, can be described as

$$\tau_{ni}^{-1} = \sigma_{ni} v_e n_{1i} \tag{1.42}$$

$$\tau_{pi}^{-1} = \sigma_{pi} v_h p_{1i}. \tag{1.43}$$

Defining parameter $A_e = \sigma_n v_e N_c$ for an electron trap and $A_h = \sigma_p v_h N_v$ for a hole trap and neglecting one type of the deep level we can write common relaxation rate τ^{-1} in a form

$$\tau_{n(h)}^{-1} = A_{e(h)} \exp\left(-\frac{E_t}{k_B T}\right), \tag{1.44}$$

for the electron trap and the hole trap, respectively.

The linearization of equation(1.44) gives the Arrhenius equation

$$\ln(\tau_i T^2) = \frac{E_i}{k_B T} + \ln\left(\frac{C}{\sigma_i}\right). \tag{1.45}$$

Here σ_i is the capture cross-section, E_i is the energy of the i-th level and τ_i is the relaxation rate of i-th level. The constant C is equal to

$$C = \frac{h^3}{16 m_{e(h)}^* \pi k_B^2}. \tag{1.46}$$

This analysis allows us to determine the thermally activated transitions. Thermally activated transitions are transitions of electrons from the valence band to deep levels or from deep levels to the conduction band. Therefore the type of transition can be distinguished based on the sign of the change of the space charge. If the inner electric field under the cathode increases, it means that electron transitions from the deep level to the conduction band take place. These transitions cause the increase of the positive space charge (Figure 1.5(a)) or decrease of the initial negative space charge (Figure 1.5(b)). These situations are explained in Figure 1.5(c) with two types electron transitions. The first electron transition from the deep level to the conduction band is thermally activated and the second electron transition from the deep level to the valence band is not thermally activated. On the other hand, a decrease of the inner electric field under the cathode corresponds to thermally activated electron transitions from the valence band to the deep level (de-trapping of holes) or to the not thermally activated electron trapping from the conduction band to the deep level (Figure 1.5(d,e,f)).
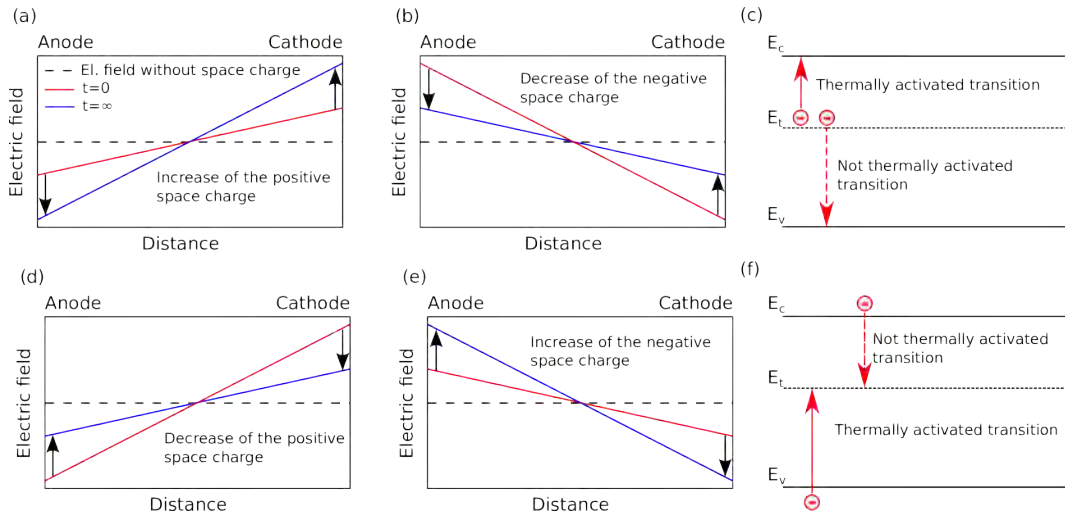
Figure 1.5: The graphs show the change of the electric field profiles in time. The dashed black line represents the electric field without a space charge. Graph (a) exhibits situation with positive space charge when the electric field increases from the anode to the cathode and its evolution shows an increase of the positive space charge. This corresponds to transitions of electrons from a deep level to the conduction band (thermally activated process) or it corresponds to the electron transition from the deep level to the valence band (not thermally activated transition) (simplified scheme (c)). Same processes can be attributed to the situation on the graph (b) with initial negative space charge. An opposite situation is shown in graph (d) when the positive space charge decreases from the initial positive space charge or in graph (e) when the negative space charge increases from the initial negative space charge. The sheme (f) describes previous situations (d,e) with not thermally activated electron transition from the conduction band to the deep level or with thermally activated electron transition from the valence band to the deep level.

19

1.8 Metal-Semiconductor interface

A metal contact on a semiconductor surface forms a metal-semiconductor interface, which affects the electrical current flowing through the interface. The interface can be produced as an ohmic contact with a linear current-voltage characteristic or as contact with non-linear voltage characteristic called a Schottky contact.

In the first approximation, let us consider the model based on the work function differences in the metal and in the semiconductor without surface states. The semiconductor is described by the work function ϕ_S, and electron affinity χ. The work function ϕ_S is the energy difference from the Fermi level E_F to the vacuum energy E_{vac}. The electron affinity χ is given by the difference between the conduction band edge E_c and the vacuum energy. The ideal metal is characterized by the metal work function ϕ_M.

Let us explain the formation of the metal-semiconductor interface in the case of the n-type semiconductor with work function ϕ_S, which is higher than the work function of metal ϕ_M. This situation is depicted in Figure 1.6.
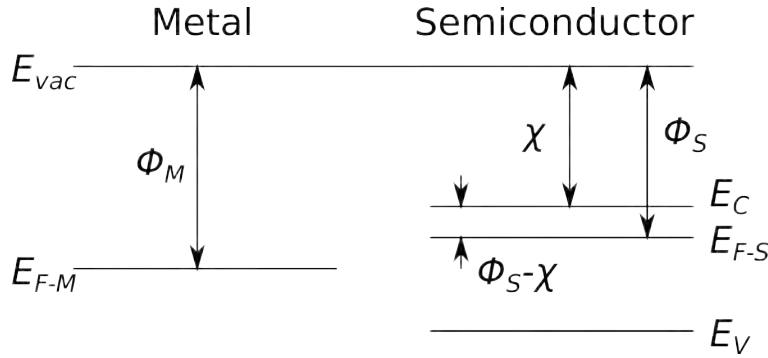
Figure 1.6: The band scheme before deposition of the metal on the semiconductor surface.

After connecting the metal and semiconductor, the electrons flow to the metal from semiconductor in order to establish the equilibrium. The Fermi levels in both materials are pinned relatively to the Fermi level position in the metal, and the positive space charge is formed in the semiconductor nearby the interface. It means that the Fermi level in the semiconductor is shifted down due to the difference between metal and semiconductor work functions

$$V_{bi} = \phi_M - \phi_S. \tag{1.47}$$

Here V_{bi} is the band bending. It corresponds with the bending of the conduction or the valence band in the vicinity of the interface (Figure 1.7).

The electron transition from the metal to the semiconductor is affected by the Schottky barrier height ϕ_{B0}

$$\phi_{B0} = \phi_M - \chi. \tag{1.48}$$
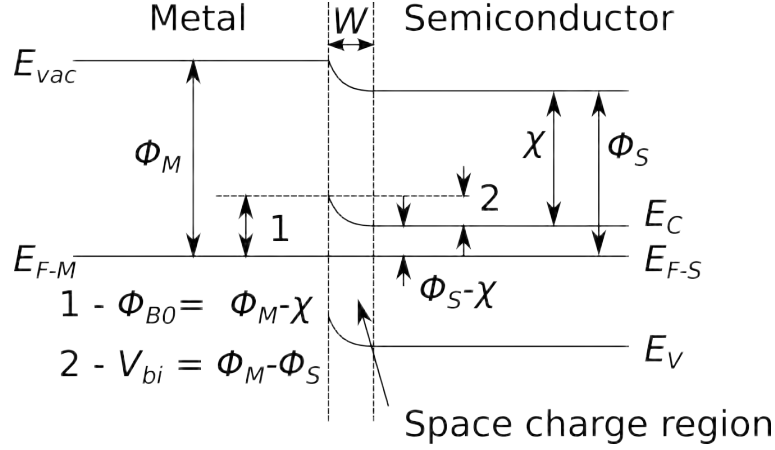
Figure 1.7: The band scheme after deposition of the metal on the semiconductor surface.

The width of the area, where the positive space charge is localized, is called depletion width W [70] and is given by

$$W = \sqrt{\frac{2\varepsilon}{eN_D}\left(V_{bi} - U - \frac{k_BT}{e}\right)},\qquad(1.49)$$

where U is the applied voltage.

When the semiconductor work function is higher than the metal work function, the electrons flow from the metal to the semiconductor, and the Ohmic contact is formed.

In case of the p-type semiconductor, the Schottky barrier height is given by

$$\phi_{B0} = E_G - (\phi_M - \chi).\qquad(1.50)$$

Then, the Ohmic contact is created if the semiconductor work function is lower then the metal work function. Otherwise, the Schottky contact is formed.

The real situation can involve the surface states into the account, which affect the Schottky barrier height [83, 84].

1.9 Schottky barrier lowering

The Schottky barrier lowering $\Delta\phi_B$ is an effect caused by externally applied bias U, which induces the inner electric field $\mathcal{E}$. After the application of the bias on the metal-semiconductor interface, the total potential energy $P(x)$ is given by [70]

$$P(x) = \frac{e^2}{16\pi\varepsilon x} + e\mathcal{E}x,\qquad(1.51)$$

where the first term is the work done by electron transfer to the point x, due to the attraction force (the image force) between electron at distance x from the metal and induced positive charge at $-x$. The second term describes the potential energy due to the applied bias. The situation is shown in Figure 1.8.

The requirement on the equation (1.51)

$$\frac{dP(x)}{dx} = 0\qquad(1.52)$$
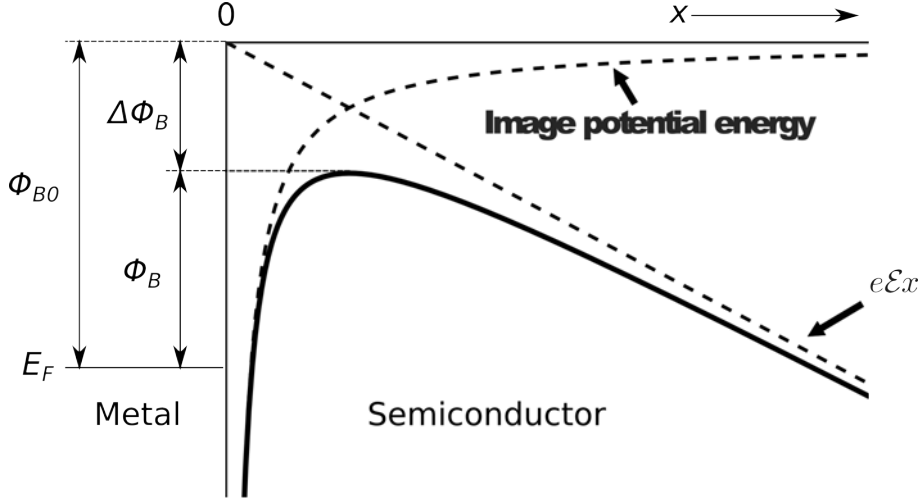
Figure 1.8: Energy diagram between metal and semiconductor [70].

leads to the expression for the Schottky barrier lowering in the form

$$\Delta\phi_B = \sqrt{\frac{e\mathcal{E}}{4\pi\varepsilon}}.$$
(1.53)

Hence, the resulting Schottky barrier is given by

$$\phi_B = \phi_{B0} - \Delta\phi_B.$$
(1.54)

1.10 Current transport in Schottky barrier

The majority carriers are responsible for the current in metal-semiconductor interfaces. There are three main theories describing transport over the barrier. The first theory is thermionic emission theory [85], which is based on three presumptions. The energy value of the Schottky barrier height ϕ_B is higher than the value of the $k_B T$, there are no electron collisions in the depletion region and the Schottky lowering is neglected.

The second theory is the isothermal diffusion theory designed by Schottky in 1938 [86]. This theory has the same assumption for the value of the Schottky barrier height. However, electron collisions are involved in the depletion region, and two more presumptions are included. The first presumption is that the current flow in the depletion region does not affect the carrier concentration. The second presumption is that the concentration of impurities is non-degenerate.

The third theory is more complex because it combines both theories. It is called thermionic emission-diffusion theory [87]. Also, it takes into account the effect of the Schottky barrier lowering.

Based on the third theory, the I-V characteristics of semiconductor with metal contacts are described by the following equation [70]

$$I = AA^* T^2 \exp\left(-\frac{\phi_B}{k_B T}\right) \left[\exp\left(\frac{eV}{k_B T} - 1\right)\right],$$
(1.55)

where A is the area of the contact, A^* is the Richardson constant, and ϕ_B is Schottky barrier height (eq. (1.54)).

At higher voltages, the current is affected by Schottky barrier heights at interfaces which limit the current. In reverse biasing, the equation (1.55) is simplified and it leads to the equation for the I-V characteristic in the following form

$$I_r = AA^*T^2 \exp\left(-\frac{\phi_{B0} - \Delta\phi_B}{k_B T}\right). \tag{1.56}$$

Assuming equation (1.53) and the fact that the electric field nearby the interface can be described by $E = \sqrt{\frac{2eN_t}{\varepsilon}U}$ the equation (1.56) may be rewritten as

$$\ln\left(I_r\right) = \ln\left(AA^*T^2\right) - \frac{\phi_{B0}}{k_B T} - \frac{1}{k_B T}\sqrt{\frac{e}{4\pi\varepsilon}\sqrt{\frac{2eN_t}{\varepsilon}}}U^{1/4}. \tag{1.57}$$

Therefore, this model based on the Schottky barrier lowering is valid if the reverse current dependence of $\ln\left(I_r\right)$ versus $U^{1/4}$ is linear.

1.11 Separation of bulk and surface leakage currents

The total current flowing through the detector is often strongly affected by the surface states between electrodes. These conductive states can be reduced by the surface etching or the surface passivation [88, 89, 90]. However, these processes are not always applicable in our experiments, which demand high optical quality of the surface. Fortunately, there is another method how to separate the current flowing through the material and current flowing over the surface. It is the application of the guard ring electrode. Scheme of this contact is depicted in Figure 1.9 [91, 92] The top contact consists of the central electrode and the guard ring electrode, which surrounds the central electrode. Between the central electrode and the guard ring electrode is a gap that electrically separates both parts from each other. Both parts are at the same potential, so the central electrode collects the current from the bulk, and the guard ring collects the current flowing over the surface.
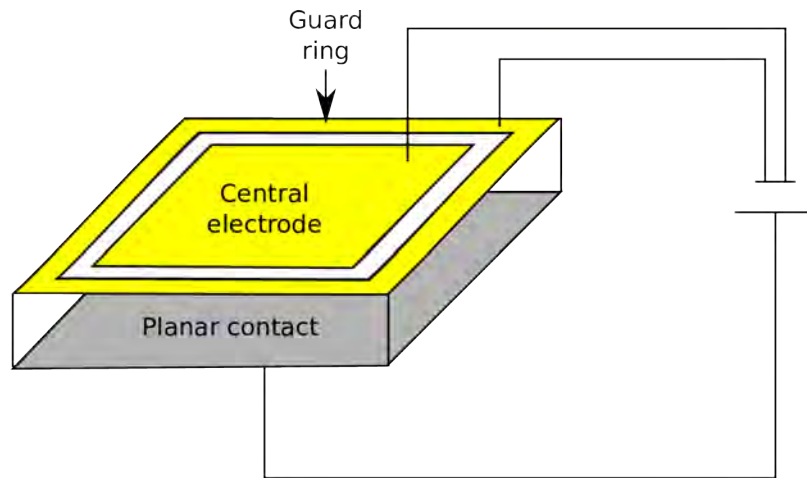
Figure 1.9: Scheme of the guard ring and the central electrode.

1.12 Optics of anisotropic media

One of the main experimental methods used in this thesis is based on the fact that the CdTe material and its compounds exhibit anisotropic properties under the applied bias (the Pockels effect).

In case of an anisotropic medium, the electric displacement $\mathbf{D}$ is dependent on the linear combination of the components of the electric field $\mathbf{E}$ by [93]

$$\mathbf{D} = \boldsymbol{\varepsilon}\mathbf{E}, \tag{1.58}$$

where $\boldsymbol{\varepsilon}$ is the dielectric tensor. This tensor describes dielectric properties of the medium in three arbitrary orthogonal axes.

Alternatively, we can describe the anisotropic medium with tensor of dielectric impermeability $\boldsymbol{\eta}$

$$\varepsilon_0\mathbf{E} = \boldsymbol{\eta}\mathbf{D}. \tag{1.59}$$

Comparison between equation (1.58) and equation (1.59) leads to the relation between tensors

$$\boldsymbol{\eta} = \frac{\varepsilon_0}{\boldsymbol{\varepsilon}}. \tag{1.60}$$

Using the principal coordinate system, the non-diagonal members disappear, and the equation (1.60) can be rewritten

$$\eta_{ii} = \frac{\varepsilon_0}{\varepsilon_{ii}} = \frac{1}{n_i^2}, \tag{1.61}$$

here n_i are the main refractive indices.

The dielectric impermeability tensor is symmetric $\eta_{ij} = \eta_{ji}$, which allows to use the following equation for characterization of anisotropic media

$$\sum_{ij} \eta_{ij} x_i x_j = 1. \tag{1.62}$$

Here x_i and x_j are the axes of the coordinate system formed by principal axes. By substituting the equation (1.61) into the equation (1.62), we get the expression for the index ellipsoid or the indicatrix

$$\frac{x_1^2}{n_1^2} + \frac{x_2^2}{n_2^2} + \frac{x_3^2}{n_3^2} = 1. \tag{1.63}$$

The index ellipsoid (see Figure 1.10) describes the optical properties of the anisotropic medium and allows us to determine the refractive index as a function of the polarization of the plane wave.

1.13 Electro-optic effect

In the case of the applied bias on an electro-optic material, the impermeability tensor $\boldsymbol{\eta}$ is a function of the inner electric field $\mathbf{E}$ which is related to the applied bias. Therefore, the refractive index is also a function of the applied bias. Using a Taylor series around $\mathcal{E} = 0$ the tensor of dielectric impermeability can be written as [94]

$$\eta_{ij}(\mathbf{E}) = \eta_{ij}(0) + \sum_k \mathfrak{r}_{ijk}\mathcal{E}_k + \sum_{kl} \mathfrak{s}_{ijkl}\mathcal{E}_k\mathcal{E}_l \quad ; \quad i,j,k,l = 1,2,3, \tag{1.64}$$
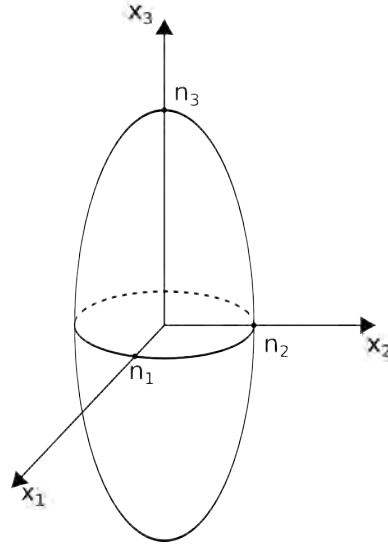
Figure 1.10: The index ellipsoid. The main axes of the coordinate system are (x_1, x_2, x_3) and the main refractive indices of the anisotropic medium are (n_1, n_2, n_3)

where $\mathfrak{r}_{ijk} = \frac{\partial \eta_{ij}}{\partial E_k}$ are Pockels coefficients, and $\mathfrak{s}_{ijkl} = \frac{1}{2}\frac{\partial^2 \eta_{ij}}{\partial E_k \partial E_l}$ are Kerr coefficients. Higher terms of the series are neglected.

The tensor of Pockels coefficient has 18 independent members and tensor $\mathfrak{s}$ has 36 independent elements due to the symmetry of the dielectric impermeability tensor. The CdTe material and its compounds are formed in crystal symmetry of cubic crystal $(\bar{4}3m)$. In this case the Kerr coefficient can be neglected because its elements are much smaller when compared to the elements of the Pockels tensor $\mathfrak{r}$.

The tensor $\mathfrak{r}$ can be reduced into the matrix of 6×3, due to the symmetry of the $\boldsymbol{\eta}$. The reduction of indexes i and j of the Pockels coefficient to one index I is described in the table 1.1.

Table 1.1: Table of $\mathfrak{r}_{i,j}$ reduction into $\mathfrak{r}_I$.

j	i:1	2	3
1	1	6	5
2	6	2	4
3	5	4	3

Due to the crystal symmetry, the matrix of Pockels coefficients for CdTe materials (zinc-blend structure) and its compounds is shown in equation (1.65)

$$\begin{pmatrix} 0 & 0 & 0 \\ 0 & 0 & 0 \\ 0 & 0 & 0 \\ r_{41} & 0 & 0 \\ 0 & r_{41} & 0 \\ 0 & 0 & r_{41} \end{pmatrix}, \tag{1.65}$$

where only the coefficient r_{41} is non-zero[1].

---

[1]Here we use a standard notation r as an element of matrix $\mathfrak{r}$.

Considering of the equation (1.62), the equation (1.64) and the matrix of Pockels coefficient (1.65) leads to

$$\frac{x_1^2 + x_2^2 + x_3^2}{n_0^2} + 2r_{41}(\mathcal{E}_1 x_2 x_3 + \mathcal{E}_2 x_3 x_1 + \mathcal{E}_3 x_1 x_2) = 1, \qquad (1.66)$$

where Kerr effect is neglected.

In this thesis, the applied bias U is in the direction perpendicular to the (111) plane, therefore the electric field is $\mathbf{E} = \frac{\mathcal{E}}{\sqrt{3}}(1,1,1)$. Then the equation (1.66) is equal to

$$\frac{x_1^2 + x_2^2 + x_3^2}{n_0^2} + \frac{2}{\sqrt{3}}r_{41}\mathcal{E}(x_2 x_3 + x_3 x_1 + x_1 x_2) = 1. \qquad (1.67)$$

It leads to the matrix of dielectric impermeability

$$\eta_{ij}(\mathbf{E}) = \begin{pmatrix} \frac{1}{n_0^2} & \frac{r_{41}\mathcal{E}}{\sqrt{3}} & \frac{r_{41}\mathcal{E}}{\sqrt{3}} \\ \frac{r_{41}\mathcal{E}}{\sqrt{3}} & \frac{1}{n_0^2} & \frac{r_{41}\mathcal{E}}{\sqrt{3}} \\ \frac{r_{41}\mathcal{E}}{\sqrt{3}} & \frac{r_{41}\mathcal{E}}{\sqrt{3}} & \frac{1}{n_0^2} \end{pmatrix}. \qquad (1.68)$$

The eigenvalues of this matrix are equivalent to the refractive indices for new coordinate axes (y_1, y_2, y_3) [95].

$$\begin{aligned} \frac{1}{n_{y_1}^2(\mathcal{E})} &= \frac{1}{n_0^2} - \frac{1}{\sqrt{3}}r_{41}\mathcal{E}, \\ \frac{1}{n_{y_2}^2(\mathcal{E})} &= \frac{1}{n_0^2} - \frac{1}{\sqrt{3}}r_{41}\mathcal{E}, \\ \frac{1}{n_{y_3}^2(\mathcal{E})} &= \frac{1}{n_0^2} + \frac{2}{\sqrt{3}}r_{41}\mathcal{E}. \end{aligned} \qquad (1.69)$$

Therefore,

$$\begin{aligned} n_{y_1}(\mathcal{E}) &= \left(1 - \frac{1}{\sqrt{3}}r_{41}n_0^2\mathcal{E}\right)^{-\frac{1}{2}} n_0, \\ n_{y_2}(\mathcal{E}) &= \left(1 - \frac{1}{\sqrt{3}}r_{41}n_0^2\mathcal{E}\right)^{-\frac{1}{2}} n_0, \\ n_{y_3}(\mathcal{E}) &= \left(1 + \frac{2}{\sqrt{3}}r_{41}n_0^2\mathcal{E}\right)^{-\frac{1}{2}} n_0. \end{aligned} \qquad (1.70)$$

Assuming $(1+\Delta)^{-1/2} \approx 1 - \frac{1}{2}\Delta$ due to the value of r_{41}, which is in the magnitude of 10^{-12} m/V for CdTe, the refractive indices are given by

$$\begin{aligned} n_{y_1}(\mathcal{E}) &= n_0 + \frac{1}{2\sqrt{3}}r_{41}n_0^3\mathcal{E}, \quad (a) \\ n_{y_2}(\mathcal{E}) &= n_0 + \frac{1}{2\sqrt{3}}r_{41}n_0^3\mathcal{E}, \quad (b) \\ n_{y_3}(\mathcal{E}) &= n_0 - \frac{1}{\sqrt{3}}r_{41}n_0^3\mathcal{E} \quad (c). \end{aligned} \qquad (1.71)$$

The CdTe crystal shifts from the isotropic into an anisotropic medium after application of the bias. In view of the indicatrix, the CdTe crystal forms a sphere without the electric field. The application of the bias turns the sphere into the ellipsoid of revolution with a rotation axis defined by equation (1.71)(c).

1.14 Electro-optic intensity modulator

Used electro-optic intensity modulator consists of the Pockels cell, which is placed between two crossed linear polarizers (see Figure 1.11). Using the Jones calculus [93], which presume the monochromatic plane wave (testing light), the intensity transmittance $\mathcal{T}$ can be examined as a function of the phase shift Γ between two orthogonal linear polarisation modes of the testing light.
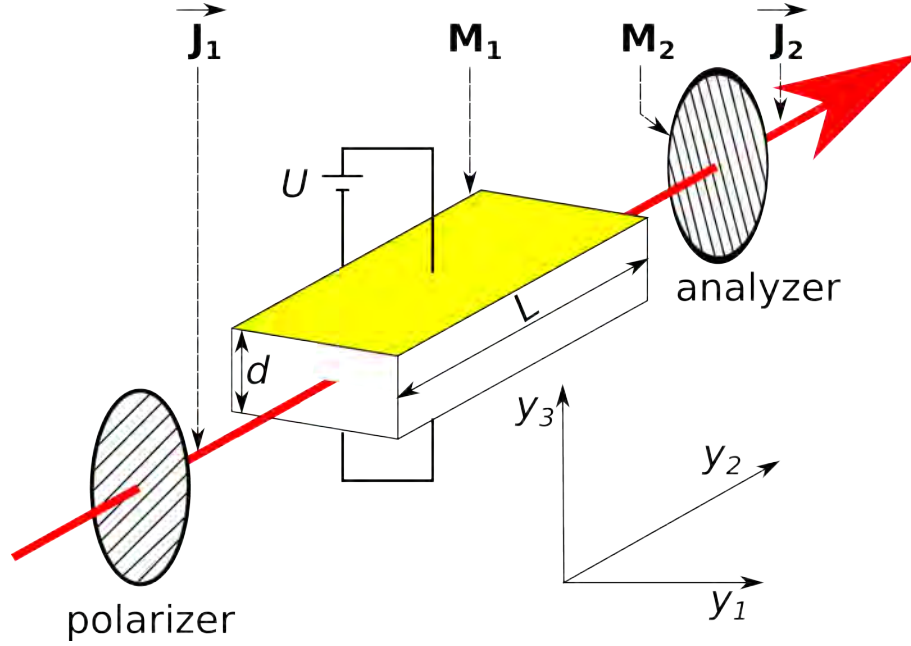
Figure 1.11: Scheme of the electro-optic modulator.

The first linear polarizer is rotated at $45°$ concerning the y_1 axis. The polarisation state of light after passing through this polarizer is described with Jones vector $\mathbf{J_1}$

$$\mathbf{J_1} = \left[\begin{array}{c} \cos 45° \\ \sin 45° \end{array} \right] = \left[\begin{array}{c} \frac{\sqrt{2}}{2} \\ \frac{\sqrt{2}}{2} \end{array} \right]. \tag{1.72}$$

The resulting intensity transmittance is given by

$$\mathcal{T} = J_{2y_1} J_{2y_1}^* + J_{2y_3} J_{2y_3}^*, \tag{1.73}$$

where J_{2y_1} and J_{2y_3} are element of the Jones vector $\mathbf{J_2}$ of the output beam, which is equal to

$$\mathbf{J_2} = \mathbf{M_2}\mathbf{M_1}\mathbf{J_1}. \tag{1.74}$$

Here, $\mathbf{M_1}$ and $\mathbf{M_2}$ are the Jones matrices. The matrix $\mathbf{M_1}$ describes the Pockels cell (matrix of wave retarder), which delays a component of light in the slow axis y_3 by a phase delay Γ, if the fast and slow axis of the Pockels cell equal to the axis y_1 and y_3. The Jones matrix $\mathbf{M_2}$ is connected with the second linear polarizer (analyzer), if the analyzer is placed at $-45°$ with respect to the y_1 axis.

$$\mathbf{M_1} = \left[\begin{array}{cc} 1 & 0 \\ 0 & \exp\left(-i\Gamma\right) \end{array} \right] \quad ; \quad \mathbf{M_2} = \frac{1}{2}\left[\begin{array}{cc} 1 & -1 \\ -1 & 1 \end{array} \right]. \tag{1.75}$$

Combining equation (1.74), equation (1.73) and equation (1.75), the intensity transmittance is given by

$$\mathcal{T} = \sin^2\left(\frac{\Gamma}{2}\right). \tag{1.76}$$

Mutual phase shift Γ is equal to

$$\Gamma = k_0(n_{y_1}(\mathcal{E}) - n_{y_3}(\mathcal{E}))L, \tag{1.77}$$

where L is the optical path length, $k_0 = \frac{2\pi}{\lambda_0}$ is wavenumber and λ_0 is the wavelength of used monochromatic light.

Let us consider that the Pockels cell is the CdTe sample and the electric field is applied in y_3 direction. Then substituting equation (1.71) into equation (1.77) leads to

$$\Gamma = \frac{2\pi}{\lambda_0}\frac{\sqrt{3}}{2}r_{41}n_0^3\mathcal{E}L. \tag{1.78}$$

Using equations (1.76) and (1.78), the electric field distribution can be written as a function of transmittance $T(y_1, y_3)$

$$\mathcal{E}(y_1, y_3) = \frac{\arcsin\sqrt{T(y_1, y_3)}}{\alpha_p} \quad ; \quad \alpha_p = \frac{\sqrt{3}}{2}\frac{\pi r_{41}n_0^3 L}{\lambda_0}. \tag{1.79}$$

The equation (1.79) is valid for the inner electric field $\mathcal{E}$ in a range between 0 and half-wave electric field $\mathcal{E}_{\frac{\pi}{2}}$. This electric field induces the mutual phase shift $\Gamma = \pi$ until which the transmittance T is a monotonic function of $\mathcal{E}$. At higher electric field, this is not true and the equation (1.79) must be adjusted according to the ranging of the electric field with respect to the half-wave electric field.

In this thesis, the measured electric fields were below the half-wave electric field and the equation (1.79) was valid for evaluating of the electric field from transmittance.

2. Experimental methods

2.1 Pockels effect

The basic scheme of the experimental set-up for Pockels effect measurements is shown in Figure 2.1. The set-up consists of a testing light, two polarizers, and an InGaAs camera. The sample is placed between two crossed polarizers and the testing light at a wavelength of $\lambda_0 = 1550$ nm passes through the sample. The transmitted light is collected by an IR InGaAs camera. Then the distribution of the inner electric field $\mathcal{E}(x,z)$[1] is described by the equation (1.79)[2].
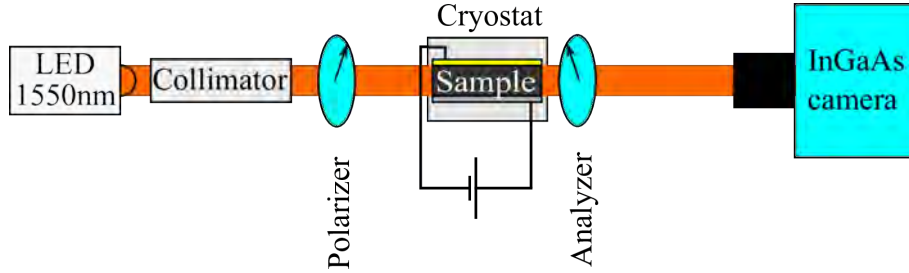
Figure 2.1: Basic experimental set-up for Pockels effect measurements.

The sample is placed in a cryostat, and the temperature is set using a thermo-electric cooler. The thermoelectric cooler is controlled by Eurotherm temperature controller which can set the temperature in the range from 270 K up to 373 K with an error of 0.1 K. The cryostat can be evacuated or filled with ambient air or argon (Ar) atmosphere.

The InGaAs camera (XenICs-Xeva) camera has a resolution of 320×256 pixels, and it is equipped with thermoelectric cooler able to set a temperature to 240 K. The camera communicates with the PC via the supplied software *X-control*.

This set-up allows to measure the electric field distribution after application of bias as well as its temperature evolution with time resolution of 10 *ms*.

2.1.1 Modified set-ups

The basic set-up for Pockels effect measurement was modified by adding the additional light which illuminates the top contact of the sample. The additional light was Light-Emitting Diode (LED) at a wavelength of 940 nm or a tunable light from monochromator in the range of $900 - 1800$ nm (see Figure 2.2(a)). The set-up with LED was used to measure temporal and temperature dependence of the inner electric field on illumination.

The set-up with monochromator is used to scan the spectral dependence of the inner electric field in the sample with a step of 25 nm. The monochromatic incident light has a constant photon flux about 1.0×10^{15} photons cm^{-2}s^{-1}. This technique allows us to determine the deep levels in the sample due to the measurement of the change of the inner electric field.

---

[1] y_1, y_2, y_3 were renamed to x, y, z for an easier notation.
[2] More information in the sections 1.13 and 1.14 where the theory of Pockels effect and electro-optic modulator are described.
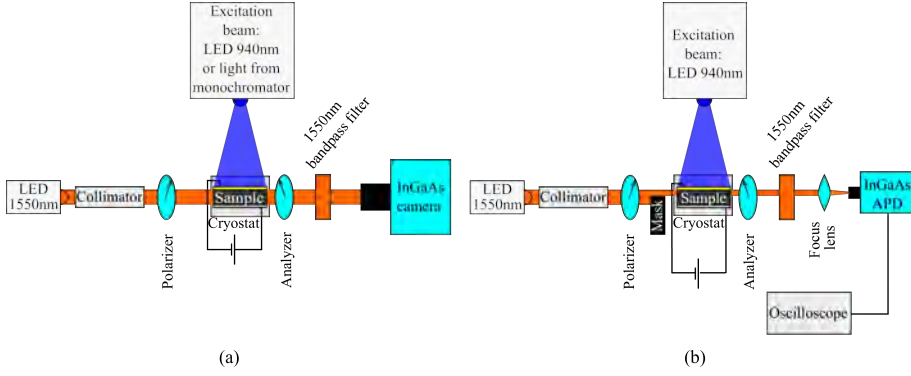
Figure 2.2: Modified experimental set-ups for Pockels effect measurements. The scheme (a) shows the set-up for steady state measurement of the electric field and its time evolution with resolution of 10 ms. The set-up for time evolution of the electric field measurements with time resolution of 5 μs is shown in scheme (b).

Let us describe the analysis of this measurement technique on the simplified diagrams (Figure 2.3). We use a band structure model with two deep levels in the band-gap. The bias is applied and the sample is in steady-state. Let us suppose that the electric field profile increases from the anode to the cathode. It means that a positive space charge is localized in the sample according to the Gauss law (Figure 2.3(a)).

The Figure 2.3(b) shows the situation when the sample is illuminated by the light with energy $h\nu$ from the monochromator. The energy $h\nu$ is below the energy band-gap E_G. It means that the illumination goes through the sample volume (see section about Optical absorption 1.5). If the photon energy matches the energy distance of the deep level E_{t1} from the maximum of the valence band E_v, it causes optically induced electron transitions from the valence band to the deep level which results in an increase of the negative space charge in the sample (trapping and de-trapping processes are in balance). This is manifested by a profile of electric field which decreases from the anode to the cathode. We assume here that the photon energy is lower than the energy distance between the conduction band E_c and the deep level E_{t2}.

The photon energy of illumination shown in the situation in Figure 2.3(c) is higher than energy distance of E_{t1} from the valence band. It means that the electron transitions from E_v to E_{t1} are still active and the trapping and de-trapping is in balance. Also, the photon energy matches the energy distance from E_{t2} to E_c which causes optically induced electron transitions from the deep level E_{t2} to the conduction band. It results into a decrease of negative space charge which causes that the electric field under the cathode grows.

The presented scheme can be used to evaluate energies in the energy band-gap and types of traps by illumination of the sample (Pockels cell) with light from monochromator by measuring the change of electric field profile in dependence of wavelength of the light. If the negative space charge increases upon illumination (positive space charge decreases) the electron transitions are optically induced from the valence band to the deep level and the electric field under the cathode decreases. On the other hand, if the electric field under the cathode increases the negative space charge decreases (positive space charge increases) and the electron transitions from deep level to the conduction band take place.
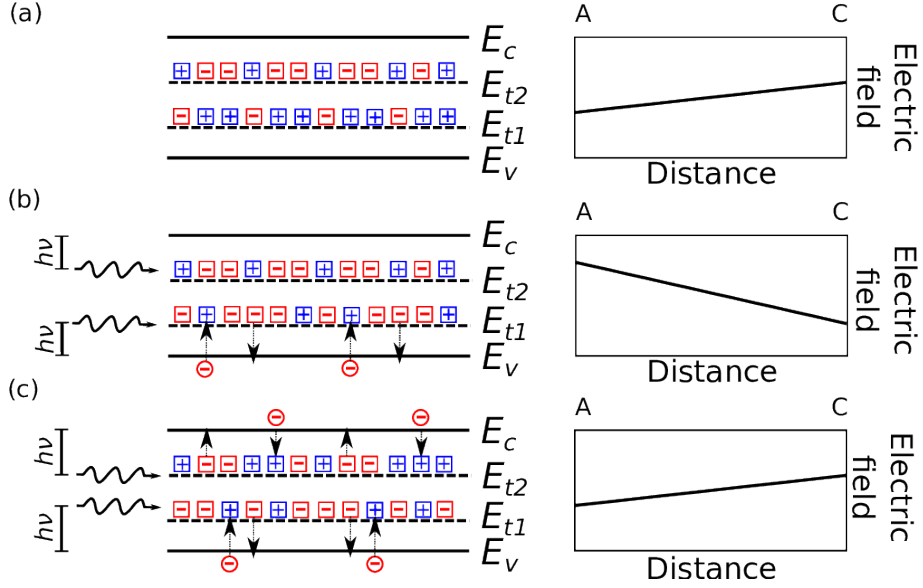
Figure 2.3: Simplified diagrams of band structure with two deep levels and corresponding electric field. Scheme (a) shows situation without illumination. The positive space charge is localized in the sample. Then the electric field increases from the anode to the cathode. Scheme (b): the illumination activates the electron transitions from the valence band to the deep level E_{t1}. Then the negative space charge is accumulated in the sample and the electric field decreases from the anode to the cathode. Scheme (c) depicts situation when illumination induces electron transition from E_v to E_{t1} and also from E_{t2} to E_c. The electric field declines from the anode to the cathode due to the negative space charge presence in the sample.

The set-up with LED at 940 nm is used to measure the temporal and temperature evolution of the inner electric field after switching on/off the addition light.

The second modified set-up is shown in Figure 2.2(b) was used to measure the time and temperature evolution of the electric field under the electrode with higher time resolution up to 5 μs. The metal mask was placed in front of the sample, so the testing light passed through only a small area of the sample below the cathode. The transmitted light was focused on a chip of InGaAs avalanche photodiode (APD) which was connected to an oscilloscope where the output voltage signal was scanned. The APD records an average electric field from the area under the cathode which is defined by a metal mask. The time resolution of the APD was 5 μs.

In both set-ups, the sample was mounted in a cryostat, and the temperature range between $270 - 373$ K was controlled using a thermoelectric cooler with error of 0.1 K.

2.1.2 Electric field evaluation

The InGaAs camera acquires the images of the transmitted light through the sample. Examples of the images are depicted in Figure 2.4. The intensity of the captured signal depends on the integration time, which is set with the software controlling the camera. It is important to set the integration time, avoiding overexcitation at each pixel of the image. In Figure 2.4, the image (a) is the

transmitted light intensity distribution $I_0(x, y)$ through the sample when the polarizers are parallel, and the bias is not applied. The image (b) represents the thermal noise of the camera $I_0^{bcg}(x, z)$, which is taken when the testing light is switched off. The images (c) and (d) are captured with crossed polarizers with applied bias $I(x, z)$ and without bias $I^{bcg}(x, z)$, respectively.

For the reconstruction of the inner electric field, the equation (1.79) must be rewritten with respect to the integration time of the camera and to the thermal noise, which randomly initiates a signal. Assuming these facts the equation for evaluation of the electric field distribution $\mathcal{E}(x, z)$ is given by

$$\mathcal{E}(x, z) = \frac{\sqrt{T(x, z)}}{\alpha_p} \quad ; \quad T(x, z) = \frac{[I(x, z) - I^{bcg}(x, z)]t^{para}}{[I_0(x, z) - I_0^{bcg}(x, z)]t^{cross}}. \qquad (2.1)$$

Here t^{para} and t^{cross} is integration time during measurement with parallel polarizers and crossed polarizers, respectively.
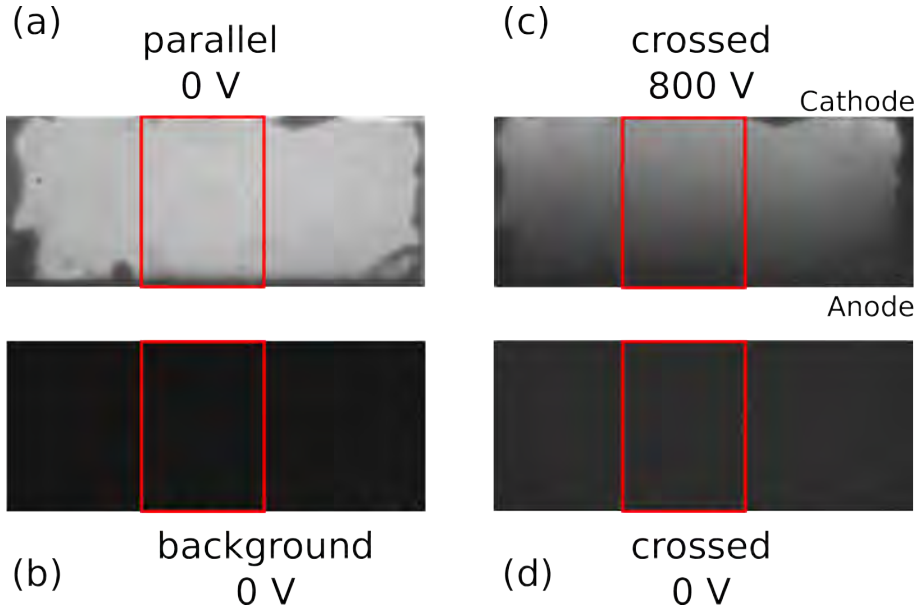
Figure 2.4: The captured images of the transmitted light through the sample by the camera. The images (a) and (b) are acquired with the parallel polarizers with the testing light on for (a) and off for (b), respectively. The images with crossed polarizers are shown in (c) and (d). The image (c) is captured, when the bias is applied on the sample. The image (d) is captured without bias. The red square describes the selected area for the determination of the electric field. The selected area is without significant surface and bulk defects, which affect the transmitted light.

The measurement is affected by the surface and bulk defects in the sample. These defects negatively change the acquired image. For the measurement and analysis of the electric field profile the area with a minimum amount of defects is chosen (the red square in Figure 2.4).

The profiles of the averaged counts through the direction parallel with the electrodes from the selected area in Figure 2.4 are shown in Figure 2.5. The resulting electric field is calculated using equation (2.1) and it is depicted in the same Figure 2.5.
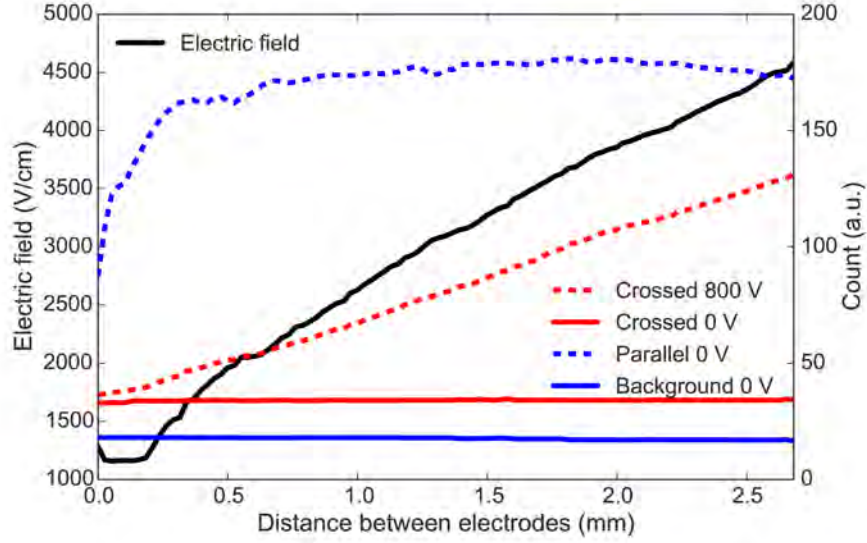
Figure 2.5: Distribution of the average counts in the red area from the images in the Figure. 2.4 between electrodes. The resulting electric field is plotted as a black solid line.

2.2 I-V characteristic

The measurement of I-V characteristic is a technique that allows to determine the sample resistivity from its course close to 0 V as well as to evaluate energy barriers at the metal/semiconductor interfaces. The resistivity is evaluated from Ohm's law because, in this regime, the current is not affected by the semiconductor-metal interface.

The standard I-V characteristic is described by equation (1.55). At higher voltages, the current is affected by Schottky barrier heights lowering, and the I-V characteristic can be described by equation (1.56). Assuming the Schottky barrier lowering (equation (1.53)), and the electric field in the vicinity of the interface in a term $E = \sqrt{\frac{2eN_t}{\varepsilon}U}$, the Schottky barrier height Φ_{B0} can be determined from the following equation

$$\ln\left(I_r\right) = B - DU^{1/4}, \tag{2.2}$$

where

$$B = \ln\left(AA^*T^2\right) - \frac{\phi_{B0}}{k_BT} \quad ; \quad D = \frac{1}{k_BT}\sqrt{\frac{e}{4\pi\varepsilon}\sqrt{\frac{2eN_t}{\varepsilon}}}. \tag{2.3}$$

The theory of Schottky barrier height and Schottky barrier lowering is described in sections 1.8, 1.9 and 1.10, respectively.

The used set-up for measuring the I-V characteristics is depicted in Figure 2.6. It is designed to measure a sample with both planar contacts or a sample with a central electrode and a guard ring. The bottom planar contact is connected to the high voltage (HV). The sample is biased by sourcemeter Keithley 2410 or sourcemeter ISEG SHQ 122M. The currents flowing through the sample bulk, or sample surface are evaluated from measured voltages on two serial resistors with the resistance $R = 1$ MΩ by using Keithley 6514 or Keithley 2000 electrometers

as

$$I_B = \frac{V_B}{R}; \quad I_L = \frac{V_L}{R}. \tag{2.4}$$

Here I_B is the bulk current, V_B is the measured voltage at the resistor connected to a central electrode, R is the resistance of the resistor, I_L is the leakage current flowing through the guard ring and V_L is the measured voltage at the resistor attached to a guard ring.
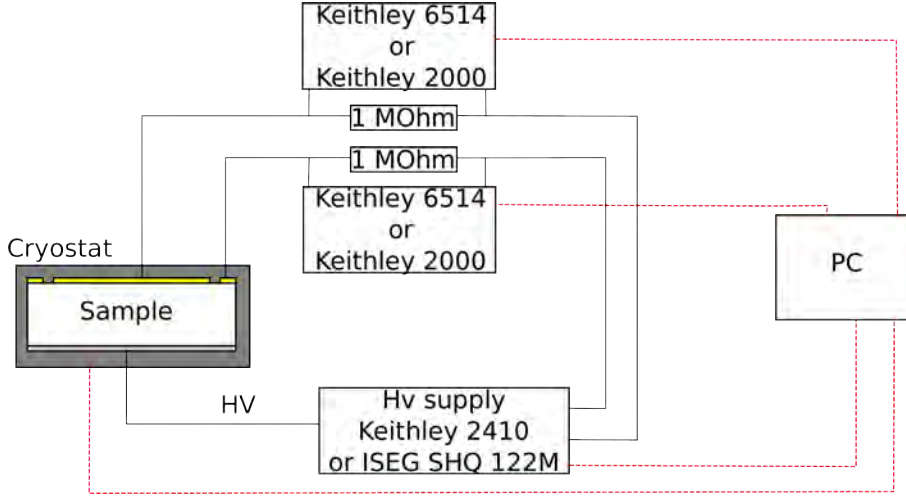
Figure 2.6: The diagram of the set-up used for measuring the I-V characteristics. The black solid lines describe the electrical circuit. The red dashed lines show the connection between PC and devices.

The sample is placed in the cryostat, which can be filled with ambient air or Ar atmosphere. The temperature is set in the range of $270 - 373$ K using the thermoelectric cooler.

The measurement is controlled via a script in Labview software.

2.3   Ellipsometry

Ellipsometry is a non-destructive method based on measuring changes in light polarisation upon reflection on the material structure. The ellipsometric angles Ψ and Δ represent the polarisation changes in reflected light. These angles are connected with Fresnel reflection coefficients for s- and p- polarized light by

$$\delta = \frac{r_s}{r_p} = \tan(\Psi)\exp(i\Delta). \tag{2.5}$$

The parameters describing the examined materials (thickness, optical constants, etc.) are characterized by the measured spectral dependence of ellipsometric angles Ψ and Δ. The experimental data are fitted by the proper theoretical model to obtain parameters describing materials.

A commercial Mueller matrix ellipsometer J.A.Woollam RC2 was used to measure ellipsometry experimental data. The ellipsometry data were obtained for the photon energy ranging from 1.24 to 6.5 eV.

2.4 Samples

Seven samples were prepared for investigations by electrical and optical methods. Two of them were cut from detector-grade ingots Cadmium Telluride (CdTe) doped with Chlorine (Cl) and Indium labelled as sample #1 and sample #2, respectively. The samples exhibited n-type conductivity from thermoelectric power measurement [96]. The measurement of the sample #2 (CdTe:In) gave a clear signal which referred to an n-type conductivity. The sample #1 (CdTe:Cl) conductivity measurement had a weak n-type signal, which corresponds to a position of the Fermi level close to the mid-gap.

Other three samples #3 − #5 were prepared from n-type Cadmium Zinc Telluride (CdZnTe) with 10% of Zn. The samples were doped with In.

One sample was made from Cadmium Telluride Selenide (CdTeSe) with a content of Se 5%. The sample was marked as #6.

The last sample #7 was cut from Cadmium Zinc Telluride Selenide (CdZnTeSe) ingot containing 10% of Zn in the Cd sublattice and 4% of Se in the Te sublattice. The sample conductivity was n-type.

The CdTe crystals were grown by Vertical Gradient freeze method in the Institute of Physics, Charles University. The CdZnTe samples were prepared from commercial material prepared by travelling heater method (THM). The CdZnTeSe crystal was grown at Brookhaven National Laboratory also by THM method. The surfaces were mechanically polished with Aluminum Oxide (Al_2O_3) abrasive up to optical quality (surface RMS 2 nm), without any further chemical treatment.

Samples were equipped with contacts on large opposite sides by evaporation. The indium (In) formed the bottom planar contact, and the opposite contact structure consisting of central electrode and guard ring was from Au. The guard ring allows to separate bulk and surface leakage currents during electrical measurements. The distance between the guard ring and the central electrode was ≈ 0.4 mm. The scheme of the sample with and without a guard ring is shown in Figure 2.7.
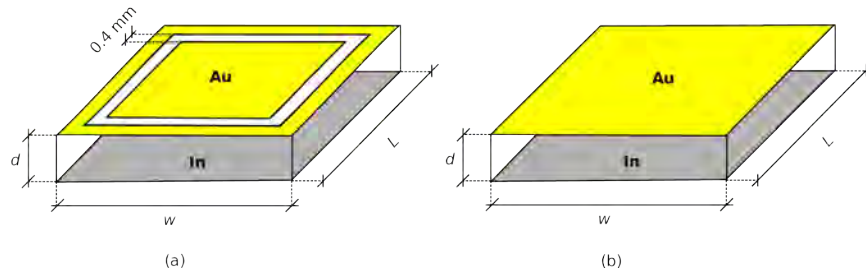
Figure 2.7: The scheme (a) shows the configuration with guard ring and central electrode. The basic configuration with planar contacts is depicted on scheme (b). Three values describe the sample dimensions: d is the thickness, L is the optical length/depth, and w is its width.

The fundamental properties of samples and performed experimental methods are listed in the table 2.1.

Table 2.1: List of measured samples and their properties. Experimental methods: E...Ellipsometry, I-V...I-V characteristic (Resistivity, Schottky barrier heigh), PE...Pockels effect

Sample #	Material	Dimension (mm^3)	Guard ring	Methods
1	CdTe:Cl	$5.0 \times 3.5 \times 1.5$	$\checkmark$	E,I-V
2	CdTe:In	$4.3 \times 4.6 \times 1.6$	$\checkmark$	E,I-V
3	CdZnTe	$5.4 \times 5.4 \times 2.0$	$\checkmark$	E,I-V,PE
4	CdZnTe	$5.0 \times 4.3 \times 1.5$		E,I-V,PE
5	CdZnTe	$5.4 \times 5.4 \times 2.0$		PE
6	CdTeSe	$5.0 \times 3.5 \times 2.0$	$\checkmark$	E,I-V
7	CdZnTeSe	$6.5 \times 5.3 \times 2.7$	$\checkmark$	E,I-V,PE

3. Results

3.1 Ellipsometry measurements and I-V measurements

The ellipsometry measurements and I-V measurements were performed at all the samples except the sample #5-CdZnTe. The oxide surface layer growth after low-temperature annealing in ambient air was analyzed by using ellipsometry measurement and I-V measurements (see subsection 3.2.1).

The ellipsometry data were evaluated by a theoretical model published in the ref. [97]. The complex theoretical model consists of the models for CdTe, TeO_2, and Tellurium predefined in the Woollam database. This database contains predefined models for common materials, including CdTe and CdTe oxide, The CdTe/CdTeSe/CdZnTe/CdZnTeSe material was parameterized by Lorentz oscillators, and the CdTe oxide was parameterized with the Cauchy equation. The used model is described by effective medium approximation (EMA) and the surface roughness layer. The EMA layer substitutes a non-uniform surface layer with material peaks and trenches with an average value, because the oxide layer grows on a rough non-uniform bulk surface [98, 99].

The I-V characteristics were measured using the set-up shown in Figure 2.6.

Some of the presented results in this section about ellipsometry measurements and I-V characteristics were published in refs. [100, 101, 102].

3.1.1 Energy band-gap measurements

The ellipsometry was measured in reflection mode with three incident angles 55°, 60° and 65°, respectively. The range of spectral photon energies was between 0.80 and 6.42 eV. Acquisition time was 120 seconds. The incident light beam diameter was adjusted by an iris aperture to approximately 1.5 mm.

The measured ellipsometry spectra are depicted in Figure 3.1 for all studied samples. Each graph is supplied with the fit (red curves), which allows determining the optical energy band-gap from the first oscillator describing the optical transition between the valence and conduction bands. The evaluated optical parameters refractive index n and extinction coefficient κ in the energy range between 1 eV and 2 eV are shown in Figure 3.2.

The determined energy band-gaps are summarized in the Table 3.1. The values are in a good agreement with the graph in Figure 2, which describes the change of energy band-gap in dependence of the composition of the material. The error of the measurement was estimated to 0.02 eV.

Table 3.1: Determined energy band-gap from ellipsometry measurements.

Sample	#1 CT:Cl	#2 CT:In	#3 CZT	#4 CZT	#6 CTS	#7 CZTS
E_G (eV)	1.50	1.49	1.59	1.56	1.48	1.52
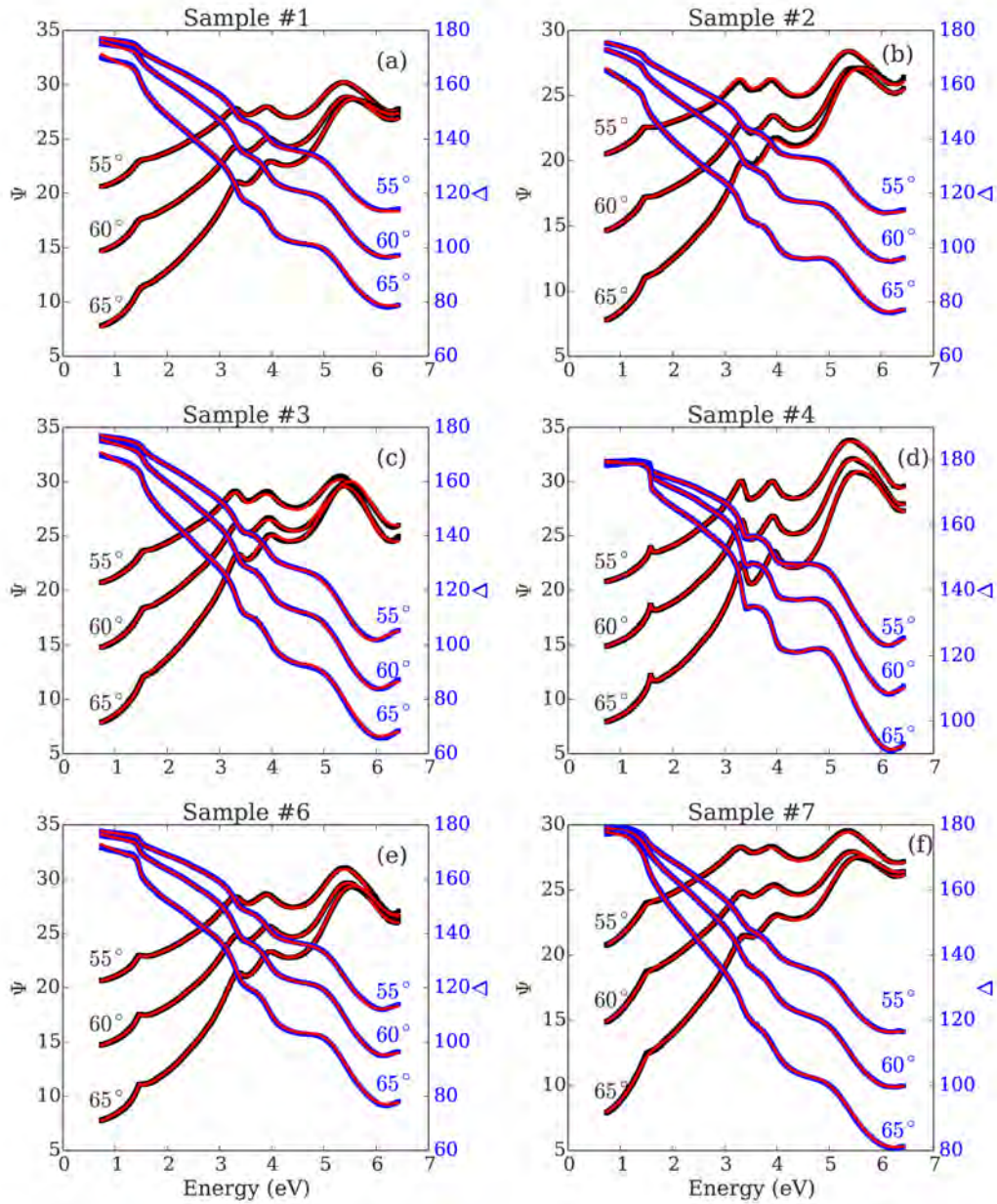
Figure 3.1: The graph (a) shows the ellipsometric parameters Ψ and Δ of the sample CdTe:Cl as a function of the energy. The ellipsometric spectra for CdTe:In, CdZnTe, CdZnTe, CdTeSe and CdZnTeSe are shown in graph (b), (c), (d), (e) and (f), respectively.
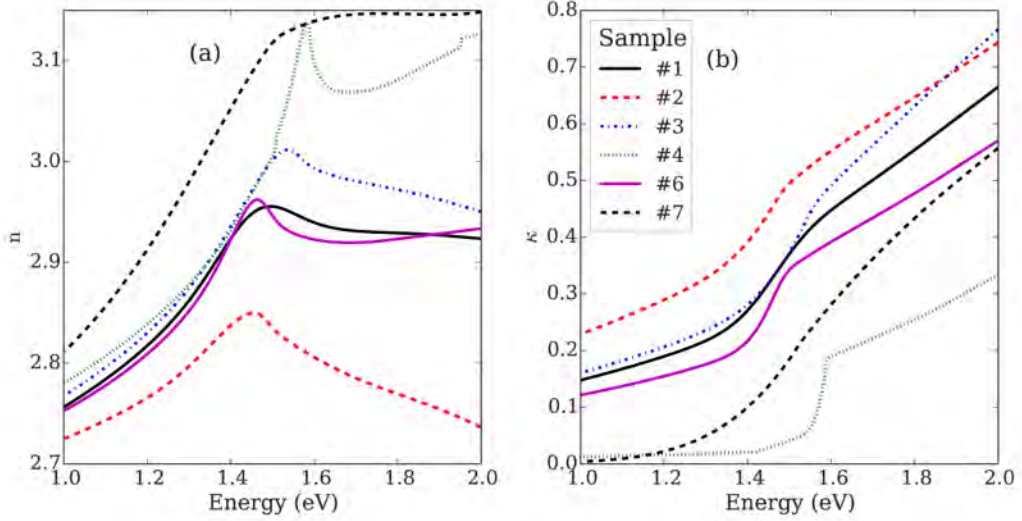
Figure 3.2: The energy dependence of the refractive index n (a) and extinction coefficient κ (b).

3.1.2 Determination of the resistivity and Schottky barrier height based on the I-V measurements

The I-V measurements were performed on the samples $\#1 - \#4$ and $\#6 - \#7$ to determine sample resistivity and to get information about the influence of the metal-semiconductor interfaces on the electric current.

Samples $\#1$-CdTe and $\#2$-CdTe

The I-V characteristics between -1 and 1 V of samples $\#1$ and $\#2$ are shown in Figure 3.3. The experimental data (black squares) are fitted by a linear function (red lines), which describes the Ohm's law. It allows to obtain the value of a sample's resistivity. The samples $\#1$ and $\#2$ resistivities are $\varrho = 2.05 \times 10^9$ Ωcm and $\varrho = 2.49 \times 10^8$ Ωcm, respectively.

The Fermi level E_F is connected to resistivity by the equation:

$$\varrho = \frac{1}{\left[\mu_e N_c \exp\left(\frac{E_F}{k_B T}\right) + \mu_h N_v \exp\left(\frac{(-E_F - E_G)}{k_B T}\right) \right]}. \tag{3.1}$$

The energy band-gap is $E_G = 1.50$ eV for CdTe material (see section 3.1.1). The general carrier mobilities for electrons $\mu_e \approx 1100$ cm^{2}V^{-1}s^{-1} and $\mu_h \approx 80$ cm^{2}V^{-1}s^{-1} for holes were used [103, 104]. The samples exhibit a slight n-type conductivity (thermoelectric measurement). For that reason, we assume that the evaluated Fermi energy value represents the energy distance from the conduction band. The CdTe:Cl Fermi level is at $E_F = E_c - 0.68$ eV and the Fermi level is at $E_F = E_c - 0.63$ eV for CdTe:In. The positions of Fermi level demonstrate that the sample $\#2$-CdTe:In is a stronger n-type than CdTe:Cl.

The I-V characteristics measured on the sample $\#1$ CdTe:Cl in the voltage range from -200 V to $+200$ V and the sample $\#2$ CdTe:In from -600 V to $+600$ V at 300 K are presented in Figure 3.4(a) (We show only the bulk current I_B).

39
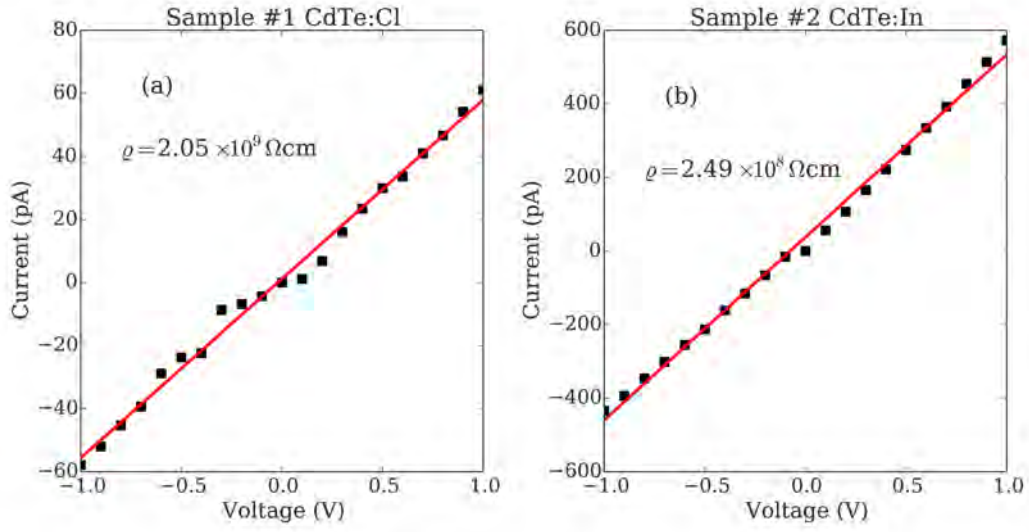
Figure 3.3: The I-V characteristics of samples #1-CT:Cl and #2-CT:In in the voltage range of −1 and 1 V. The experimental data are plotted as black squares and the red line describes the Ohm's law.
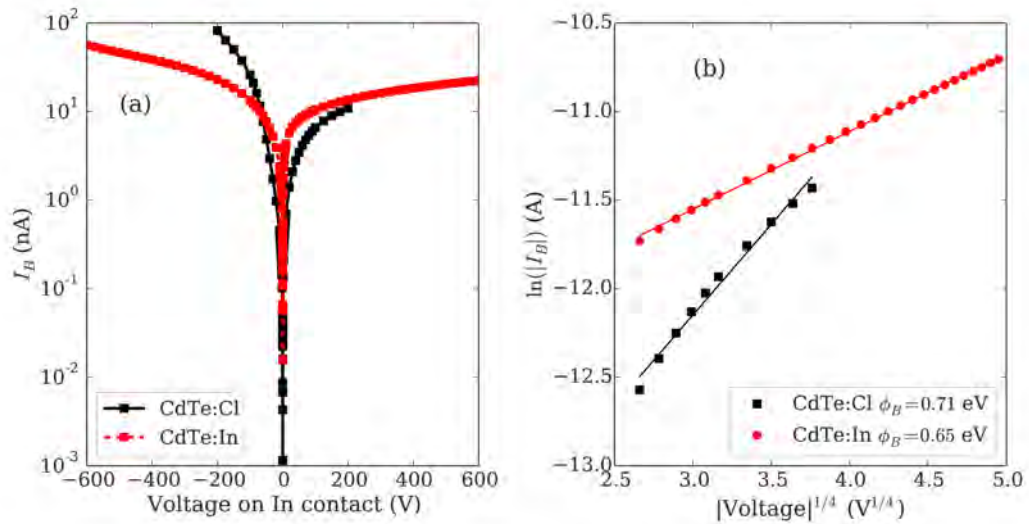
Figure 3.4: The I-V characteristics in the voltage range of −200 and 200 V for the sample #1-CdTe:Cl and −600 V and 600 V for the sample #2-CdTe:In are shown in graph (a). The graph (b) shows the natural logarithm of the absolute value of reverse current versus voltage$^{1/4}$. The determined Schottky barrier heights are 0.71 eV and 0.65 eV for CdTe:Cl and CdTe:In, respectively.
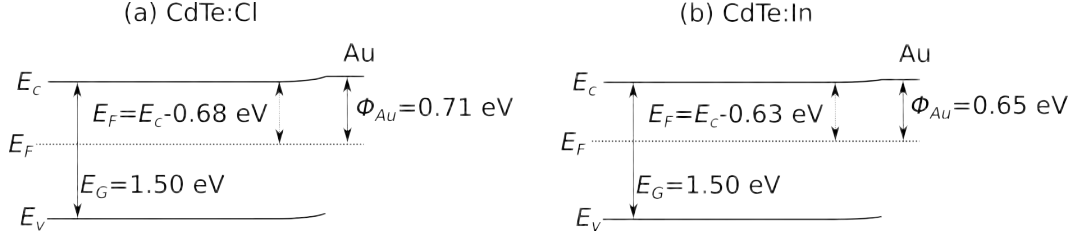
Figure 3.5: Energy diagram (a) of CdTe:Cl/Au structure and CdTe:In/Au (diagram (b)) without applied voltage.

The corresponding profiles of $\ln(I)$ vs $U^{1/4}$ for voltages in the range of $50 - 200$ V for the CdTe:Cl sample and for CdTe:In sample in the range of $50 - 600$ V are presented in Figure 3.4(b). The determined Schottky barrier heights limiting the current flow are 0.71 eV and 0.65 eV for CdTe:Cl and CdTe:In, respectively. Based on the n-type character of conductivity in both samples, we assume that the evaluated Schottky barriers are on the Au/CdTe interfaces. The Fermi levels and Schottky barriers indicate the band bending around 30 meV upwards, which corresponds to a nearly Ohmic contact.

We plotted the assumed energy diagrams of samples #1-CdTe:Cl and #2-CdTe:In in Figure 3.5.

Sample #3-CdZnTe

The I-V characteristic of the sample #4-CZT at $T = 300$ K in the range from -700 V to 700 V is depicted in Figure 3.6(a) (Bulk current is only shown). The determined sample resistivity is $\varrho = 1.00 \times 10^9$ Ωcm and calculated the Fermi level according to the equation (3.1) is $E_F = E_c - 0.67$ eV.
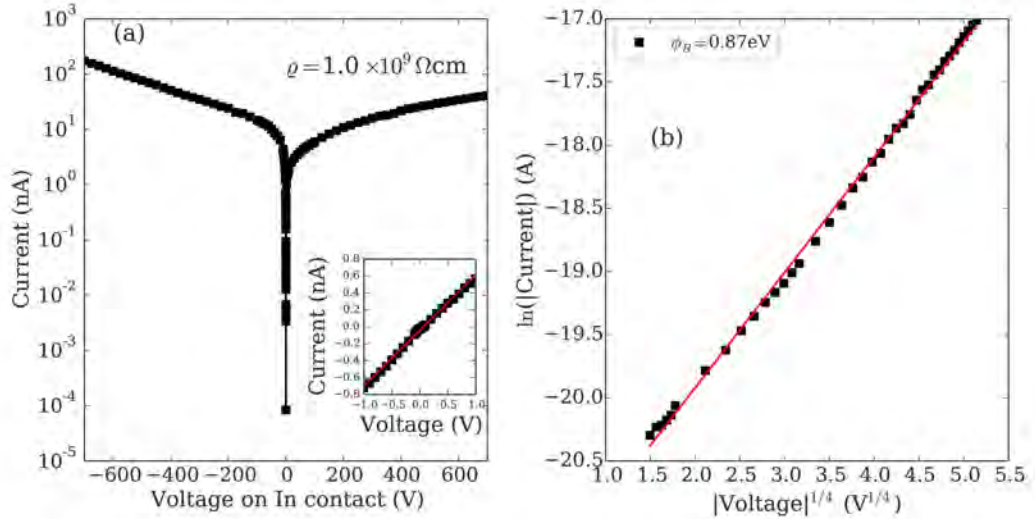
Figure 3.6: The I-V characteristics of sample #3-CZT at $T = 300$ K (graph (a)). The insert graph shows the I-V curve around 0 V. The plot of natural logarithm of the absolute value of reverse current versus voltage$^{1/4}$ is depicted in the graph (b).

The dependence between $\ln(I)$ and $U^{1/4}$ (Figure 3.6(b)) demonstrates the Schottky barrier lowering due to the linear relation. The evaluated Schottky

barrier height is $\phi_{B0} = 0.87$, which we attributed to the Au/CZT interface.

Let us discuss the obtained experimental data based on a simple model of work function difference. The work function of Au $\phi_{Au} \sim 5.3$ eV is close to the work function of semi-insulating CZT (~ 5 eV = sum of electron affinity 4.3 eV and ~ 0.67 eV energy difference between the bottom of the conduction band and the Fermi energy). Therefore, a relatively small band bending upwards can be formed at the interface. This band bending results in blocking of electrons in the reverse direction of the I-V characteristic (Figure 3.6(a)). Figure 3.7 shows the anticipated energy diagram at the Au/CZT interface.

An analogous scheme is also plotted for the In contact (work function $\phi_{In} = 4.1$ eV), where the band bends downwards $4.1 - (4.3 + 0.67) = -0.87$ eV might be reached forming degenerate electron gas at the interface. It should lead to the Schottky barrier height of 1.79 eV. In reality, based on the observations in our recent study [105] we do not suppose that such a strong band bending occurs at In/CZT interface in our samples. Also, as it is often mentioned in the literature (e.g., [83]), the band bending may be significantly reduced due to the surface states.
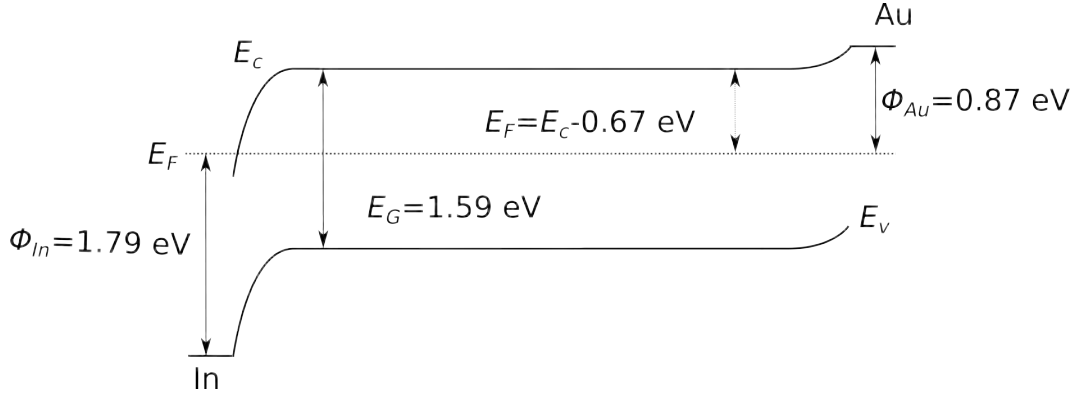
Figure 3.7: Energy diagram of In/CZT/Au structure without applied voltage for the sample #3. Idealized model of work function difference.

The determined Schottky barrier height could theoretically be either at the Au/CZT or In/CZT interfaces because both the Au and In contacts are in the reverse mode. However, the found value is very close to the expected one at the Au/CZT interface assuming near midgap position of the Fermi energy (Figure 3.7).

Sample #4-CdZnTe

The temperature dependence of the I-V characteristic of sample #4-CZT in the range from -400 V to 500 V is shown in Figure 3.8(a). The I-V curves were measured at four different temperatures of 280 K, 300 K, 320 K and 340 K. The inserted graph shows the experimental data around 0 Volt with a linear fit (red line) at 300 K. The determined resistivity is $\varrho = 6.30 \times 10^9$ Ωcm. The Fermi level E_F is connected to resistivity by the equation (3.1). The band-gap energy is $E_G = 1.56$ eV and the sample has slight n-type conductivity from the thermoelectric power measurements. Therefore, we assume that the calculated Fermi level is related to the conduction band minimum at $E_F = E_c - 0.71$ eV.

The I-V characteristic at a higher voltage in reverse polarity (In-Anode; Au-Cathode) is affected by the Schottky barrier lowering (section 1.10). This model is supported by the linear relation between $\ln(I)$ versus $U^{1/4}$ (Figure 3.8(b)). The Schottky barrier height was evaluated around $\phi_{B0} = 0.91$ eV.
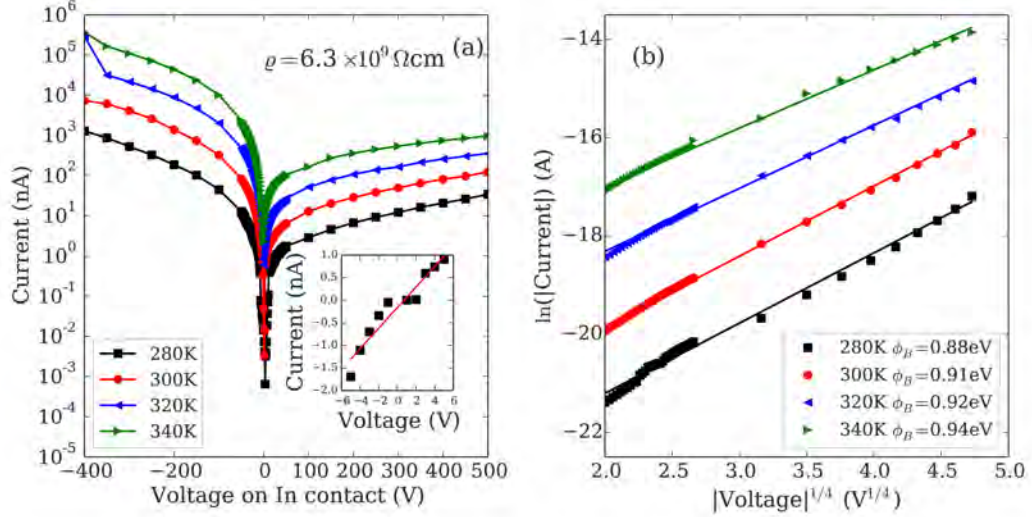
Figure 3.8: The I-V characteristics of sample #4-CZT at different temperatures (graph (a)). The insert graph shows the I-V curve around 0 V. The plot of natural logarithm of the absolute value of reverse current versus voltage$^{1/4}$ is depicted in the graph (b).

The same considerations as for the sample $\#3 - CZT$, lead to the attribution of determined Schottky barrier height to the Au/CZT interface (Figure 3.9(a)). Furthermore, holes are firmly blocked at the In/CZT interface according to the discussed model of work function difference. They have to overcome the barrier of approx. 1.6 eV. Even if the barrier was smaller due to the presence of surface dipoles, the sample is n-type, and the transport of electrons prevails the transport of holes (Figure 3.9(b)). This assumption is supported by the fact, that the current flowing in the reverse direction is electronic, that was confirmed by Hall effect [106] and thermoelectric effect measurements.

Sample #6-CdTeSe

The sample #6 I-V characteristic at 300 K is depicted in Figure 3.10(a). The sample resistivity $\varrho = 5.59 \times 10^6$ Ωcm was determined by the fitting from the current-voltage dependence at low voltages.

The log-log dependence of current versus voltage (Figure 3.10(b)) shows that the current still keeps the Ohm's law due to the slope around 1. It means that the current is not affected by the Schottky barrier. It can be caused by the low resistivity ($\varrho = 5.59 \times 10^6$ Ωcm), which points to a large concentration of charge carriers in the sample and then the effect of the Schottky barrier is negligible. Other possibility is that the Schottky barrier heights are not formed at interfaces, but the metal-semiconductor interfaces create an Ohmic contact.

The Fermi level position $E_F = E_c - 0.53$ eV was calculated using equation 3.1 and taking in account that the sample is n-type.
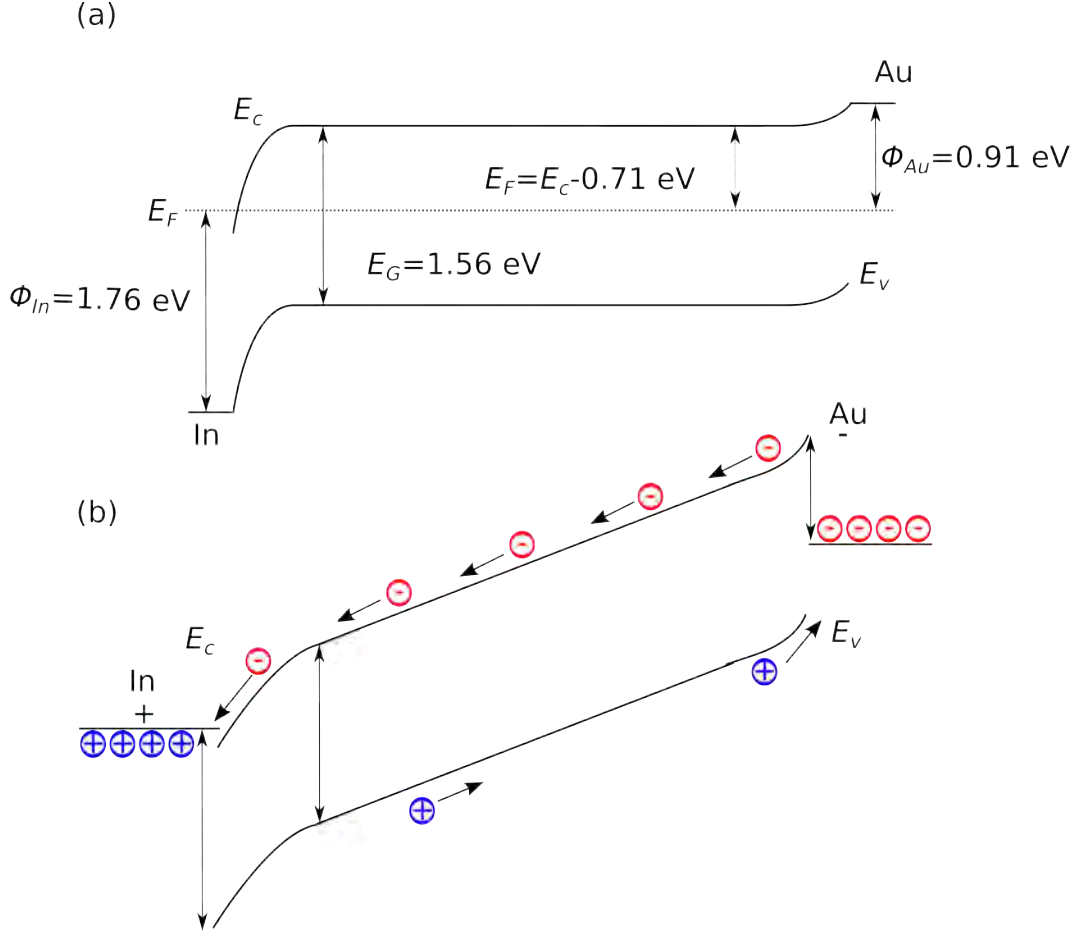
Figure 3.9: Energy diagram of In/CZT/Au structure without applied voltage (a) and with applied voltage in a reverse direction (b). Idealized model of work function difference.

Sample #7-CdZnTeSe

The I-V measurement of sample #7-CZTS bulk current in the range from -800 V up to $+800$ V at 300 K is shown in Figure 3.11(a). The sample resistivity was determined as $\varrho = 1.1 \times 10^{10}$ Ωcm (Figure 3.11(b)). The equation 3.1 was used to calculate the Fermi level position. The energy band-gap is 1.52 eV from ellipsometry measurement, and the sample conductivity (n-type) was observed by the thermoelectric power measurements. Hence, the determined Fermi level is related to the conduction band minimum at $E_F = E_c - 0.727$ eV.

The electric field profiles at ± 800 V were measured (Figure 3.11(d)) to clarify the determination of the Schottky barrier heights. The maximal electric field $\mathcal{E}_m$ occurs at the cathode for both bias polarities. The electric field decreases from the cathode to the anode, where its value is close to zero. It means that the Schottky barrier lowering at the anode for both polarities is nearly zero. On the other hand, the maximal electric field is at the cathode, and it causes the maximal Schottky barrier lowering, which creates the measured non-linearity in the I-V curve in Figure 3.11(a). We observed the linear dependence between $\ln(I)$ and $V^{1/4}$ which is shown in the range of $220 - 800$ V for both polarities in Figure 3.11(c). This effect allows to determine the Schottky barrier height at the metal-semiconductor interface when it acts as a cathode.
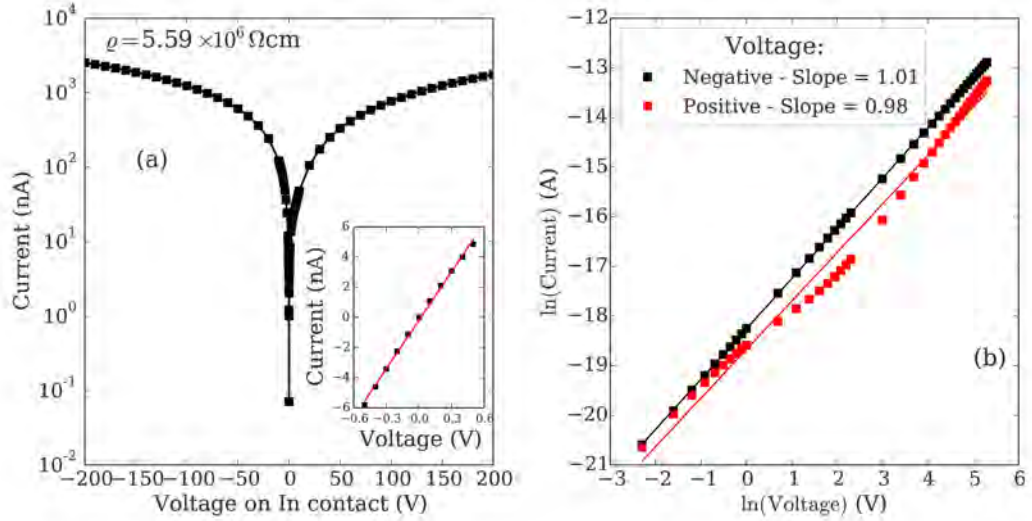
Figure 3.10: The I-V characteristic of a sample #6-CTS at 300 K. The resistivity was determined from the data depicted in the inserted graph using the Ohm's Law. The right graph shows that the dependence between current and voltage keeps Ohm's law in the whole measured voltage range.
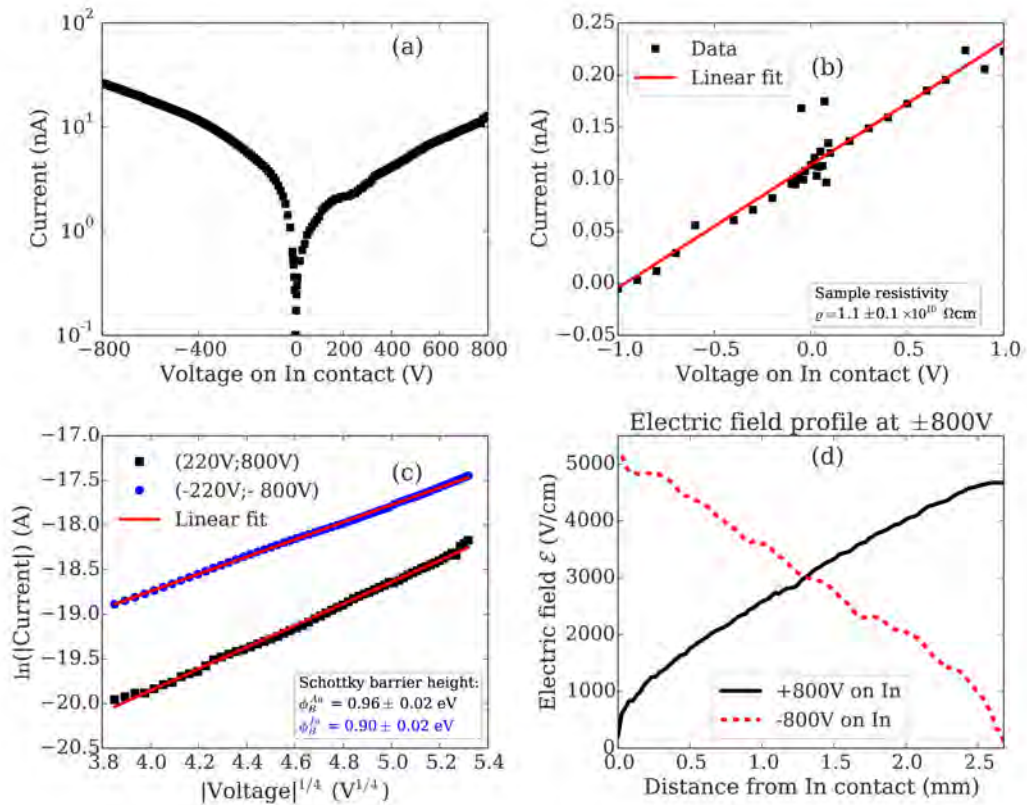
Figure 3.11: The I-V characteristics of In/CZTS/Au sample measured at 300 K (black squares) is plotted in Graph (a). Graph (b) shows the I-V curve around zero voltage with a linear fit (Ohm's law). The evaluated sample resistivity is $\varrho = 1.10 \times 10^{10}$ Ωcm. The Schottky barrier heights were computed using equation (1.57) from the experimental data (Graph (c)). The electric field profiles at ± 800 V are depicted in Graph (d). More information about the electric field profiles is in the section 3.3.1.

45

The current at high voltage is limited by the Schottky barrier height at both polarities. It means that the bands bend upwards at both interfaces (Au/CZTS and In/CZTS). We evaluated the Schottky barrier height at the Au/CZTS interface as $\phi_B^{Au} = 0.96 \pm 0.02$ eV and at the In/CZTS interface as $\phi_B^{In} = 0.90 \pm 0.02$ eV. The simplified band structure is shown in Figure 3.12.
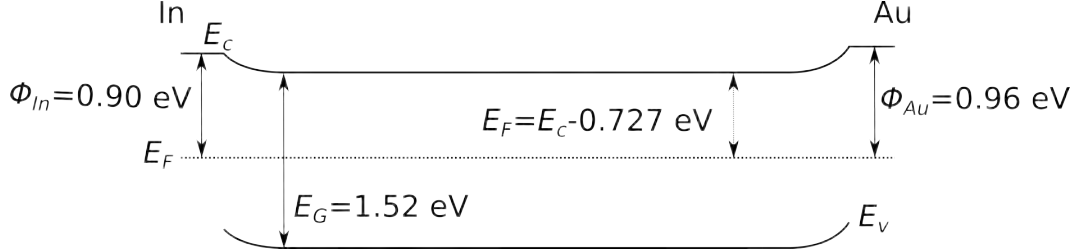
Figure 3.12: The simplified band structure of sample CZTS #7.

Summary

In summary, we found that the sample #6-CTS has low resistivity ($\varrho \approx 10^6$ Ωcm), which indicates that this material is not good for detector production. The resitivities of CdTe samples are in the range between $10^8 - 10^9$ Ωcm. The addition of Zn into CdTe matrix causes a higher resistivity (sample #4-CdZnTe $\varrho = 6.3 \times 10^9$ Ωcm) due to the larger energy band-gap ($E_G = 1.56$ eV) than CdTe ($E_G = 1.50$ eV) and better compensation of shallow defects. The sample #6-CdZnTeSe exhibits the highest resistivity $\varrho \approx 10^{10}$ Ωcm. However, the energy band-gap ($E_G = 1.52$ eV) is lower than the CZT energy band-gap. The fact that such a high resistivity was achieved at lower band-gap when compared to CZT indicates an excellent degree of compensation of shallow defects.

The determined sample resistivities and Fermi level positions are summarized in Table 3.2.

Table 3.2: Determined sample resistivities from I-V measurements and calculated Fermi level positions.

Sample	#1 CT:Cl	#2 CT:In	#3 CZT
ϱ (Ωcm)	2.05×10^9	2.49×10^8	1.00×10^9
E_F (eV)	$E_c - 0.68$	$E_c - 0.63$	$E_c - 0.67$

Sample	#4 CZT	#6 CTS	#7 CZTS
ϱ (Ωcm)	6.30×10^9	5.59×10^6	1.10×10^{10}
E_F (eV)	$E_c - 0.71$	$E_c - 0.53$	$E_c - 0.727$

The In contact bends the interface upwards in the case of the sample #7-CZTS, which is not consistent with the simple model based on the work function difference. This could be caused by the surface states which are not involved in the model.

In case of the Au contact, the barrier between Au and CdTe is almost Ohmic (band bending ≈ 30 meV). The CZT sample exhibits Schottky barrier height on

Au interface $\phi_B = 0.91$ eV, and for CZTS sample the barrier is higher $\phi_B = 0.96$ which more restricts the current in the reverse direction.

3.2 Low-temperature annealing in ambient air

3.2.1 Influence of low-temperature annealing on electric properties of samples

Low temperature annealing performed typically in the temperature range of $373 - 523$ K and its impact on properties of CdTe based materials and detectors has been investigated with so far controversial results. While Wang et. al. [107, 108] and Chattopadhyay et.al. [109] reported increase of leakage currents accompanied by deteriorated detection parameters, other authors observed decrease of leakage currents [110, 111, 112, 113]. Kim et. al. [112] studied the influence of the low-temperature annealing in air/vacuum on In/CdZnTe/Au samples with a chemical gold contact and with a gold contact formed by evaporation. They showed that the current decreased after the low-temperature annealing $(390 - 410$ K) in air on the sample with chemical gold contact due to an oxide layer creation below the gold contact. The same effect was shown by Mergui et. al. [113] who measured the effect of annealing in air on Au/CdTe interface. He observed that oxide penetrates under the contact and leads to a larger barrier height, which can explain the decrease of the leakage current. Kim also measured ^{241} Am gamma spectrum before and after low-temperature annealing and he showed the worsening of the FWHM from 10% to 12%. On the other hand, Park [111] showed that the FWHM is the same before and after low-temperature annealing at about 100 ° for 8 hours. Both used the planar configuration of detector, so they did not distinguish the bulk and the surface leakage current, which could affect the gamma spectra resolution. Pekárek et. al. [89] measured the passivation influence on detector performance and they showed improvement of both of the resolution and charge collection efficiency with lower surface leakage current. But the passivation only affects the surface conditions while the low-temperature annealing affects both the surface and the interface between semiconductor and metal. In our study we focused on very low annealing temperatures below 100° C to minimize thermal generation of bulk point defects, that could act as recombination and trapping centers and negatively influence spectral resolution and charge collection efficiency.

In this section we provide an insight on the influence of low temperature annealing in ambient air at even lower temperatures $313 - 373$ K covering in detail also the temperature range of standard operation conditions of detectors (typically up to 333 K). One of the reasons for observed differences of impact of low temperature annealing can be the influence of leakage currents flowing on the side surfaces of the sample. These currents strongly depend on the state of the surface that varies with type of passivation and time. Therefore we equipped the samples #1 and #2 with a guard ring contact structure, which allowed to separate bulk and surface leakage currents.

The samples #1 and #2 were annealed at temperatures $313 - 373$ K with an annealing step of 10 K in ambient air. They were kept at each annealing temperature T_a for 1 hour. Then the samples were cooled to room temperature,

at which I-V characteristic and ellipsometry measurements were performed. Then they were heated up again to the temperature of 10 K higher than the previous annealing temperature and the whole cycle was repeated.

As the primary research method, we used the measurements of I-V characteristics evolution with annealing. The bulk current and surface leakage currents were analyzed separately. The used measurement set-up is shown in Figure 2.6.

The results of I-V measurements performed on the sample #1 CdTe:Cl in the voltage range $(-200$ V,$+200$ V$)$ and the sample #2 CdTe:In $(-600$ V,$+600$ V$)$ at 300 K at different annealing temperature are presented in Figures 3.13 and 3.14. We separately show the bulk current I_B and the total current I_{TOT} that also includes the flow through the guard ring electrode and reflects the surface leakage current. The reason for the smaller measuring voltage range in the case of CdTe:Cl (Figure 3.13) was the significantly higher current in the forward direction compared to CdTe:In (Figure 3.14).
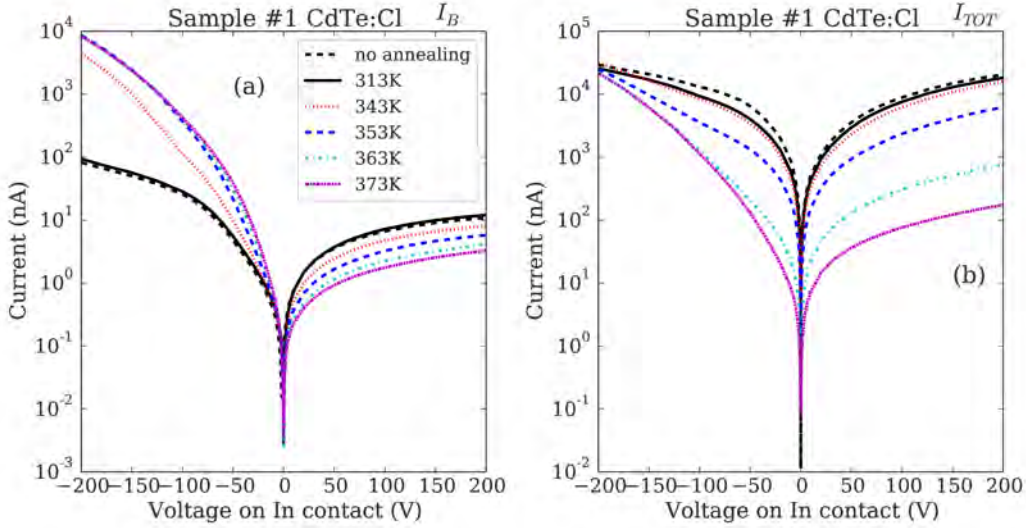
Figure 3.13: I-V characteristics of the sample #1-CdTe:Cl bulk current I_B and the total current $I_{TOT} = I_B + I_{GR}$.

The bulk current in the reverse direction (In - anode, Au - cathode) decreased with the increasing annealing temperature. In the case of forward current, an opposite effect was observed – the bulk current increased with the increasing annealing temperature. In order to understand this effect, we analyzed the I-V characteristics using the eq. (1.57) described in detail in section 2.2.

The corresponding profiles of $\ln(I)$ vs $U^{1/4}$ for voltages in the range of $50 - 200$ V for the CdTe:Cl sample and for CdTe:In sample in the range of $50 - 600$ V are presented in Figure 3.15. The Schottky barrier heights limiting the current flow are evaluated for both CdTe:Cl and CdTe:In samples and the dependence of the annealing temperature is presented in Figure 3.16. This figure also shows an increase of the Schottky barrier height with increasing temperature. The increase starts to be significant at annealing temperatures above 340 K and is stronger for the CdTe:Cl sample. This observation concludes that the Schottky barrier increase is responsible for the observed reduction of the bulk current I_B (Figure 3.16). The difference between the barrier height in CdTe:Cl and CdTe:In as-grown samples approximately corresponds to the position of the Fermi level in
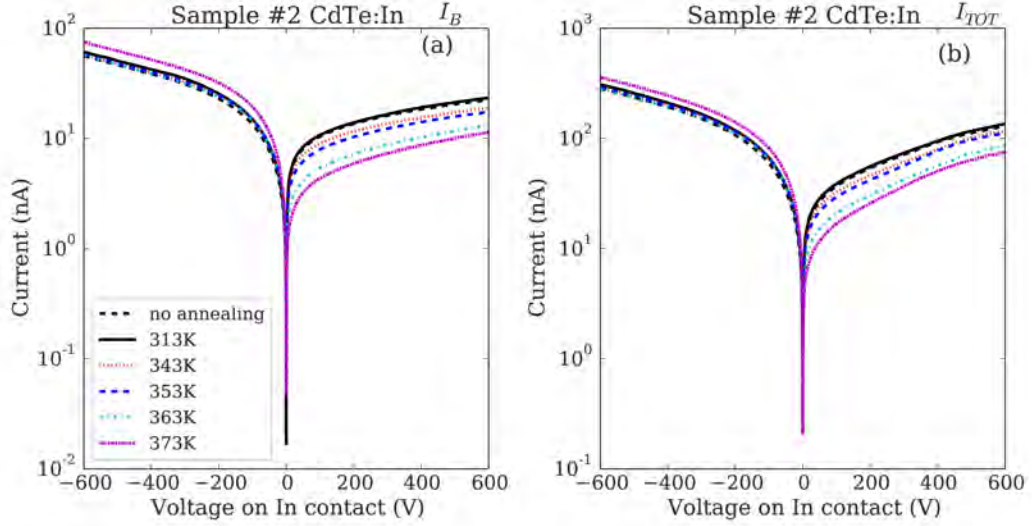
Figure 3.14: I-V characteristics of the sample #2-CdTe:In bulk current I_B and the total current $I_{TOT} = I_B + I_{GR}$.

these materials. We assume that the limiting Schottky barrier in the presented experiments is the Au/CdTe barrier. The Schottky barrier increase could be caused by the diffusion of oxygen under the gold contact [112].
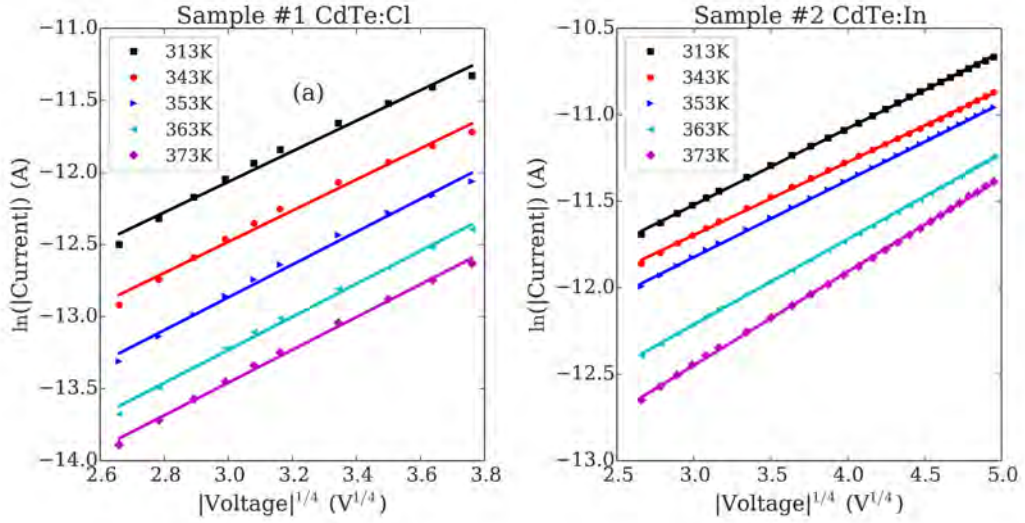
Figure 3.15: Dependence of $\ln(I)$ versus $U^{1/4}$ for the sample #1-CdTe:Cl (left) and sample #2-CdTe:In (right) with annealing temperature as a parameter.

To understand the origin of surface leakage currents I_{GR}, we investigated the side surfaces of the sample by ellipsometry after each annealing step. We measured the ellipsometry at room temperature immediately after cooling down from the annealing temperature.

The ellipsometry data at an incident angle of 60° in the range between 1.2 eV and 4.0 eV are depicted in Figure 3.17 with annealing temperature as a parameter. The results of ellipsometric measurements are summarized in Table 3.3 and Table 3.4 for sample #1 (CdTe:Cl) respectively sample #2 CdTe:In. The tables also
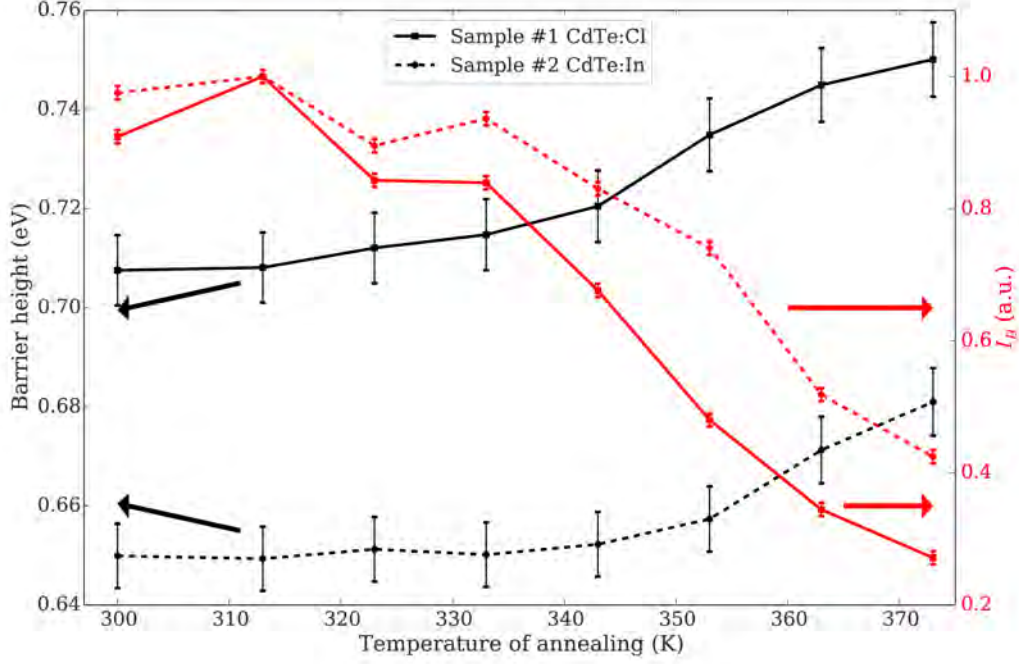
Figure 3.16: Dependence of the Schottky barrier height and normalized bulk current at 200 V on annealing temperature.

show the percentage distribution of Tellurium and TeO$_2$ in the EMA layer and the thickness of EMA and the surface roughness.

Table 3.3: Results of ellipsometric data analysis for Sample #1-CdTe:Cl.

T_a (K)	Thickness (nm)	Tellurium (%)	TeO$_2$ (%)	Roughness (nm)
313	2.8	0.0	65.9	9.1
323	4.0	0.0	63.2	9.3
333	4.0	1.7	61.1	9.4
343	4.9	8.1	57.3	10.0
353	5.4	9.4	55.2	10.4
373	4.7	5.0	58.3	10.6

Figure 3.18 shows the dependence of leakage current I_{GR} at +200 V and the effective TeO$_2$ thickness in the surface layer on the sides of the CdTe:Cl (a) and CdTe:In (b) samples on the annealing temperature. The effective TeO$_2$ thickness d_{TeO_2} is described by

$$d_{TeO_2} = \frac{F_{TeO_2}}{100} d_{ST}, \tag{3.2}$$

where F_{TeO_2} is the TeO$_2$ filling factor, d_{ST} is the surface thickness. This TeO$_2$ effective thickness would correspond to the ellipsometry signal if the surface consisted of only a flat tellurium oxide layer. It is apparent that the leakage current and TeO$_2$ thickness are well anticorrelated. Therefore, the experimentally observed decrease of the leakage current can be associated with increasing oxidation of the surface. We assume that the surface oxide layer modifies the surface leakage channels and/or results in depletion of the surface layer from majority

50
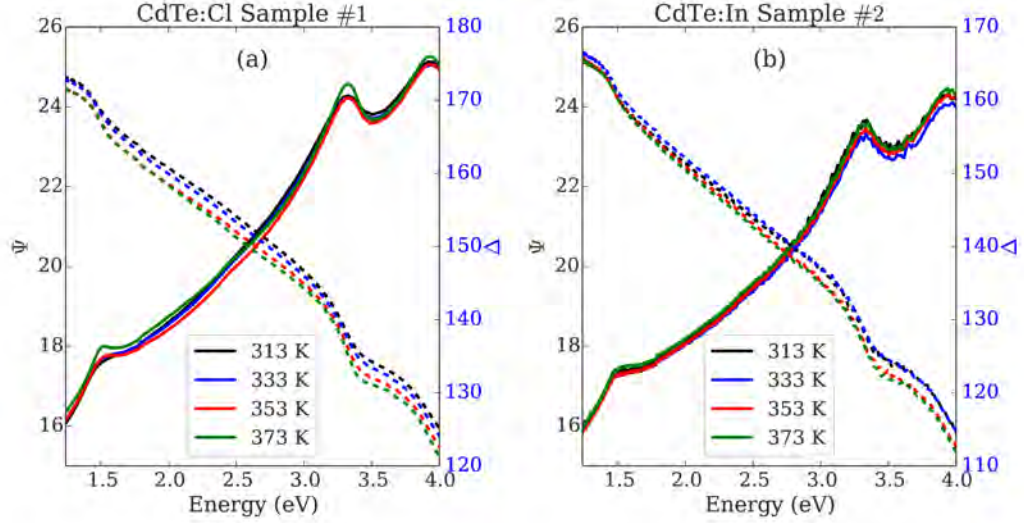
Figure 3.17: The annealing temperature dependence of the ellipsometry parameters Ψ and δ in the range between 1.2 eV and 4.0 eV.

Table 3.4: Results of ellipsometric data analysis for Sample #2-CdTe:In.

T (K)	Thickness (nm)	Tellurium (%)	TeO_2 (%)	Roughness (nm)
313	2.8	2.5	42.2	19.0
323	4.0	4.5	41.6	17.9
333	4.0	4.5	42.1	18.0
343	4.9	7.5	42.7	17.8
353	5.4	6.1	47.1	18.6
363	6.0	6.2	47.9	18.9
373	5.1	4.7	46.2	19.2

carriers.

The elemental Te is located on the CdTe surface layer [108, 114, 115], and its change is caused by oxidation of the surface and evaporation of Cd. The elemental Te is oxidized into TeO_2 [99, 116], which causes a decrease of the Te filling factor in the surface layer. On the other hand, the evaporation of cadmium from the CdTe surface [115] increases the Te filing factor and this associated with the Te filling factor maximum at about 350 K. The increasing oxide layer causes the growth of the surface roughness.

The presented results clearly show that low-temperature annealing at 300-373 K leads to a decrease in both the bulk and leakage currents. This effect is observed even at standard temperatures of detector operation 300-330 K and accelerates at $T > 340$ K.

3.2.2 Influence of low-temperature annealing under bias on the distribution of space charge

In this section we investigate the influence of the low-temperature annealing under bias with the goal to analyze, how the sample (#5-CZT) properties change at
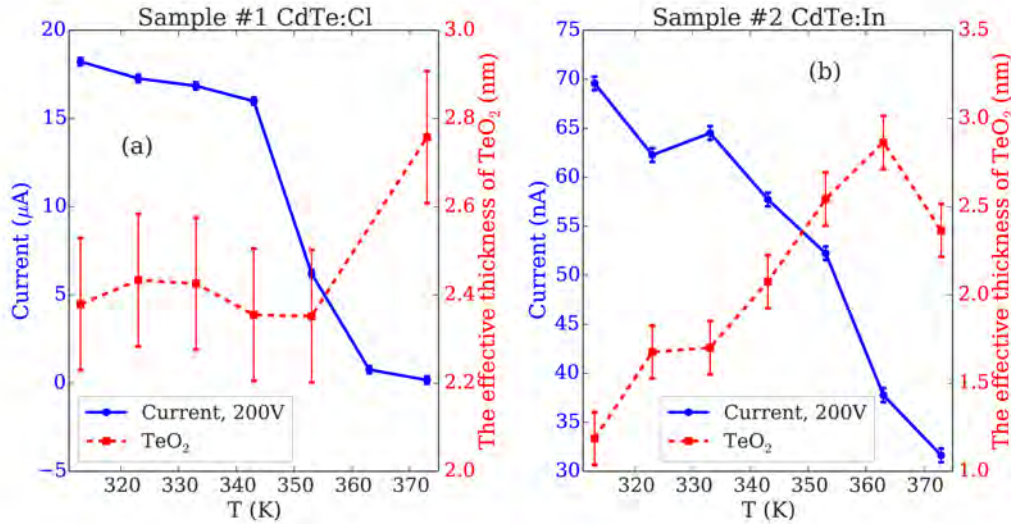
Figure 3.18: Room-temperature dependence of total current I_{TOT} at $+200$ V and the effective thickness of TeO_2 in the surface layer on sides of the sample #1 CdTe:Cl and sample #2 CdTe:In on annealing temperature.

standard operational conditions of detectors by using measurement of Pockels effect at 300 K. Typically the temperature of the CdTe detector during operation varies around room temperature (≈ 300 K). In some cases the temperature can increase up to ≈ 340 K or even more. The high temperature and high bias voltage (from 500 V up to 2000 V) can significantly change the space charge distribution, which leads to the change of the electric field profile and spectroscopic properties.
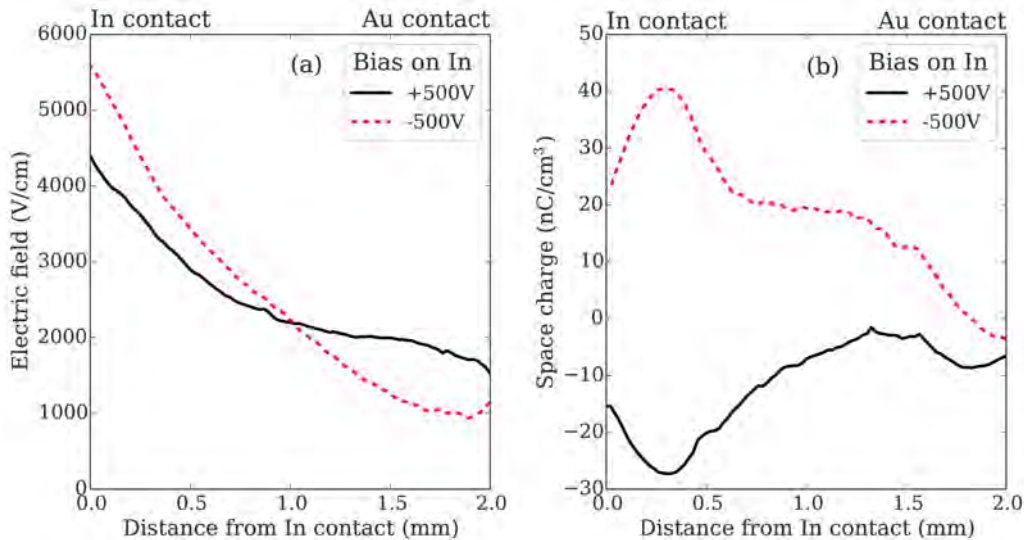
Figure 3.19: The profiles of the electric field at ± 500 V at 300 K are shown in graph (a). The graph (b) shows the distributions of the space charge in the sample #5-CZT.

The electric field at both polarities at temperature 300 K before any treatment is depicted in Figure 3.19(a). The numerically computed distributions of space charge from the electric field profiles are shown in Figure 3.19(b). The electric field decreases from the In anode to the Au cathode at bias $+500$ V on In contact.

Table 3.5: Parameters of the annealing steps

Step	Temperature (K)	Voltage (V)	Time (min)
1	373	+500	20
2	373	-500	120
3	373	-500	300
4	363	+500	180
5	363	-500	420

It shows that the negative space charge is present in the sample. The distribution of the space charge shows that the maximum of the negative charge is located approx. 0.3 mm below the In contact. The electric field also decreases from In cathode to the Au anode at bias -500 V. Therefore, the positive space charge is accumulated in the sample with a maximum value at the same distance below the In contact as in the case of the negative space charge at opposite bias.

The sample #5-CZT was treated with 5 different annealing steps (each of them defined by temperature, bias, and time) and after each step the electric field profiles at both polarities were measured at 300 K. The temperature, voltage, and time of each step are summarized in the Table 3.5.
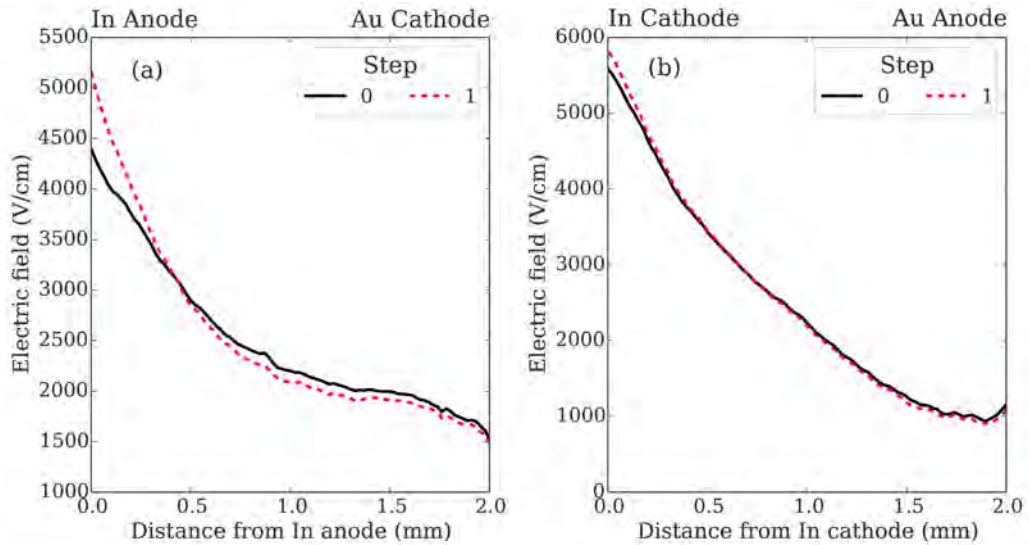
Figure 3.20: Graph (a) demonstrates the $\mathcal{E}$ profiles under bias $+500$ V at 300 K before and after the first step of annealing treatment (373 K; 20 min ;$+500$ V) in the sample #5-CZT. The electric field profiles at -500 V are depicted in graph (b).

In the first step, the sample was heated at 373 K and the bias $+500$ V on In contact was applied for 20 minutes. After that, the sample was cooled down to 300 K and the electric profiles were measured (Figure 3.20). The comparison between the electric profile at $+500$ V before and after first step (Figure 3.20) shows increase of the electric field under the In anode. It is caused by the increase of the negative space charge with a maximum just below the cathode (Figure 3.23). In the opposite polarity, the space charge distribution exhibits an increment of the positive space charge below the In contact.

In the second step, the bias -500 V on In contact was applied for 120 minutes
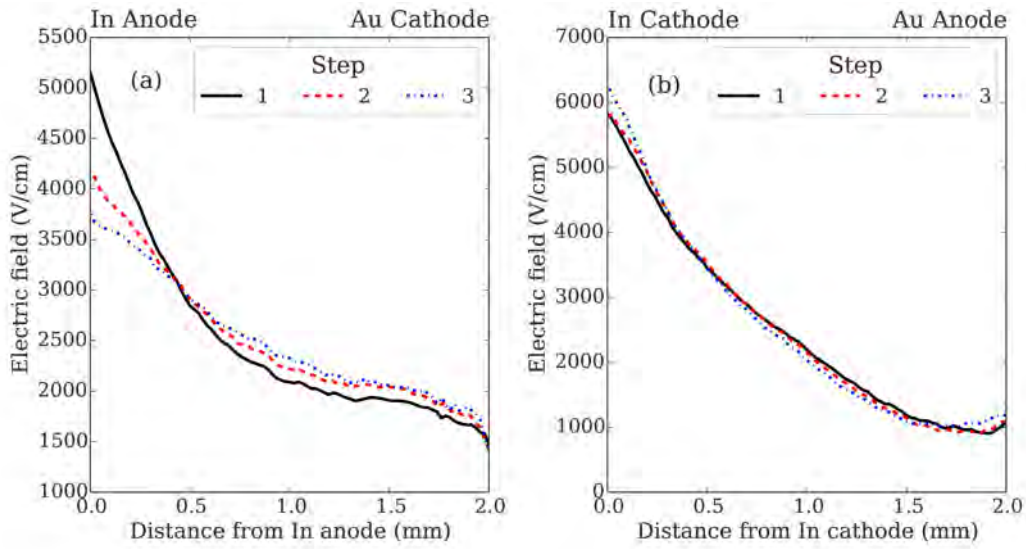
Figure 3.21: Graph (a) shows the electric field profiles under bias +500 V at 300 K after the first (373 K; 20 min; +500 V), second (373 K; 120 min; −500 V) and third step (373 K; 300 min; −500 V) of annealing treatment in the sample #5-CZT. The electric field profiles at −500 V are depicted in graph (b).
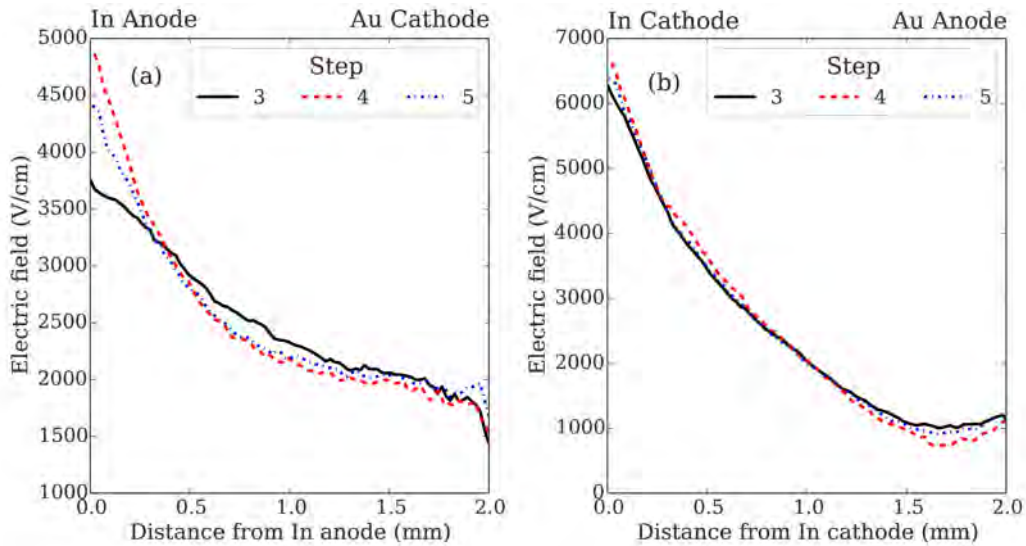
Figure 3.22: Graph (a) shows the electric field profiles under bias +500 V at 300 K after the third (373 K; 300 min; −500 V), fourth (363 K; 180 min; +500 V) and fifth step (363 K; 420 min; −500 V) of annealing treatment in the sample #5-CZT. The electric field profiles at −500 V are depicted in graph (b).
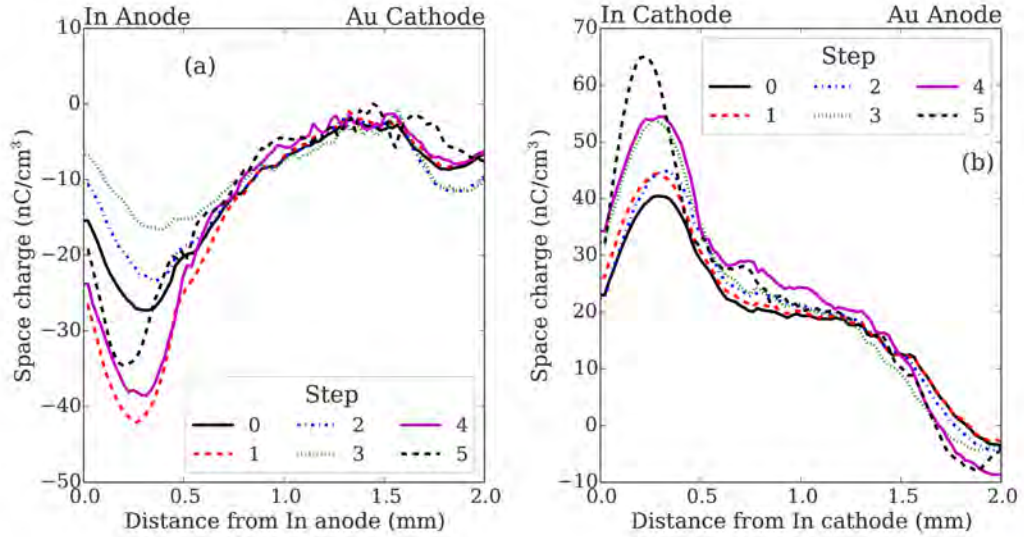
Figure 3.23: Graph (a) shows the distribution of the computed space charge from the electric profiles in sample #5-CZT under bias +500 V at 300 K. The space charge distributions at −500 V are depicted in graph (b).

at 373 K. Then the sample was cooled down without bias at 300 K where the electric field profiles were measured. The electric profile at +500 V returned into the initial state and the profile at −500 V is almost the same (Figure 3.21).

Next three steps (step 3-5 from Table 3.5) were investigated with results that the application of the positive voltage on In contact at temperature 363 K or 373 K causes formation of the negative space charge below the In contact. It leads to the higher polarization of the inner electric field at 300 K. On the other hand, the annealing at bias −500 V decreases the negative space charge in the sample (Figure 3.22).

In conclusion, the low-temperature annealing under bias causes the change of the space charge distribution (Figure 3.23). The main reason can be the electromigration of ions. This conclusion is supported by the apparent reversibility of the process. It will be studied in detail in future with other methods to describe the source of this behaviour. This effect can influence the performance of operating CZT detectors exposed to higher temperatures.

3.3 Analysis of deep levels using Pockels effect measurement

In this section we present a complex approach applying measurements and analysis of the Pockels effect in order to determine those deep levels in the material that substantially influence the charge transport.

At first we discuss the steady-state measurement of the inner electric fields with and without additional illumination. The results from infrared spectral scanning method are reported in the following subsection. The last subsection describes the temporal and temperature evolutions of the inner electrical field of samples #3, #4 and #7 which were measured in the temperature range between 275 K and 330 K with a step of 5 K.

The results of this work were published in articles [100, 117, 102]

3.3.1 Temperature dependence of the electric field profiles

We used the set-up for steady-state measurements (Figure 2.1) to measure the temperature dependence of the electric field profiles $\mathcal{E}(x)$ in samples #3, #4 and #7. The applied voltage was 500 V for sample #3 and #4. The sample #7 was measured with bias 800 V. We measured the electric fields at different temperatures $\mathcal{E}(x,T)$ between 275 K and 330 K with a step of 5 K. The selected $\mathcal{E}(x,T)$ of samples #3, #4 and #7 are shown in Figures 3.24, 3.25 and 3.26, respectively.
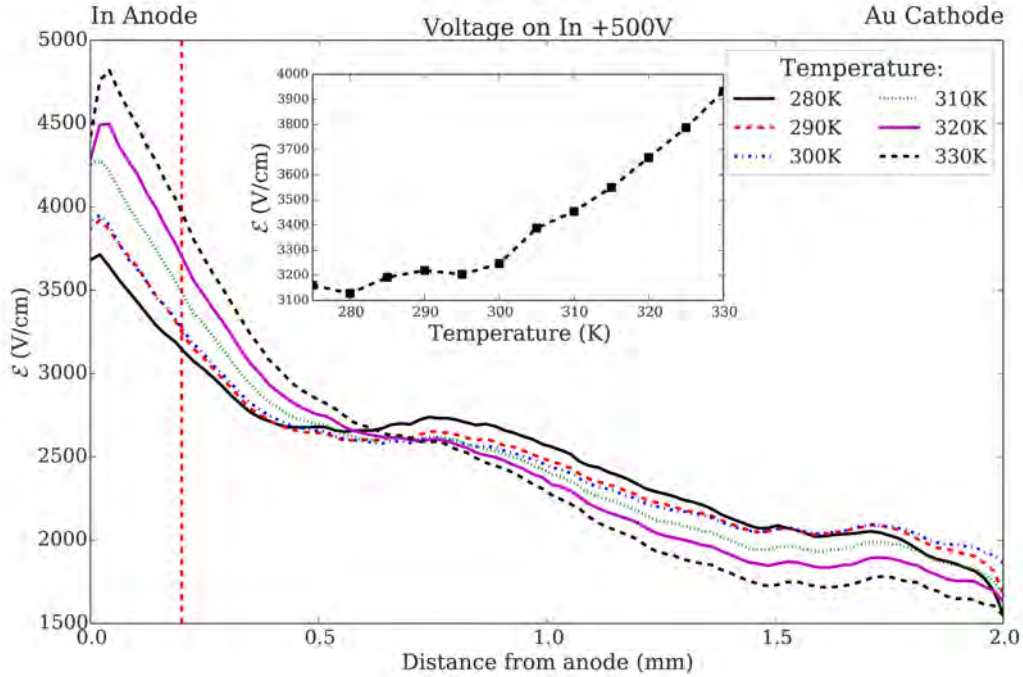
Figure 3.24: Profiles of the electric field in the sample #3-CZT at 500 V applied on In contact at different sample temperatures. Dashed vertical red line shows the position where the data are taken for the insert graph.

The $\mathcal{E}(x,T)$ profiles of samples #3-CZT and #4-CZT almost linearly decrease from the anode to the cathode, because there is a negative space charge in the sample due to a band bending at the In anode (see band structure in Figure 3.9). There is a difference in temperature dependence between samples #3-CZT and #4-CZT. The sample #4-CZT does not exhibit strong temperature dependence of the $\mathcal{E}$, while the $\mathcal{E}$ of sample #3-CZT is more accumulated under the anode with increasing temperature (see inset graph in Figure 3.24). It means that the negative space charge in the sample grows with temperature.

The $\mathcal{E}(x,T)$ profiles of sample #7-CZTS are depicted in Figure 3.26. The profiles linearly increase from the anode to the cathode. The slope of profiles is caused by the presence of the positive space charge in the sample. The amount of the positive space charge is not dependent on temperature (see inset graph in Figure 3.26).
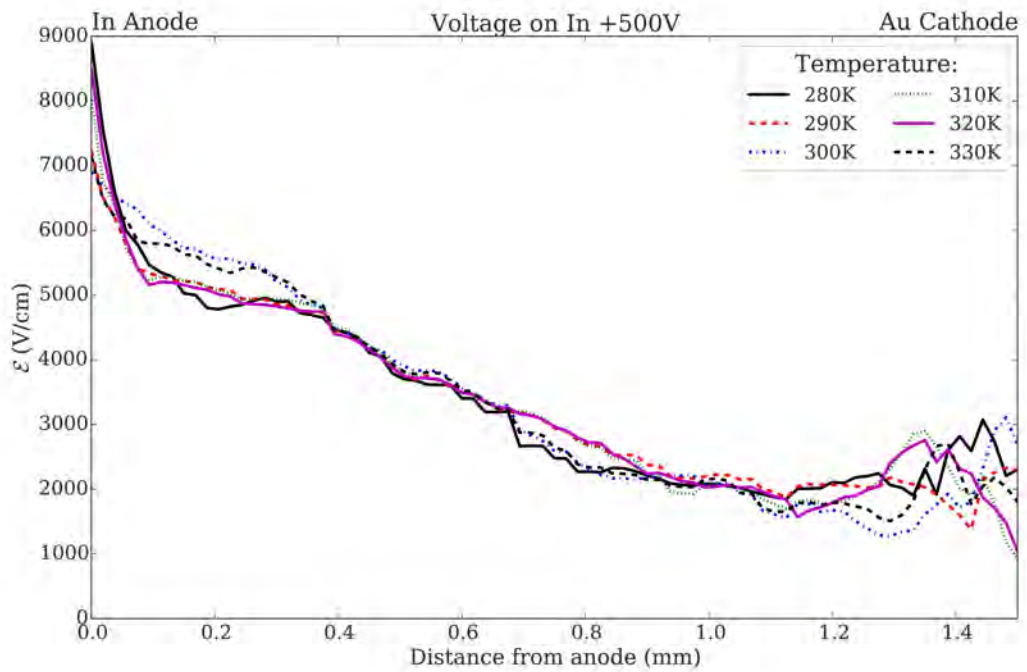
Figure 3.25: Profiles of the electric field in the sample #4-CZT at 500 V on In contact at different sample temperatures.
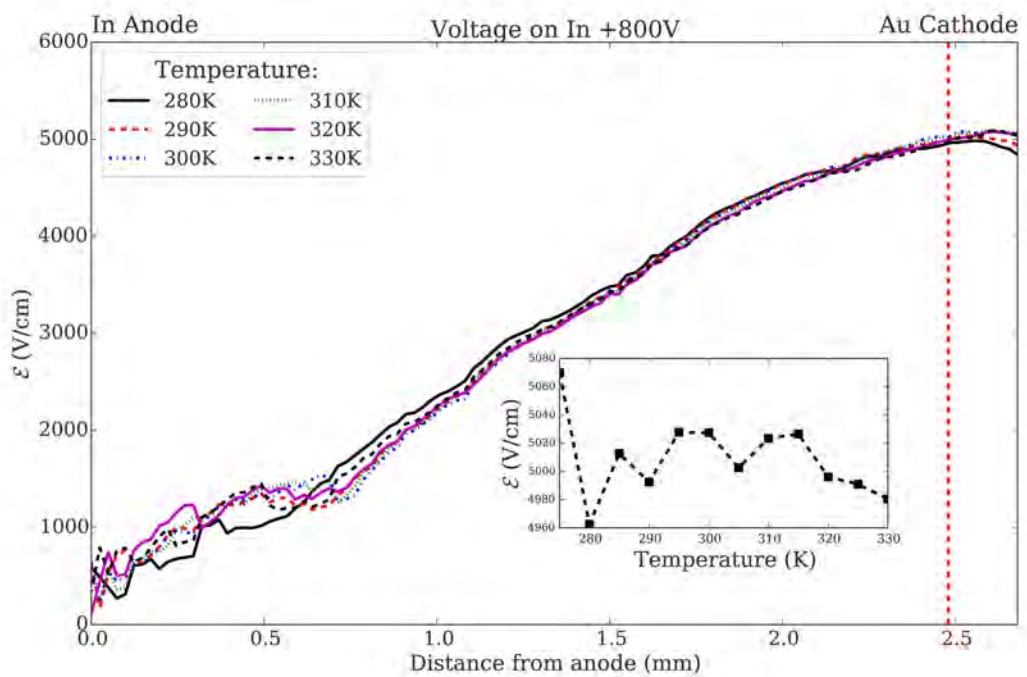
Figure 3.26: Profiles of the electric field in the sample #7-CZTS at 800 V on In contact in dependent on temperature. The dashed vertical red line shows the position where the data are taken for the insert graph.

In summary, the measured CZT samples contain negative space charge in the steady-state of the electric field after application the bias. It means that the electric field decreases from the In anode to the Au cathode due to space charge caused by band bending at the metal-semiconductor interfaces. We suppose that In contact plays a main role in this effect because the space charge is negative which correspond to band bending downwards.
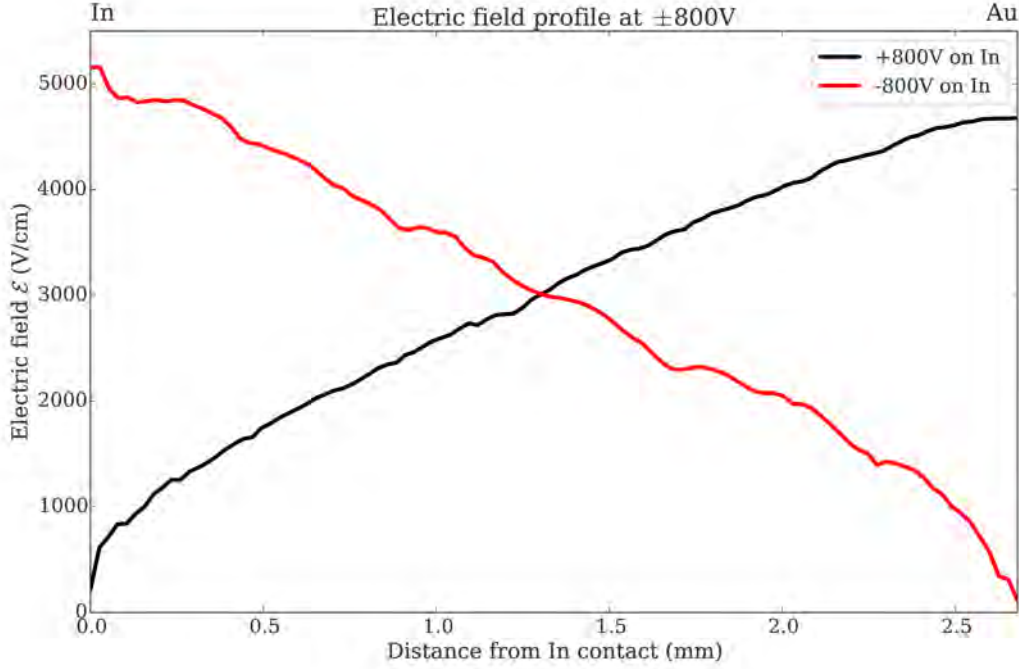
Figure 3.27: Profiles of the electric field in the sample #7-CZTS at ±800 V on In contact at 300 K.

On the other hand, the electric field increases from the In anode to the Au cathode in the CZTS sample. It means that the positive space charge is present on the deep levels. It can be caused by the band bending at both contacts upwards (see band structure in Figure 3.12).

We measured $\mathcal{E}(x)$ of the sample #7-CZTS at both polarities ±800 V (Figure 3.27) due to a presence of the opposite space charge in the sample at reverse polarity (positive bias at In contact) in comparison with CZT samples. The electric field at −800 V decreases from an In contact (cathode) to an Au contact (anode) which points to the positive space charge in the sample. It is caused by the band bent upwards at In contact in the case of this sample.

There is also difference in temperature dependence of the electric fields. The CZTS sample #7 does not exhibit any temperature dependence while the electric fields in the CZT samples are dependent on temperature. It points at the different properties of deep levels in the CZT and CZTS material. Also, it shows that electrical properties of CZTS material are temperature stable which is promising for future application as a detector. The temperature stability of the sample #7-CZTS could be caused by the larger energy distance between deep levels responsible for space charge and the Fermi level in comparison with CZT samples. Also, these level could have lower concentrations in the case of CZTS sample. Then the probability of the capture of a thermally excited electron is decreased.

3.3.2 Evolution of the inner electric field after application of the bias

The temperature and temporal evolutions of the internal electric field $\mathcal{E}(t,T)$ of samples #3-CZT, #4-CZT and #7-CZTS after application of the bias were measured in order to determine the deep levels responsible for the formation of the space charge. The measurements and results are split into three paragraphs describing each sample separately.

Sample #3-CdZnTe

The $\mathcal{E}(t,T)$ profiles of the sample #3-CZT after application of bias 500 V were monitored using the set-up for measuring Pockels effect in regular regime with InGaAs camera (Figure 2.1). The temperature range was $280 - 330$ K with a step of 5 K, and the time resolution of the electric field measurement was 30 ms.

The selected $\mathcal{E}(x,t)$ profiles between electrodes measured at 300 K are shown in Figure 3.28.
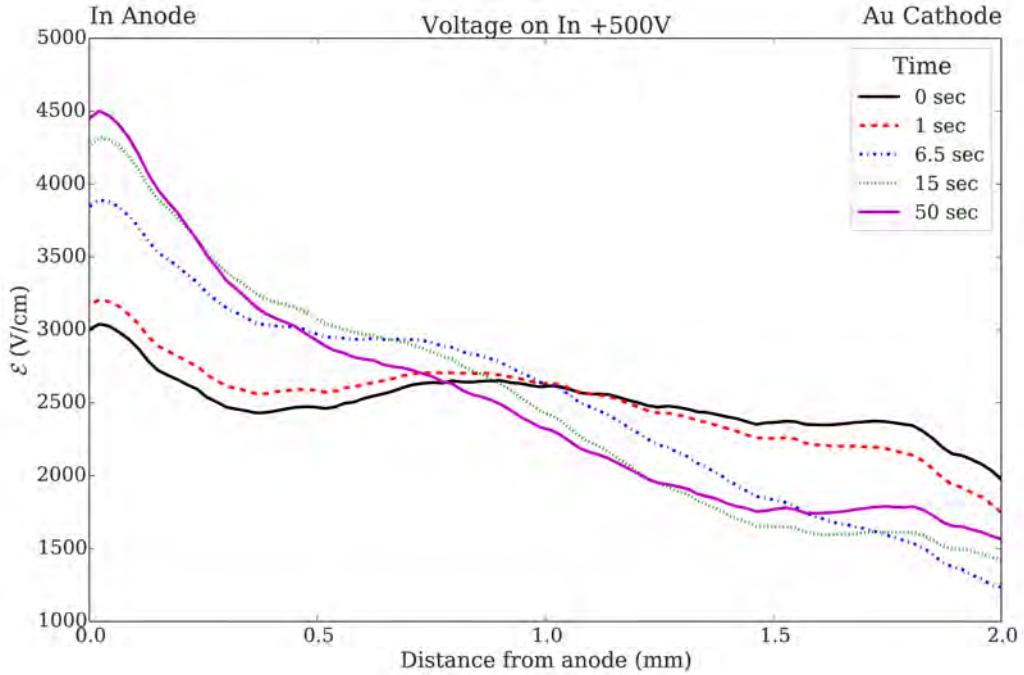
Figure 3.28: Selected $\mathcal{E}(x,t)$ profiles in sample #3-CZT after application of 500 V on the In contact at the temperature 300 K.

From the electric field distribution at each time point, we evaluated a total space charge Q as

$$Q = \int_V \rho(x)dV = S \int_a^c \rho(x)dx, \qquad (3.3)$$

where V is the sample volume, S is the electrode area, and $\langle a, c \rangle$ is the interval of the distance along the sample thickness between the anode and the cathode. $\rho(x)$ is the space charge density derived from the electric field distribution $\mathcal{E}(x)$ which varies along only one direction between the electrodes x using Gauss law (equation (1.24)).

Combining equations (3.3) and (1.24), we get a simple expression for the total space charge

$$Q = \varepsilon S \left(\mathcal{E}_c - \mathcal{E}_a \right), \tag{3.4}$$

where $\mathcal{E}_c$ and $\mathcal{E}_a$ are the electric fields at the cathode and the anode, respectively. The time evolution of electric field under the cathode $\mathcal{E}_c$ the anode $\mathcal{E}_a$ and calculated space charge at 300 K are depicted in Figure 3.29.

There is an apparent undershoot of $\mathcal{E}_c$ for time smaller than 10 s, while $\mathcal{E}_a$ has monotonous time evolution. Space charge Q reaches a negative steady-state value $Q^\infty \approx -7.5 \times 10^{-10}$ C in a few tens of seconds after biasing.

The time evolution of the total space charge was fitted by a single exponential decay

$$Q(t) = A \exp\left(-\frac{t}{\tau}\right) + Q^\infty. \tag{3.5}$$
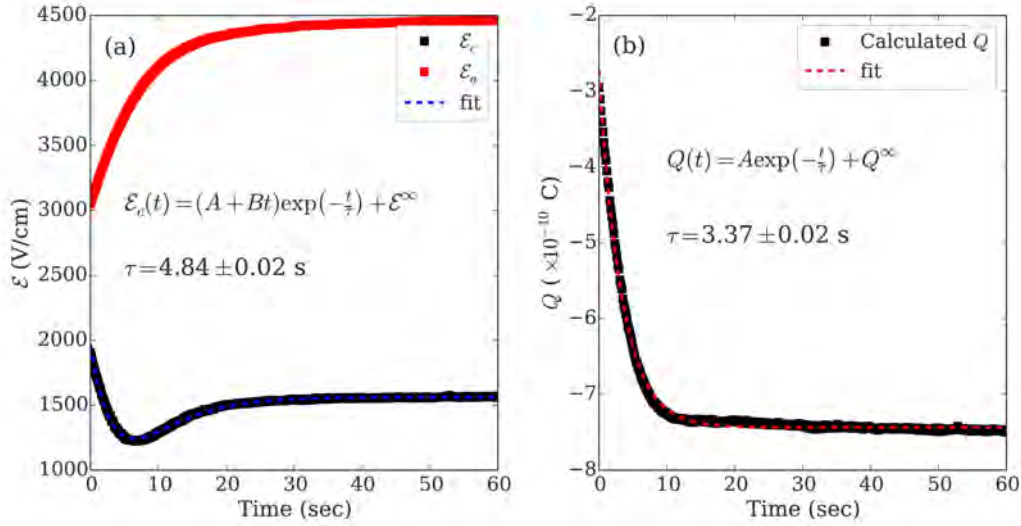
Figure 3.29: Time evolution of electric field under the cathode and the anode in the sample #3-CZT after application of the voltage of 500 V at 300 K. The evolution of the calculated total space charge is depicted in the right graph.

The obtained time constants τ denote the thermally activated process. The Arrhenius plot of τ is shown in Figure 3.30(b).

If only one transition process between bands and a single dominant deep level E_t is considered, the observed thermally activated increase in the negative space charge $Q(t)$ is related to the hole emission which is a thermally activated transition of the valence electrons to the deep level. On the other hand, the electron capture from the conduction band to the deep level, which should also lead to an increase in the negative space charge, is not thermally activated. Thus, the activation energy acquired from the Arrhenius analysis should be calculated from the bottom of the valence band E_v, and, in this case the capture cross-section belongs to holes (σ_p). Thus, the deep level energy $E_t = E_v + (0.868 \pm 0.004)$ eV was obtained from the slope of the Arrhenius plot, and from the intersect with the vertical axis we evaluated the hole capture cross section $\sigma_p = 2.5 \times 10^{-13}$ cm^2.

In order to analyze local oscillation of the electric field under the cathode, we have chosen the position at 1.8 mm from the anode $\mathcal{E}_{1.8mm}$ (0.2 mm below
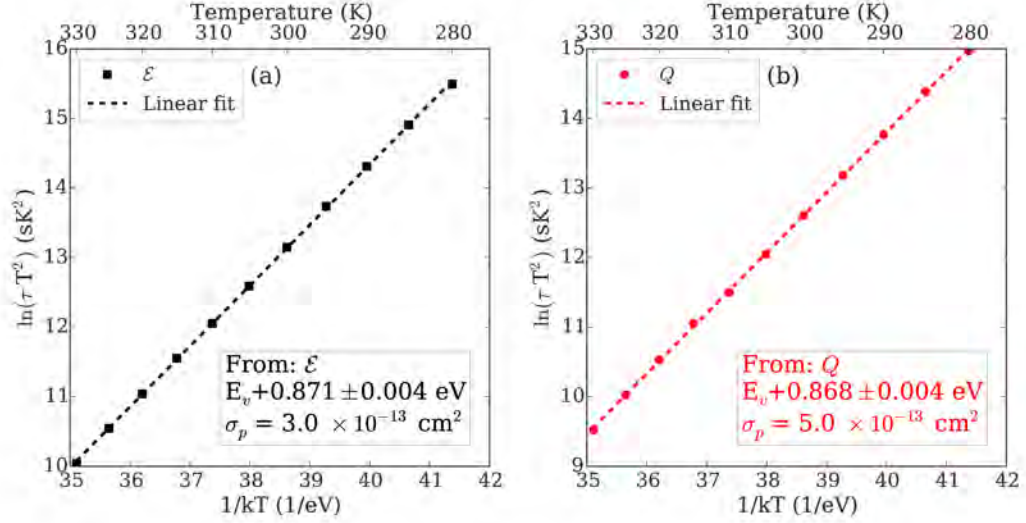
Figure 3.30: Arrhenius plots of τ of $\mathcal{E}_{1.8mm}$ (graph (a)) and total space charge Q (graph (b)) with corresponding linear fit (dashed lines).

the cathode). $\mathcal{E}_{1.8mm}$ at the temperature 300 K is shown in Figure 3.29. For determination of thermal emission constant τ, we used the fitting function

$$\mathcal{E}_{1.8mm}(t) = (A + Bt)\exp\left(-\frac{t}{\tau}\right) + \mathcal{E}^{\infty}, \qquad (3.6)$$

which describes a critically damped oscillation of the electric field. A, B, τ, and $\mathcal{E}^{\infty}$ are the fitting parameters. Fitting using equation (3.6) was chosen because it is the simplest function describing the observed undershoot.

The Arrhenius plot of τ obtained from temporal and temperature evolutions of $\mathcal{E}_{1.8mm}$ is shown in Figure 3.30(a). The obtained values of $E_t = E_v + (0.871 \pm 0.004)$ eV and $\sigma_p = 1.7 \times 10^{-13}$ cm^2 are in a good agreement with values obtained from temporal and temperature evolutions of Q. Thus the direct relation between the local electric field oscillation and the thermal emission from the single deep level is confirmed.

Sample #4-CdZnTe

The modified set-up for fast time measurements (Figure 2.2(b)) was used to measure the $\mathcal{E}(t, T)$ evolutions in the sample #4-CZT after switching on the bias voltage 500 V. The temperature was varied between 275 K and 335 K with a step of 10 K.

The $\mathcal{E}(t)$ evolution under the Au cathode after application of the bias at 305 K is plotted in Figure 3.31(a). The electric field under the cathode is in arbitrary units.

The $\mathcal{E}(t)$ evolution under the cathode exhibits undershoot in the time range below 2 seconds. We applied the equation (3.6) describing a critically damped oscillation for determining the time constant τ. It was used due to the similar steady-state electric field under bias and also due to the similar time evolution of the electric field under the cathode as we observed on sample #3. The mismatch between experimental data and fit is caused by the used modified set-up because

this measurement method averages the electric field evolution from the small area below the cathode. Then the measured signal is deformed.

At first the electric field increases within 0.2 s after application of the bias. This time interval is in Figure 3.31 presented by a red dashed line. Then its evolution consists of two phases. During the first phase, $\mathcal{E}(t)$ under the cathode descends. It corresponds to the increase in the negative space charge. During the second phase, $\mathcal{E}(t)$ increases, which corresponds to the decrease in the negative space charge. The obtained time constant from fitting describing the critically damped oscillation is 1.23 ± 0.04 sec at 305 K.
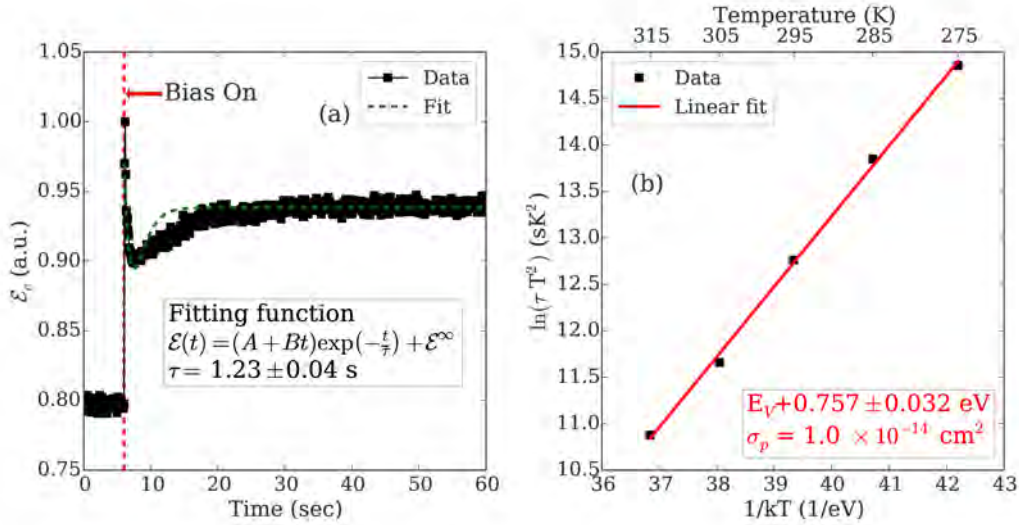
Figure 3.31: Time evolution of the electric field under the cathode in the sample #4-CZT after application of the voltage of 500 V at 305 K is shown in the left graph. The right graph shows the Arrhenius plot with the evaluated activation energy and corresponding capture cross-section.

The temperature dependence of this time constant was measured with a step of 10 K ranging between 275 and 335 K. The equation (1.45) was used to determine the activation energy of the thermally activated transition and its capture cross-section. The corresponding Arrhenius plot is depicted in Figure 3.31. The time dependence was obtained in the temperature range between 275 K and 315 K. We evaluated the activation energy $E_v + (0.757 \pm 0.032)$ eV with capture cross-section $\sigma_p = 1 \times 10^{-14}$ cm^2. We attribute it to electron transitions from the valence band to the level due to the presence of the negative space charge and its increase with T in the sample #4 (Figure 3.25).

Sample #7-CdZnTeSe

The $\mathcal{E}(x, t)$ evolution in the sample after the bias application was measured in the temperature range between $280 - 330$ K. The selected profiles of $\mathcal{E}(x, t)$ are shown in Figure 3.32. The electric field in the steady state indicates a formation of a positive space charge in the sample due to the band bending at the Au/CZTS interface upwards.

The $\mathcal{E}(t)$ evolution under the cathode at 300 K is plotted in Figure 3.33(a).
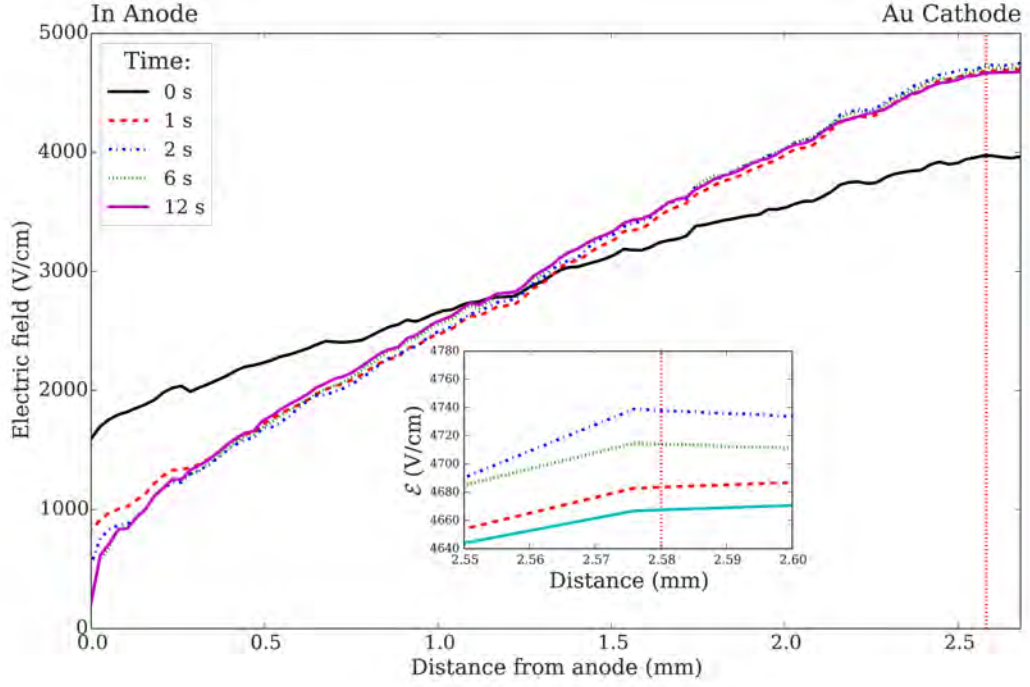
Figure 3.32: Selected electric field profiles of sample #7-CZTS after bias application. The red dotted vertical line shows the position, where time evolution of $\mathcal{E}(t)$ was extracted and evaluated.

The time evolution of the space charge Q was computed for a better understanding of the inner electric field development by the formula (3.4).

When doing the same measurement on CZT sample #3 (subsection 3.3.2) we observed the undershoot in the time evolution of the electric field under the cathode, but the $Q(t)$ was described by a single-exponential function. Such a behaviour can be described as critically damped oscillation of the electric field caused by local space-charge fluctuations including changes of occupation on just one deep level. However, in the case of CZTS, the time evolution of the space charge (Figure 3.34(a)) exhibits a similar overshoot as the evolution of the electric field (Figure 3.33(a)). We could not explain this effect using a model with just one deep level. Therefore, we applied a fit of the experimental curves by a double-exponential function and interpreted it by a model that includes two deep levels.

The activation energies of the levels E_i were evaluated from the $\tau_i(T)$ describing the $\mathcal{E}(t)$ evolution under the cathode and space charge evolution by an Arrhenius equation (1.45).

An activation energy of 0.82 ± 0.04 eV was determined from the temperature dependence of τ_1 describing the increase of the electric field under the cathode (black squares in Figure 3.33(b)). This process can be described by a thermal transition of electrons from the deep level to the conduction band resulting in the observed increase of the positive space charge. Therefore, the activation energy was assigned to the deep level $E_c - 0.82 \pm 0.04$ eV with electron capture cross section $\sigma_n = 1.0 \times 10^{-11}$ cm^2.

The time constant τ_2 describes the decrease of the electric field under the cathode, which correlates with the electron transition from the valence band to the deep level. The data are plotted as black circles in Figure 3.33(b). The

63
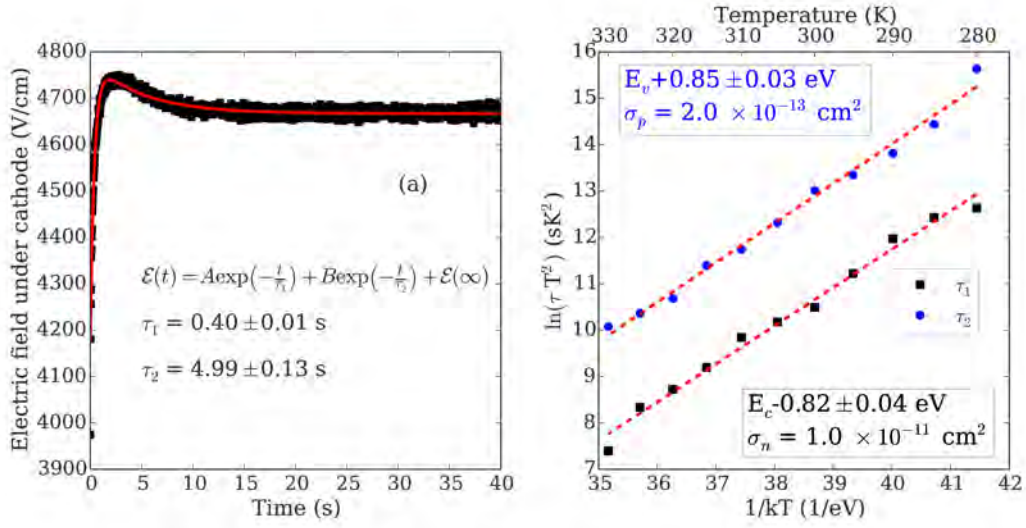
Figure 3.33: The time evolution of the electric field at $T = 300$ K in the sample #7-CZTS is plotted in the graph (a). The experimental data (black square) are fitted by a double-exponential function (red line) with time constants $\tau_1 = 0.40 \pm 0.01$ s and $\tau_2 = 4.99 \pm 0.13$ s. The Arrhenius diagram is plotted in the graph (b). The observed deep level energies $E_c - 0.82 \pm 0.04$ eV with electron capture cross-section $\sigma_n = 1.0 \times 10^{-11}$ cm^2 and $E_v + 0.85 \pm 0.03$ eV with hole capture cross-section $\sigma_p = 2.0 \times 10^{-13}$ cm^2 were calculated from time constants describing the electric-field evolution.
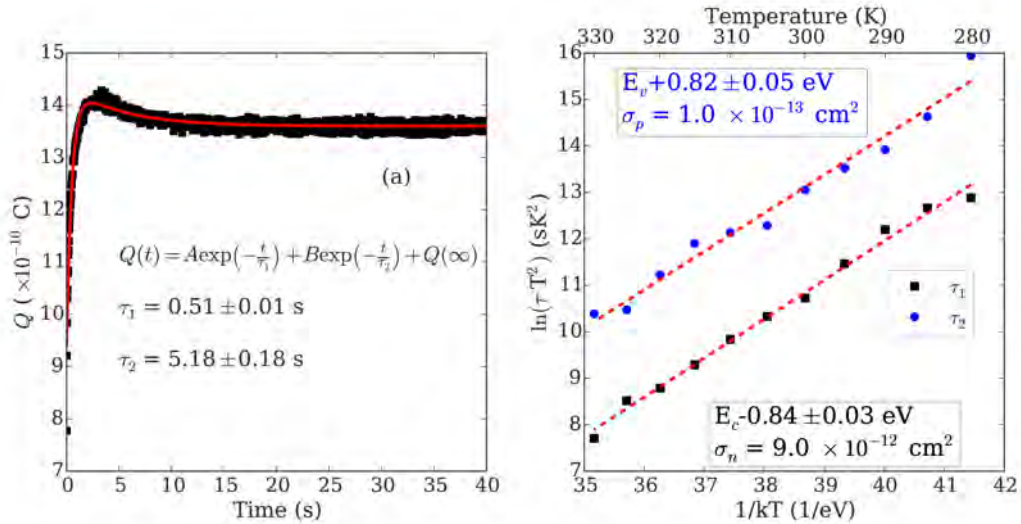
Figure 3.34: The space charge evolution of the sample #7-CZTS at $T = 300$ K in time is shown in graph (a). The data are shown as black squares, and the double-exponential fit with time constants is plotted as a red line. The graph (a) includes the determined time constants $\tau_1 = 0.51 \pm 0.01$ s and $\tau_2 = 5.18 \pm 0.18$ s. The Arrhenius diagram is plotted in the graph (b). The deep levels determined from space charge evolution are $E_c - 0.84 \pm 0.03$ eV with electron capture cross-section $\sigma_n = 9.0 \times 10^{-12}$ cm^2 and $E_v + 0.82 \pm 0.05$ eV with hole capture cross-section $\sigma_p = 1.0 \times 10^{-13}$ cm^2.

determined deep level is $E_v + 0.85 \pm 0.03$ eV with hole capture cross section $\sigma_p = 2.0 \times 10^{-13}$ cm^2.

We performed the Arrhenius analysis on time constants describing the space-charge evolution. The time constant τ_1 related to the increase of positive space charge leads to the deep level $E_c - 0.84 \pm 0.03$ eV with electron capture cross section $\sigma_n = 9.0 \times 10^{-12}$ cm^2 (black squares in Figure 3.34(b)). The analysis of the time constant τ_2 (black circles in Figure 3.34(b)) provides the deep level $E_v + 0.82 \pm 0.05$ eV with capture cross-section of holes $\sigma_p = 1.0 \times 10^{-13}$ cm^2 (decrease of the positive space charge). We conclude that both methods of evaluation (electric field and total space charge) lead to the same results within the expected experimental error.
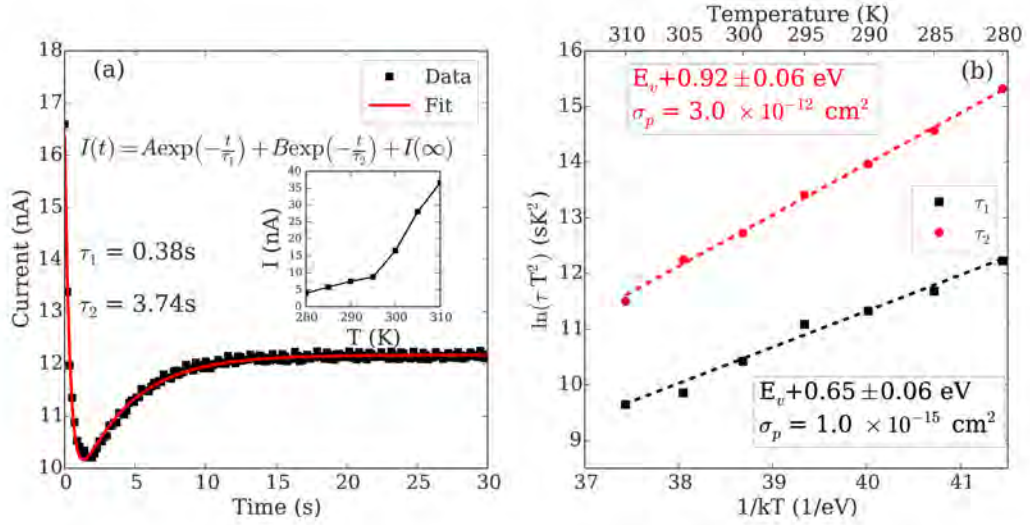
Figure 3.35: The graph (a) shows the sample #7-CZTS time evolution of the measured electric current after switching on the bias at temperature 300 K. The Arrhenius diagram is plotted in the graph (b). The observed deep-level energies are $E_v + 0.65 \pm 0.06$ eV with hole capture cross-section $\sigma_p = 1.0 \times 10^{-15}$ cm^2 and $E_v + 0.92 \pm 0.06$ eV with hole capture cross-section $\sigma_p = 3.0 \times 10^{-12}$ cm^2.

The results from the Pockels measurement were supplemented with measurements of the electric current time evolution. Figure 3.35(a) shows $I(t)$ after switching on the bias at temperature 300 K. The current decreases within the first two seconds with the time constant $\tau_1 = 0.38$ sec. It is the same time constant with which the electric field below the cathode increases (Figure 3.33(a)). The build-up of positive space charge is thus accompanied by a decrease in the electric current. The Arrhenius analysis of the time constant τ_1 (Figure 3.35(b)) gives energy of 0.65 eV and carrier capture cross-section of 1×10^{-15} cm^2. This energy is complementary to the electron trap $E_c - 0.83$ eV. The sum $0.83 + 0.65$ eV agrees within the experimental error with the band-gap of the material at 1.52 eV as measured by ellipsometry (Table 3.1). This energy is therefore probably connected with thermally activated emission of holes from the valence band to the level causing that the absolute value of the electric current increases immediately after switching on the bias with temperature (from 5 nA at 280 K to 37 nA at 310 K see insert graph in Figure 3.35(a)).

In summary, within the first two seconds after application of the bias, the positive space charge is built up by electron transitions from this level to the conduction band. At the same time, free holes are trapped at the level decreasing the electric current, which therefore seems to be composed mainly of holes. After the initial decrease, the electric current starts to increase with time constant $\tau_2 = 3.74$ sec at 300 K. An Arrhenius analysis of this time constant gives activation energy of 0.92 eV. With a similar activation energy and time constant, the electric field below the cathode decreases (positive space charge decreases - Figure 3.34(a)). Therefore, we conclude that the observed increase of the electric current is caused by an emission of holes from the level $E_v + 0.83$ eV. Corresponding transitions of electrons from the valence band to the level cause the decrease of the positive space charge.

There is a difference in deep levels responsible for time evolution of the inner electric field after application of bias between sample #3-CZT and #7-CZTS. It is evident that CZT contains one main deep level affecting time evolution due to the mono-exponential decay of the total space charge time evolution (Figure 3.29(b)). On the other hand, time evolution of the total space charge in CZTS sample exhibits double-exponential character (Figure 3.34), which can be described by a model with two deep levels.

3.3.3 Infrared spectral scanning

The set-up shown in Figure 2.2(a) was used to scan the spectral dependence of the samples #3-CZT and #7-CZTS electric field profiles in the range between 900 and 1800 nm with a constant photon flux 1.0×10^{15} photons cm^{-2}s^{-1}.

Sample #3-CdZnTe

The selected $\mathcal{E}(x)$ profiles are depicted in Figure 3.36 as a function of the wavelength of illuminating light. The negative space charge is present in the sample without illumination due to the band bending downwards at the In anode. The distribution of the space charge is changed with NIR light, which penetrates through the sample volume.

The dependence of the $\mathcal{E}$ under the cathode on the wavelength is shown in Figure 3.37. The electron transition with energy 0.77±0.05 eV causes the observed decrease of the electric field under the cathode. It means that there is an increase in the negative total space charge caused by electron transitions from the valence band to the deep level $E_t = E_v + (0.77 \pm 0.05)$ eV.

The next optically induced electron transition is at 1.10 ± 0.05 eV when the electric field under the cathode starts to increase. It corresponds to a build-up of the positive space charge. Therefore the electron transition occurs from the deep level $E_t = E_c - (1.10 \pm 0.05)$ eV to the conduction band.

Sample #7-CdZnTeSe

The dependence of the selected $\mathcal{E}(x)$ profiles on the NIR illumination from the monochromator is shown in Figure 3.38. The $\mathcal{E}(x)$ profile without illumination linearly increases from the anode to the cathode, which indicates a positive space
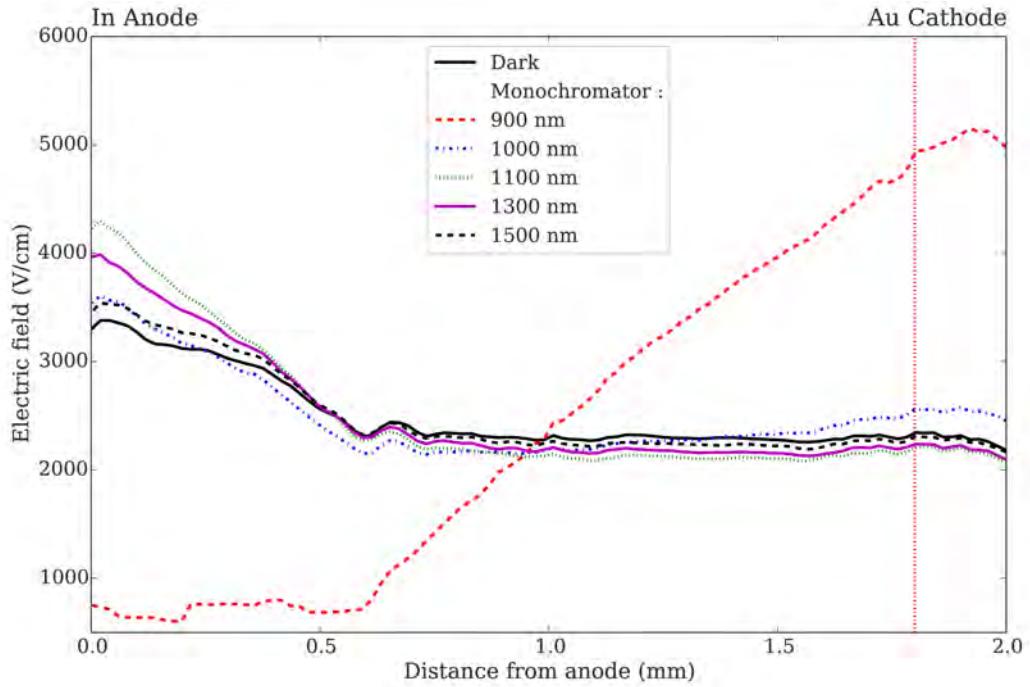
Figure 3.36: The profiles of the electric field in the sample #3-CZT with and without illumination from the source of the monochromatic light. The applied voltage was 500 V on the In contact, and the temperature was 300 K. The red dotted vertical line at $x = 1.8$ mm indicates the position where the electric field was extracted and plotted showing the dependence on illumination wavelength in Figure 3.37.
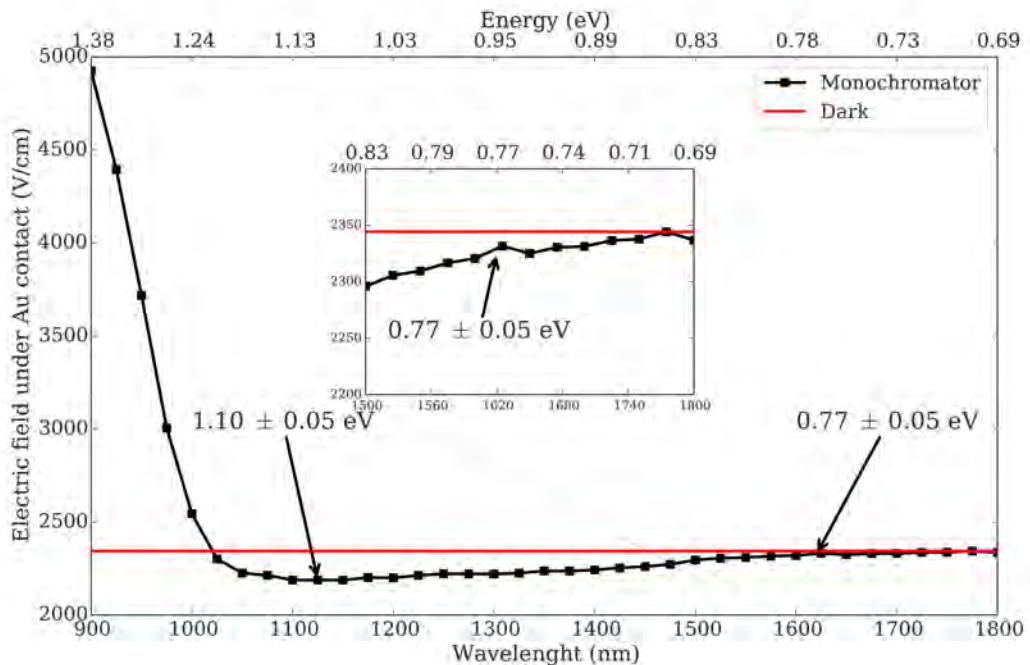
Figure 3.37: The electric field dependence on illumination wavelength for sample #3-CZT. The inset graph shows the area in the range of $1500 - 1800$ nm. The arrows mark the change of the electric field under the cathode induced by optical transitions. The determined deep levels are 0.77 and 1.10 eV with a 0.05 eV error.

67

charge in the sample volume. The below band-gap NIR light from the monochromator penetrates through the whole sample volume.
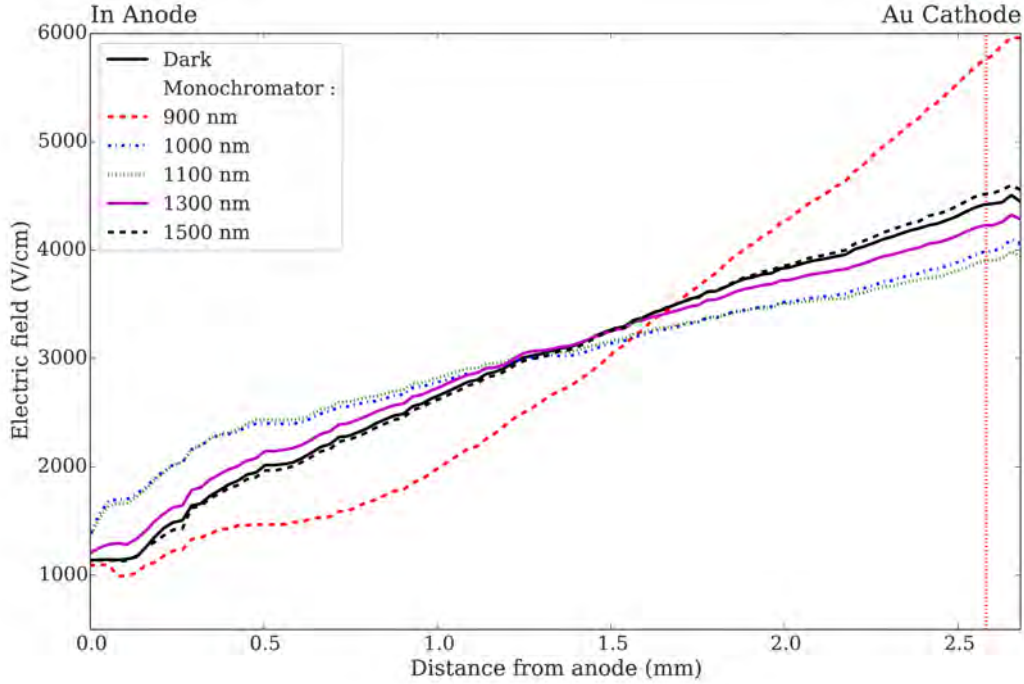
Figure 3.38: The sample #7-CZTS profiles of the electric field with and without illumination from the source of the monochromatic light at 800 V on the In contact, and $T = 300$ K. The red dotted vertical line shows the position where the electric field was evaluated and plotted showing the dependence on illumination wavelength in Figure 3.39.

The dependence of the electric field under the cathode (0.1 mm from cathode) is shown in Figure 3.39 for a step of 25 nm of the wavelength of the illuminating light. The illumination at 1725 nm (0.73 eV) causes a slight increase of the electric field under the cathode due to transitions of electrons from the deep level to the conduction band $E_c - 0.73$ eV. This transition causes an increase in the positive space charge, which leads to an increase of the electric field under the cathode. Other optically induced electron transitions affecting the electric field start at 1500 nm (0.83 eV). The decrease of the electric field under the cathode indicates a decrease in the positive space charge in the sample. It corresponds to transitions of electrons from the valence band to the deep level at $E_v + 0.83$ eV. The electric field under the cathode starts to increase at 1050 nm (1.18 eV) due to electron transitions from the deep level at $E_c - 1.18$ eV to the conduction band. This transfer forms a positive space charge in the sample.

In conclusion, we observed a 80 meV shift of the deep level $E_c - 1.10$ eV in CZT compared with $E_c - 1.18$ eV in CZTS. This level causes build-up of positive space charge due to the strong optically induced electron transitions from the deep level to the conduction band. The deep level $E_v + 0.77$ eV in CZT is also shifted to $E_v + 0.83$ eV. In addition, the CZTS sample has another deep level at $E_c - 0.73$ eV.

68
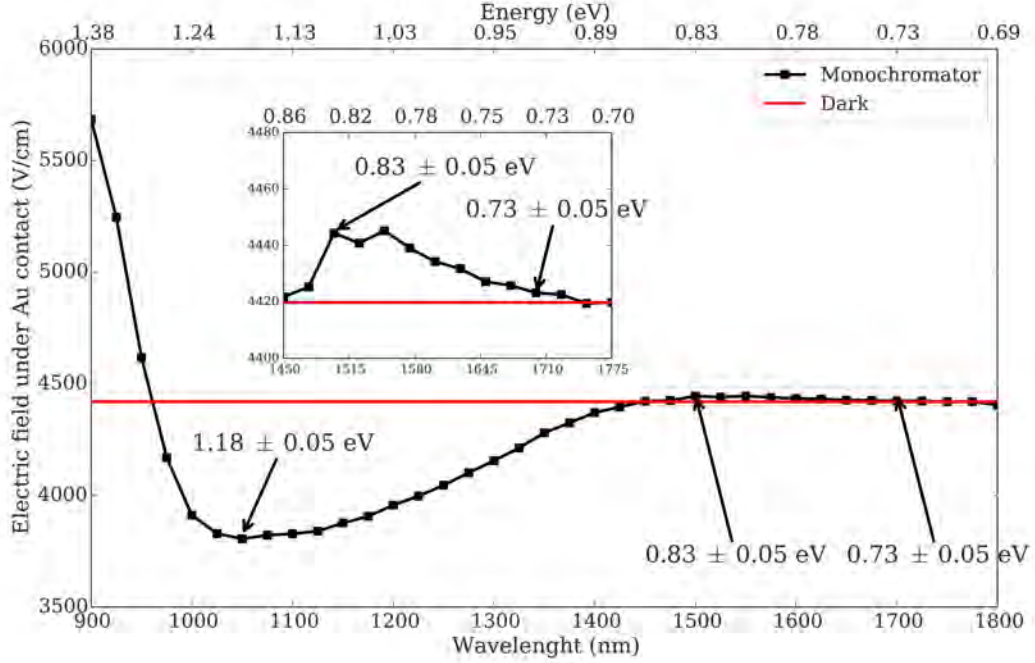
Figure 3.39: The electric field dependence on illumination wavelength for sample #7-CZTS. The inset graph shows the area in the range of $1450-1775$ nm. The arrows mark the change of the electric field under the cathode induced by the optical transition. The determined deep levels are 0.73, 0.83 and 1.18 eV with a 0.05 eV error.

3.3.4 Influence of additional light at 940 nm on the electric field

The set-up shown in Figure 2.1 was used to measure the $\mathcal{E}(x)$ profiles in the samples #3-CZT, #4-CZT and #7-CZTS under steady illumination by LED 940 nm. We used this LED due to the fact that the influence of the illumination at this wavelength on space charge is comparable with X-ray influence on occupation of deep levels [118]. This allows to easily simulate similar conditions of samples as under the irradiation with X-rays.

The selected $\mathcal{E}(x)$ profiles of sample #3-CZT are presented in Figure 3.40. This graph is supplemented by the $\mathcal{E}(x)$ profile without illumination at 300 K (grey dashed line). The $\mathcal{E}(x)$ profiles of sample #4 and #7 are shown in Figure 3.41 and Figure 3.42, respectively. The samples #3 and #4 were illuminated with the same photon flux 5×10^{15} cm^{-2}s^{-1}. The photon flux 1×10^{15} cm^{-2}s^{-1} was used to illuminate the sample #7-CZTS.

The light penetrates deep into the material because the absorption constant at wavelength 940 nm is lower than 10^3 cm^{-1}. Due to transitions between the shallow levels and the valence and conduction bands this light generates electrons and holes which then drift to the electrodes and can be trapped at deep levels. The concentrations of generated electrons and holes can differ [103], but the capture of holes prevails due to their low mobility. The positive space charge is formed due to prevailing optical transitions from deep levels to the conduction band and/or higher trapping of photo-generated holes when compared to electrons.

In the case of CZT samples #3 and #4, the negative space charge is present
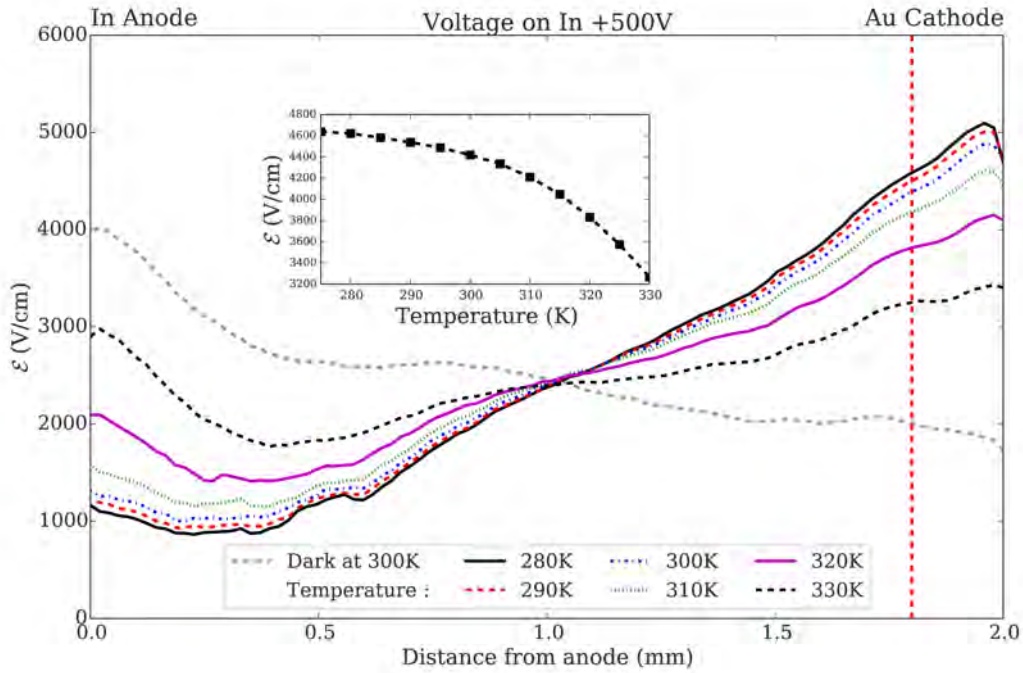
Figure 3.40: Profiles of the electric field in the sample #3-CZT at 500 V on In contact under illumination with LED at 940 nm as a function of temperature. The electric field profile without illumination at 300 K is added as a dashed gray curve. Vertical dashed red line shows the position where the data are taken for the insert graph.
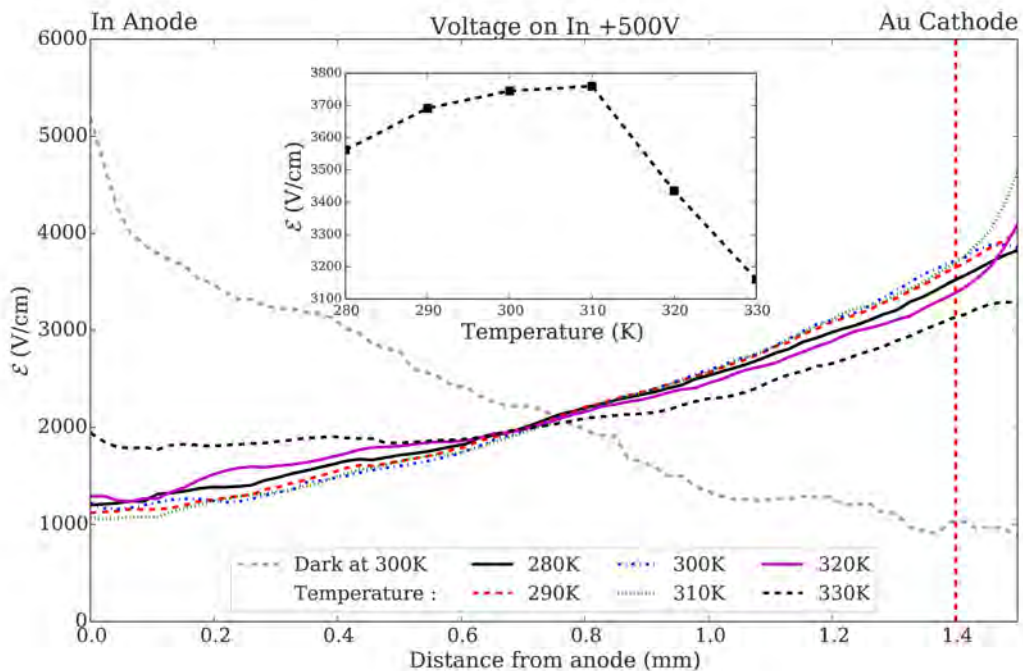
Figure 3.41: Profiles of the electric field in the sample #4-CZT at 500 V on In contact under illumination with LED at 940 nm as a function of temperature. The electric field profile without illumination at 300 K is added as dashed gray curve. Vertical dashed red line shows the position where the data are taken for the insert graph.

70

without illumination (section 3.3.1). The photo-generated charge gradually compensates the negative space charge induced by the hole depletion and causes an increase of the inner electric field under the cathode. All profiles are almost linear, and there is no dead layer under the studied experimental conditions. All the electric field measurements were performed with a bias voltage of 500 V. The polarization of the sample #3 decreases with increasing temperature. From the inserted graph in Figure 3.41, it is evident that the polarization of the sample #4-CZT has maximum around 310 K and for higher temperatures the polarization decreases with increasing temperature.
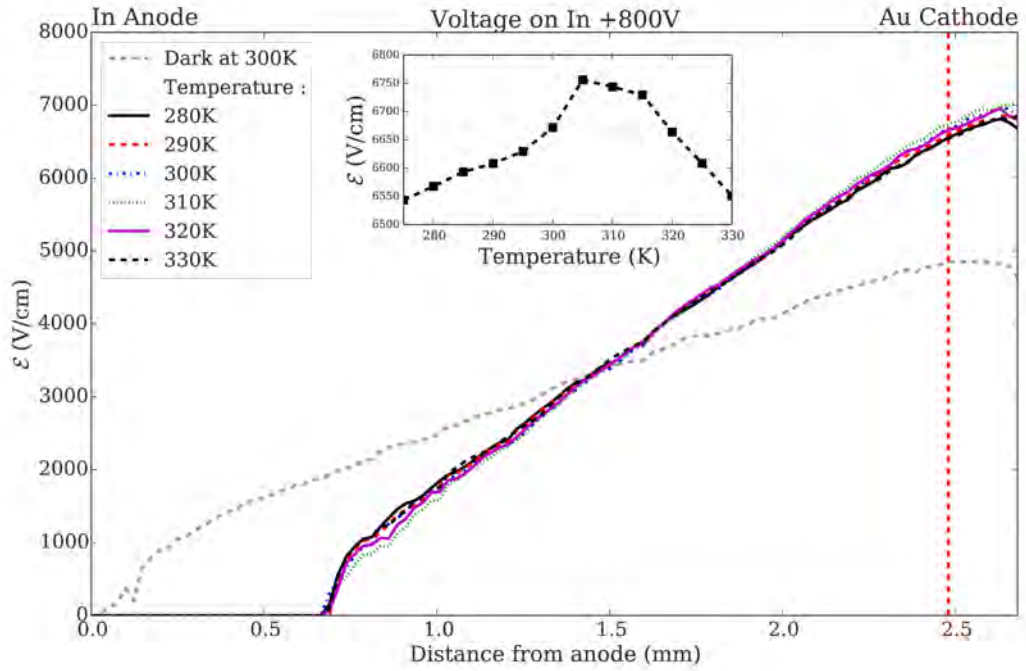
Figure 3.42: Profiles of the electric field in the sample #7-CZTS at 800 V on In contact under illumination with LED at 940 nm as a function of temperature. The electric field profile without illumination at 300 K is added as dashed gray profile. Vertical dashed red line shows the position where the data are taken for the insert graph.

The positive space charge is already formed in the CZTS sample #7 without illumination. The illumination induces increase of the positive space charge in the same way as in the sample CZT #3. The polarization creates a dead layer below the anode (Figure 3.42), where the electric field is close to 0. The temperature dependence is not as strong as the temperature dependence of samples #3 and #4.

3.3.5 Evolution of the inner electric field after switching off the additional light at 940 nm

The $\mathcal{E}(x, t, T)$ evolutions after switching off the additional light at 940 nm were measured in order to determine the deep levels responsible for the optically induced positive space charge which affects the sample similarly as a high flux of X-ray photons (see section about Infrared spectral scanning 3.3.3 and Influence of a additional light at 940 nm 3.3.4). The measurements and results are split into three paragraphs describing the samples separately.

Sample #3-CdZnTe

The selected $\mathcal{E}(x,t)$ profiles are depicted in Figure 3.43. In the beginning, the positive space charge is present in the sample due to the illumination. After switching off the illumination, the electric field returns into the steady-state without illumination, when the total space charge in the sample is slightly negative.
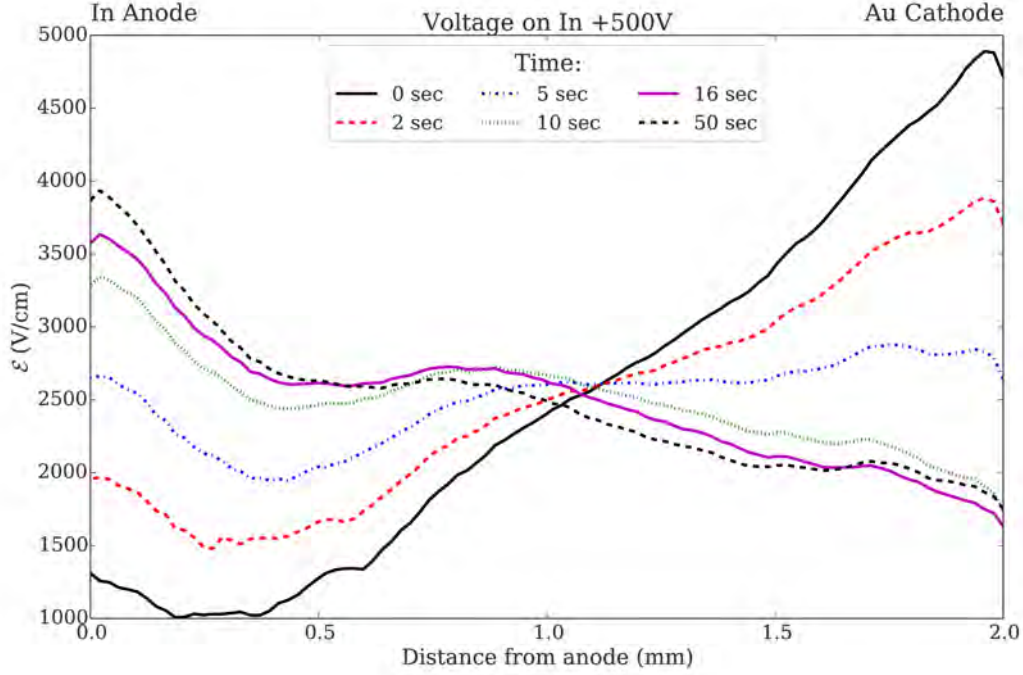
Figure 3.43: The selected profiles of the electric field in the sample #3-CZT after switching off the illumination at 940 nm. The bias is 500 V on In contact at 300 K.

Using the equation (3.4), the $Q(t)$ at 300 K was calculated and depicted in the Figure (3.44)(a). This evolution can be described by equation (3.5) as an exponential function. The determined time constant is 4.75 ± 0.03 s. The deep level energy responsible for the change of the total space charge and also the inner electric field was established by examining the temperature dependence of the time constant describing the exponential decay. Using equation (1.45) describing the Arrhenius diagram (Figure 3.44(b)), we evaluated the energy of the deep level $E_t = E_v + 0.86 \pm 0.01$ eV with capture cross-section for holes $\sigma_p = 2.0 \times 10^{-13}$ cm^2. The deep level was associated with the valence band due to the decrease of the positive space charge in time and with increasing T (Figure 3.40). This can happen only with a thermally activated transition of electrons from the valence band to the deep level.

The $\mathcal{E}(t)$ evolution under the cathode exhibits an oscillatory character (Figure 3.45(a)). It can be described as a critically damped oscillation (see equation (3.6)) because the total space demonstrates an exponential decay with one time constant. It means that only one deep level can be used to evaluate the data.

The $\tau(T)$ leads to the deep level $E_t = E_v + 0.87 \pm 0.01$ eV with capture cross-section for holes $\sigma_p = 2.0 \times 10^{-13}$ cm^2.

Both types of analysis of temperature and time evolutions (application of bias: section 3.3.2; switching off the LED 940 nm: section 3.3.5) give the same result

72
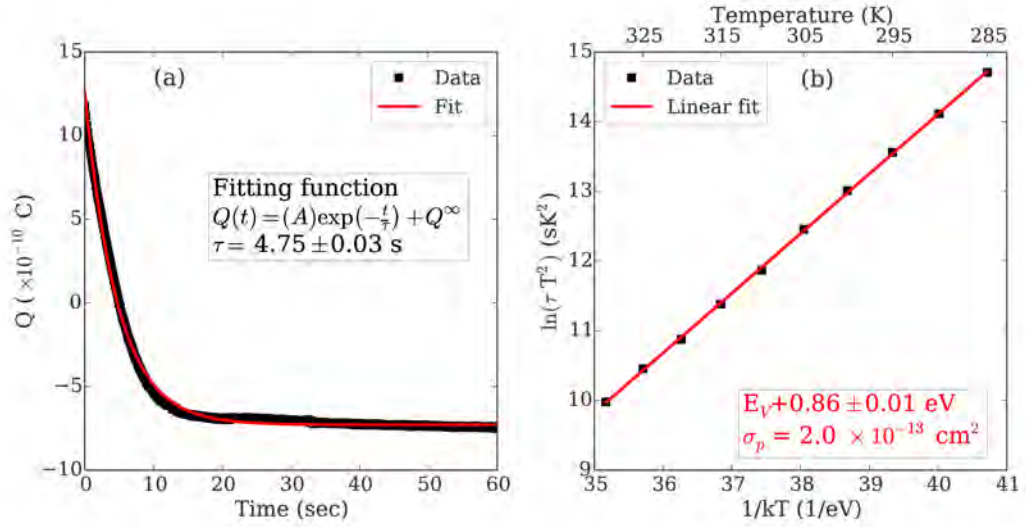
Figure 3.44: Time evolution of total space charge in the sample #3-CZT after switching off the additional light at 940 nm is shown in graph (a) at 500 V and $T = 300$ K. The graph (b) shows the Arrhenius diagram.
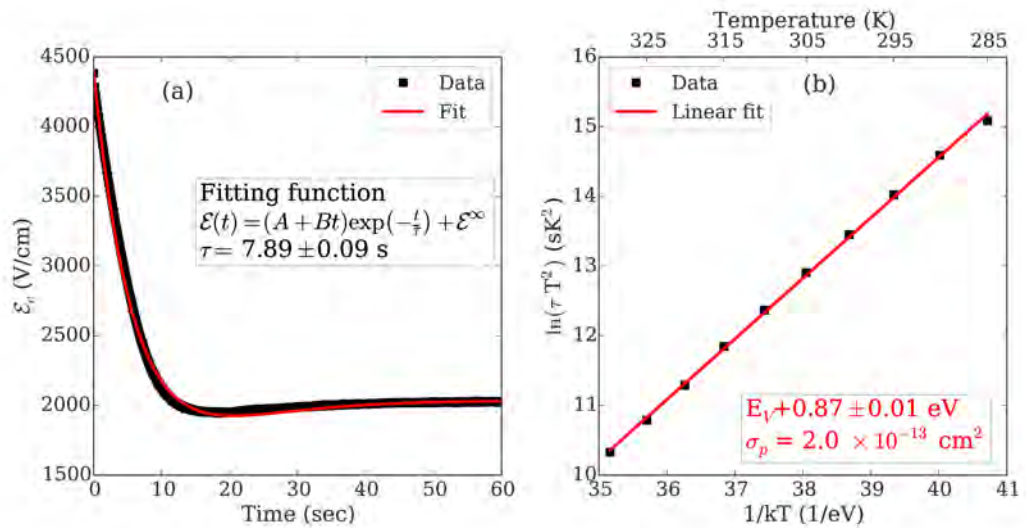
Figure 3.45: The sample #3-CZT time evolution of electric field under the cathode after switching off the additional light at 940 nm is shown in graph (a) at 500 V and $T = 300$ K. The graph (b) shows the Arrhenius diagram.

with one main deep level with activation energy $E_t = E_v + 0.86$ and capture cross-section $\sigma_p = 2.0 \times 10^{-13}$ cm^2.

Sample #4-CdZnTe

The set-up 2.2(b) was used for measuring the $\mathcal{E}(t)$ evolution with high time resolution.
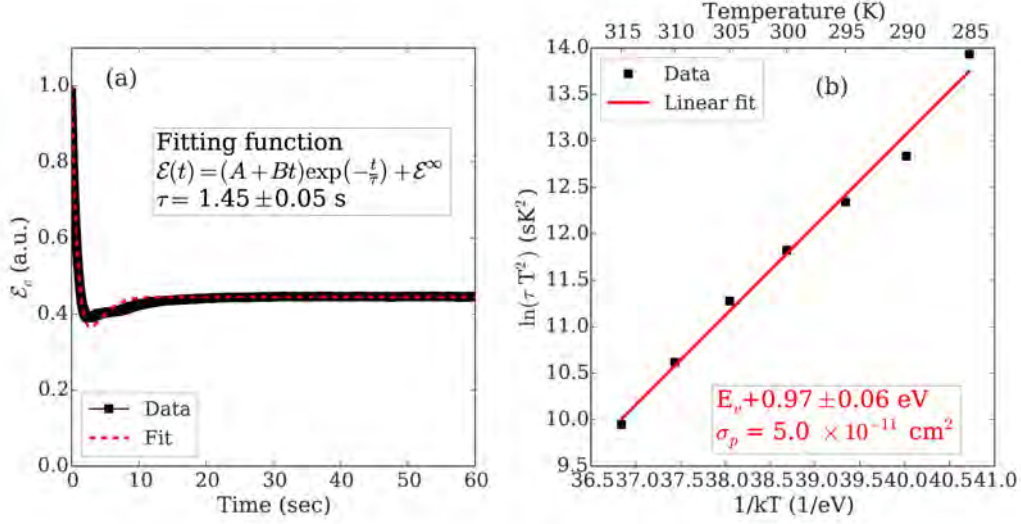
Figure 3.46: The sample #4-CZT time evolution of the electric field under the cathode after switching off the additional light LED 940 nm at 300 K.

The $\mathcal{E}(t)$ evolution after switching off the LED 940 nm at 300 K is shown in Figure 3.46. The $\mathcal{E}$ under the cathode returns to its original state as without the illumination after switching off the illumination. This evolution exhibits the critically damped oscillation character, which is the same as for CZT sample #3. Also the steady-state profiles of $\mathcal{E}(x)$ are similar(Figures 3.40 and 3.41). For those reasons, the equation (3.6) was used for fitting the dependencies. The fit leads to the time constant of $\tau = 1.45 \pm 0.05$ s. The time constant depends on temperature measured between 285 K and 315 K (see Figure 3.46). We determined activation energy 0.97 eV using equation (1.45) and associated it to a transition of electrons from the valence band, because the positive space charge decreases with increasing temperature. The evaluated capture cross-section for holes is $\sigma_p = 5.0 \times 10^{-11}$ cm^2.

Sample #7-CdZnTeSe

In sample #7 there is a positive space charge present without illumination (Figure 3.26). The illumination by 940-nm light causes its increase. The electric field returns to dark conditions (steady state) after switching off the 940-nm LED. It means that the positive space charge generated by illumination is reduced either due to thermally activated electron transitions from the valence band to the deep level or due to an electron capture from the conduction band to the deep level (not thermally activated).
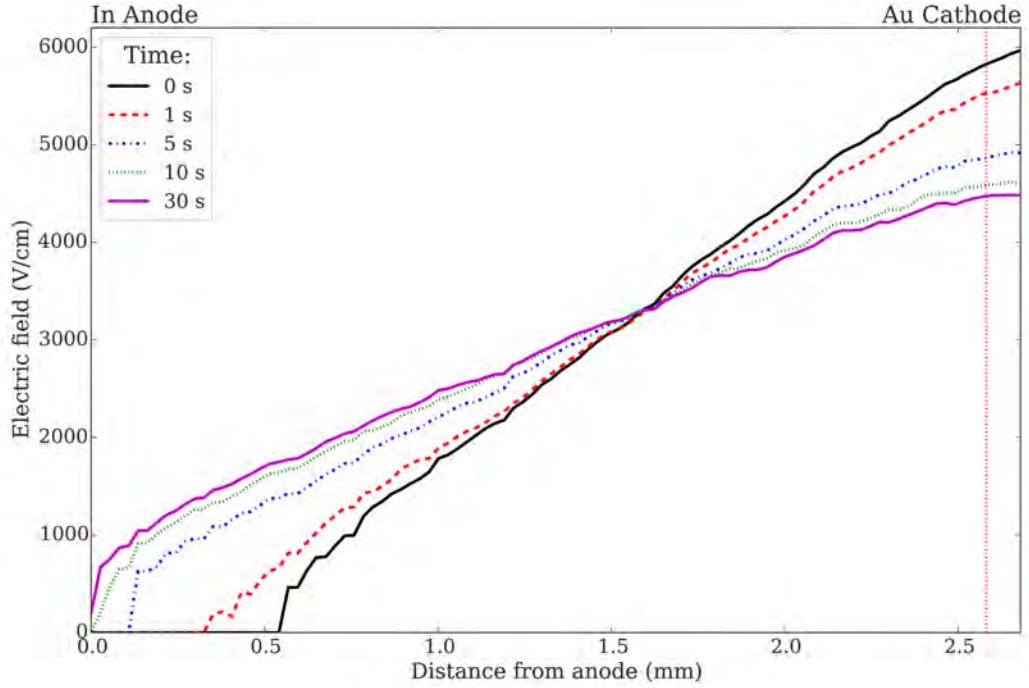
Figure 3.47: Selected electric field profiles of the sample #7-CZTS after switching off the LED at 940 nm at 800 V on In contact and $T = 300$ K.

The selected $\mathcal{E}(x,t)$ profiles at 0, 1, 5, 10 and 30 seconds after switching off the LED operating at 940 nm are shown in Figure 3.47. The $\mathcal{E}(x)$ profile recording immediately after switching off the illumination indicates presence of a dead layer under the In anode.

The corresponding $\mathcal{E}(t)$ evolution under the cathode is depicted in Figure 3.48(a), and the computed $Q(t)$ calculated by equation (3.4) is plotted in Figure 3.49(a). Both time dependencies exhibit a single exponential decay.

We measured also the temperature dependence of $\mathcal{E}$ profiles and their time evolution at temperatures $T = (280\,\text{K} - 330\,\text{K})$, evaluated $\tau(T)$ and calculated the activation energy (0.85 ± 0.02) eV and capture cross-section $\sigma_p = 1 \times 10^{-13}$ cm^2 using Arrhenius plot (Figure 3.48(b)). The same analysis applied to the total space charge Q (Figure 3.49(b)) resulted in practically the same values of $E_t = (0.85 \pm 0.02)$ eV with a capture cross-section of $\sigma_p = 2 \times 10^{-13}$ cm^2.

We conclude that the main deep level in the CZTS sample #7 responsible for the $\mathcal{E}$ evolution after switching off the illumination at 940 nm is at $E_v + 0.83$ eV. The incident light at 940 nm caused the transitions between shallow levels and the valence and conduction band, which generates electrons and holes which then can be trapped at deep levels. The capture of holes prevails and the positive space charge is formed. After switching off the illumination at 940 nm, the electron returns to this deep level from the valence band. It causes a decrease in the positive space charge. We also conclude that both the energy and capture cross-section of this deep level are the same as those evaluated after bias application (section 3.3.2).

In summary, one main deep level is responsible for $\mathcal{E}(t)$ evolution after switching off the illumination in all samples due to the mono-exponential decay of the total space charge. In case of the CZTS sample the $\mathcal{E}(t)$ evolution under the

75
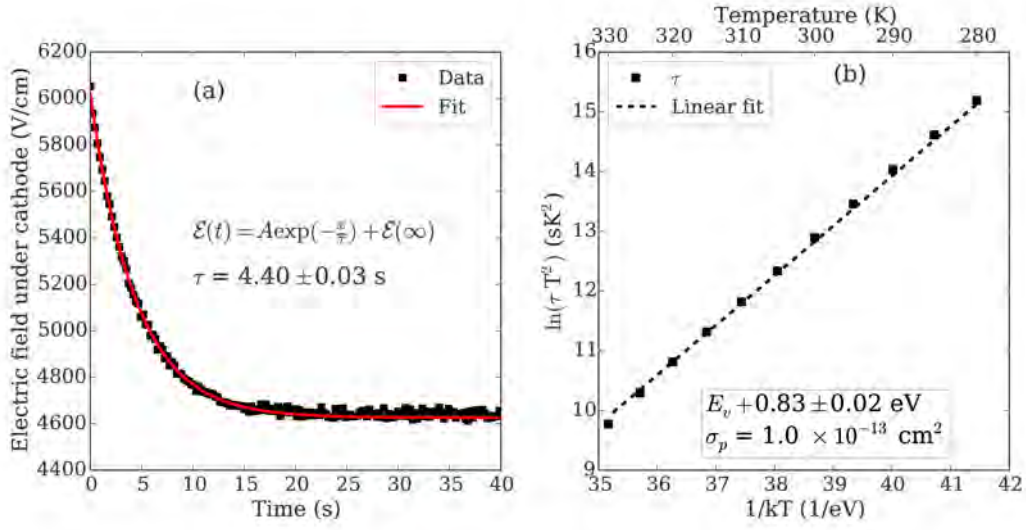
Figure 3.48: The time evolution of electric field under the cathode in sample #7 CZTS is plotted in graph (a). This graph shows a mono-exponential decay of the electric field (black square) with the mono-exponential fit (red line). The Arrhenius diagram is plotted in the graph (b). The evaluated deep level is $E_v + 0.83 \pm 0.02$ eV with hole capture cross-section of $\sigma_p = 1.0 \times 10^{-13}$ cm^2.
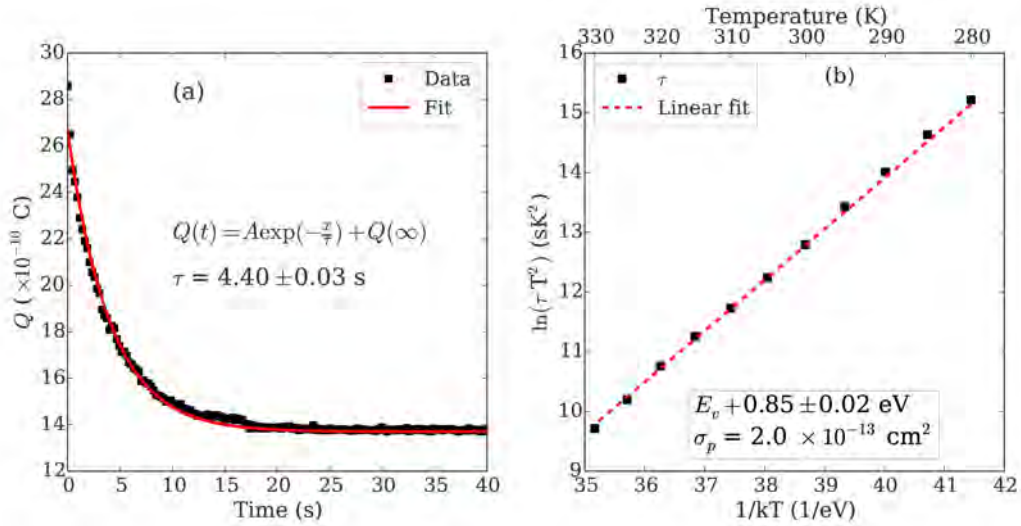
Figure 3.49: The computed space charge in the sample #7-CZTS is plotted in the graph (a) as black squares with the single exponential fit (red line). The Arrhenius diagram is plotted in the graph (b). The observed deep level energy is $E_v + 0.85 \pm 0.02$ eV with hole capture cross-section of $\sigma_p = 2.0 \times 10^{-13}$ cm^2.

cathode has also mono-exponential character (Figure 3.48(a)) as the total space charge (Figure 3.49(a)). On the other hand, the $Q(t)$ evolution (Figure 3.44(a)) of sample #3-CZT leads to the critically damped oscillation character in the $\mathcal{E}(t)$ evolution of under the cathode (Figure 3.45(a)).

3.3.6 Summary of deep levels and comparison between samples

The schemes of the observed energy levels using the infrared spectral scanning method (section 3.3.3) and temperature and temporal measurements of evolution the inner electric field (see sections 3.3.2 and 3.3.5) are presented in Figures 3.50, 3.51 and 3.52 for samples #3, #4 and #7, respectively. The scheme 3.51 is supplemented with our previous results about deep levels in the sample #4, which were determined using the infrared spectral scanning method [118].
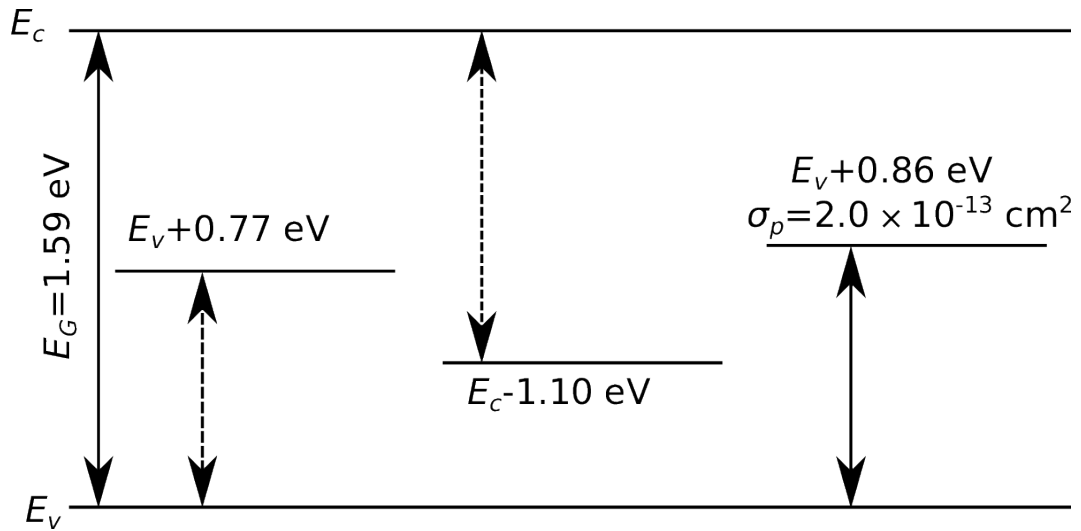
Figure 3.50: The scheme of the observed energy levels in sample #3-CZT. The full line represents energy level found by the temperature measurements and dashed lines represent energies found by the infrared spectral scanning method.

Deep levels active in optically induced polarization

The deep level $E_c - 1.10$ eV was evaluated as the main level that causes the strong optically induced polarization in the CZT samples #3 and #4 by using the spectral infrared scanning (more information in the section 3.3.3 and the article [118]). In the CZTS sample #7 this transition is shifted to $E_c - 1.18$ eV. We assume that these two levels have the same origin. Kim [119] assigned this deep level to dislocations induced by Te inclusions/precipitates. Castaldini [39] attributed the energy level at 1.1 eV below the conduction level to a positively charged tellurium vacancy. Du et al. [120] calculated the energy of a deep donor state of Te antisite corresponding to the +2/0 charge state 0.35 eV above the valence band. The calculated levels of the vacancy V_{Te} are approximately 0.9 eV and 1.1 eV. Transitions ascribed to both the Te antisite and Te vacancy are within the experimental error in the range of energies observed for the samples. Based on the published experimental data and theoretical models it is therefore probable,

that the observed energy levels are connected to Te atoms that migrated to Cd position (Te antisite) or to the surface (Te vacancy).

It should be noted that transitions in this energy range are in the literature often ascribed also to dislocations [69] and deep impurities. An extended literature overview of this topic can be found in ref [52].
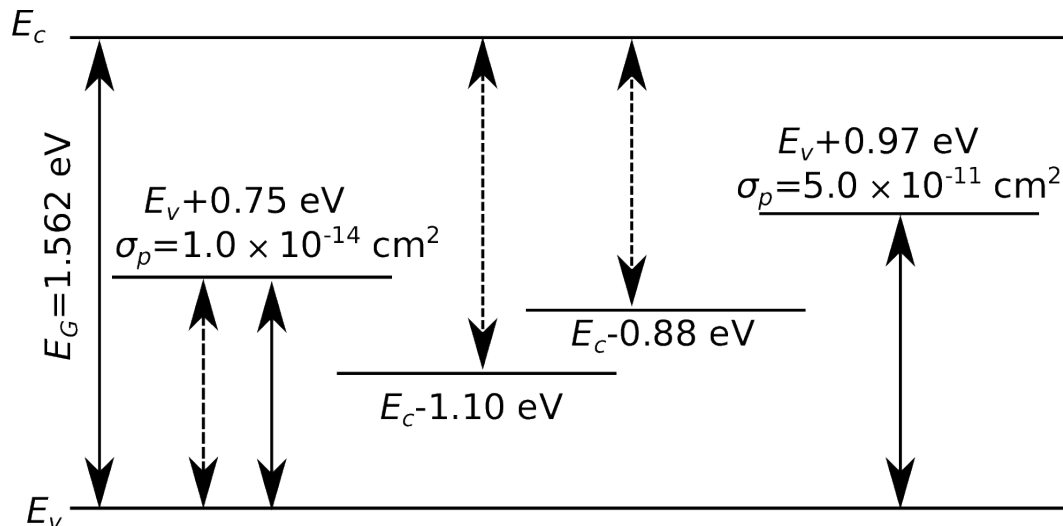
Figure 3.51: The scheme of the observed energy levels in sample #4-CZT. The full line represents energy level found by the temperature measurements and dashed lines represent energies found by the infrared spectral scanning method from our previous study [118].
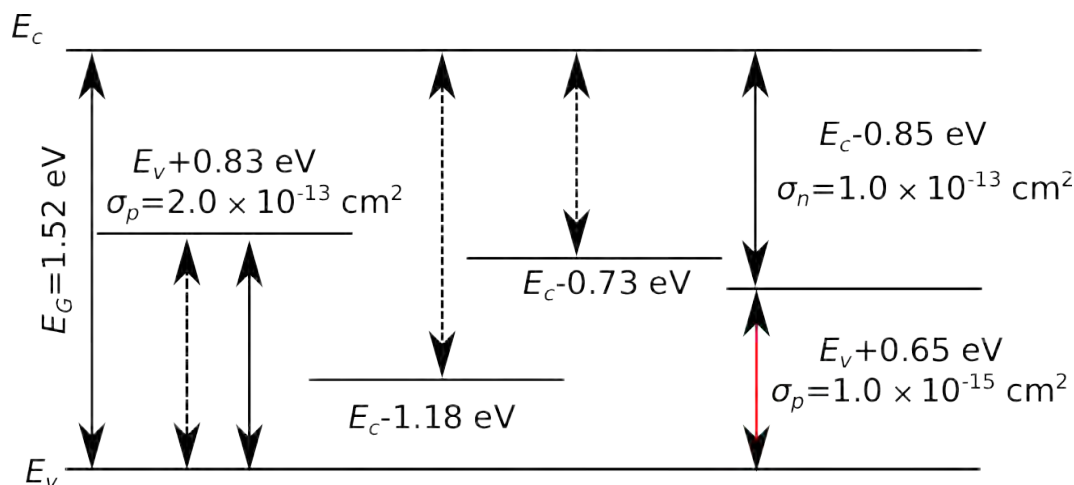
Figure 3.52: The scheme of the observed energy levels in sample #7-CZTS. The full line represents the energy level found by the temperature measurements and dashed lines represent energies found by the infrared spectral scanning method. The solid red lines represent activation energy found by measurement of temperature and temporal dependence of the electric current.

The deep level $E_v+0.83$ eV in CZTS has probably the same origin as the level $E_v + 0.77$ eV in CZT sample 3 and the deep level $E_v + 0.75$ eV in CZT sample 4. This level was assigned to the second ionized state of cadmium vacancy by Castaldini [39]. It is responsible for both a thermally and an optically induced

decrease of positive space charge after application of the bias and infrared light. The observed energy shift of the level towards the conduction band in CZTS compared to CZT is in agreement with theoretical predictions of Varley [121]. They used first-principles calculations based on screened hybrid functionals and found that energy levels of cadmium vacancy shifted towards the conduction band when Se replaces Te in the lattice. The observed energy shift, therefore, also strongly indicates that the studied defect is related to Cd vacancies.

The deep level $E_c - 0.85$ eV observed from temporal and temperature analysis is responsible for setting the electric field after the application of the bias in CZTS sample #7. Also, it is responsible for the positive space charge at steady state. For the CZT sample #3, the deep level $E_v + 0.86$ eV is responsible for the evolution of the electric field after the application of bias and switching off the LED 940 nm. The negative space charge is built-up in this level.

In the case of the CZT sample #4 the deep level $E_v + 0.75$ eV is the main level influencing the evolution of the electric field after application of bias. On the other hand, the temporal and temperature evolution of the electric field after switching off the additional light at 940 nm is affected by the deep level $E_v + 0.97$ eV.

Comparison of deep levels in CZT and CZTS

It is apparent that the activation energy of electrons from deep level $E_c - 1.18$ eV to the conduction band is higher in CZTS sample by 80 meV when compared to CZT samples ($E_c - 1.10$ eV). The activation energy of electrons from the valence band to the deep level $E_v + 0.83$ is also higher by approximately 50 meV in the case of CZTS sample in comparison with CZT samples; $E_v + 0.77$ eV in the sample #3 and $E_v + 0.75$ eV for the sample #4. At the same time, the energy band of CZTS is smaller by 70 meV compared to CZT sample #3 (Table 3.1). It means that the observed shifts of energies in CZTS, when compared to CZT, cannot be simply explained by the change of the band-gap after the introduction of Se in the lattice. While the change of energies of the principal deep levels may seem relatively small, it can significantly influence occupations of these levels if they are close to the Fermi energy, and in this way affect the stability of the Fermi level along the ingot as well as trapping and recombination of free carriers.

3.4 Simulation of the temperature and temporal electric field evolution

The time and temperature evolutions of the electric fields of samples #3-CZT and #7-CZTS (typical representative samples for CZT and CZTS) after the application of the voltage bias were compared with a numerical simulation based on the solution of the drift-diffusion and Poisson equations, including the Shockley-Read-Hall model [122]. The analysis related to sample #7 includes also simulation of the electric current after switching on the bias.

The results were published in articles [117, 123].

Table 3.6: Parameters used in the simulations

Bias on In electrode (V)	500
Sample properties:	
Thickness (mm)	2.00
Bandgap energy (eV)	1.59
Fermi level energy (eV)	$E_F = E_v + 0.82$
Schottky barrier height (eV)	$\phi_{Au} = 0.87/\phi_{In} = 0.79$

Table 3.7: Parameters of the deep level used in the simulations

Deep levels:	E_1
Energy (eV)	$E_v + 0.87$
Concentration (cm^{-3})	2.0×10^{12}
σ_n (cm^2)	1.0×10^{-25}
σ_p (cm^2)	3.7×10^{-14}

Sample #3-CdZnTe

To confirm our conclusions that the electric field oscillations can be explained by change of occupation of one deep level, we performed several numeric simulations in order to fit experimental data.

The general conditions used for the simulation are listed in the Table 3.6 and the parameters of deep level are summarized in the Table 3.7.

We used experimentally determined band-gap energy from ellipsometry measurement, the energy of the deep level $E_v + 0.87$ and capture cross-section from Pockels effect measurements (Sections 3.1.1, 3.3.2 and 3.3.5). These measurements have shown, that this level is a hole trap. Therefore we assumed that it does not communicate with the conduction band and set the σ_n to 0, which was for numerical purposes represented by a value 10^{-25} cm^2. During the simulation, we performed a careful mutual tuning of realistic values of parameters E_F, N_t and σ_p and of the band bending at Au/CZT, In/CZT interfaces. This tuning of parameters resulted in a value of $\sigma_p = 3.7 \times 10^{-14}$ cm^2, which is approximately one order of magnitude smaller than the experimental value. The used Fermi level position $E_F = E_v + 0.82$ is 100 meV closer to the energy mid-gap than the experimental value. Finally, we obtained fairly good agreement between experimental and simulated data with the undershoot of the electric field below the cathode (Figure 3.53(a)).

A comparison of the time evolution of the electric field in the vicinity of the cathode $\mathcal{E}_c$ and the anode $\mathcal{E}_a$ at 300 K between the experiment and the simulation is shown in Figure 3.53(a). We compare the experimental Q and simulated Q^{sim} time evolutions of the total space charge(Figure 3.53(b)).

We explain the undershoot in the electric field evolution close to the cathode by a process of space charge formation, which is initially distributed homogeneously within the detector and redistributed consecutively to the region close to the anode. The space charge damping close to the cathode is induced by the lowered electric field in this region, which results in hole density enhancement, trapping on the hole trap and the reduction of previously formed negative space
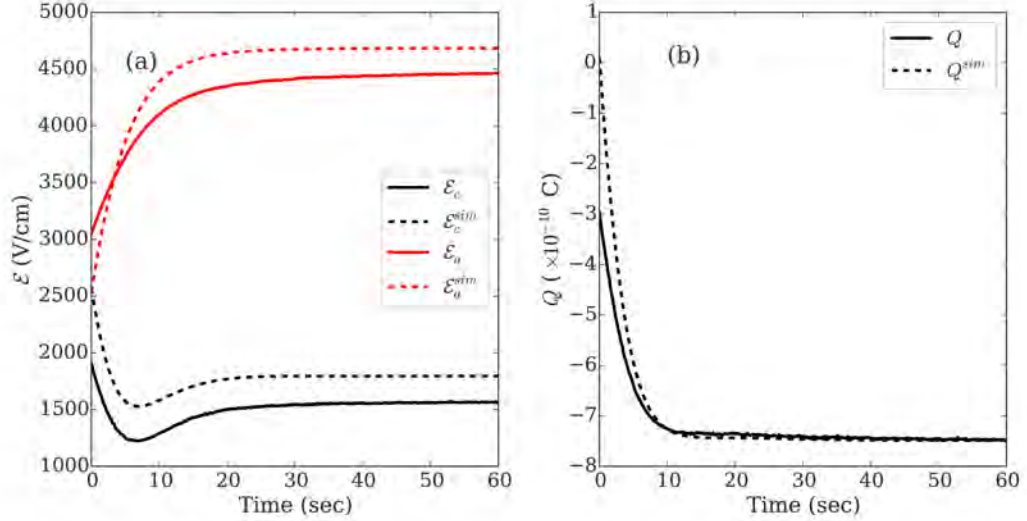
Figure 3.53: Comparison between experimental values of $\mathcal{E}_c$, $\mathcal{E}_a$ and Q (solid lines) and results obtained by a numeric simulation (dashed lines).

charge close to the cathode. The discussed processes are depicted in Figure 3.54.

In the used simulation, the shape of the electric field distribution strongly varies with a relatively small change of the band bending at the In/CZT interface and the deep level concentration N_t

The band bending at the In/CZT interface determines the total steady-state space charge and thus the slope of the electric field profile. The parameter -26 meV for the band bending at In/CZT is much lower than expected (≈ 1 eV) based on the work function difference model probably because of the presence of the surface dipoles due to a thin oxide layer between CZT and In [105].

The main factor affecting the oscillation of the electric field at the cathode $\mathcal{E}_c$ and thus the space charge is the deep level concentration N_t (Figure 3.55(a)). At low concentration up to 5×10^{11} cm^{-3}, there is no undershoot of the electric field, and it has a monotonous time evolution. The undershoot can be observed for higher values of N_t. Using the same set of simulation parameters, we calculated the time evolution of the total current density j (Figure 3.55(b)). It is apparent that undershoots and oscillations can be seen as well. This fact is in a good agreement with the model presented by Cola and Farella [82], that assumes the model with a direct correlation of the dark current with the electric field that oscillates below the cathode. The sample is an n-type; therefore, these oscillations influence the electric current of majority electrons emitted by the cathode.

Sample #7-CdZnTeSe

The experimental data (solid lines) and simulated data are depicted in Figure 3.56 (dashed lines). The general conditions used for the simulation are listed in Table 3.8. The parameters of the used deep levels are summarized in Table 3.9. We were able to fix many parameters from experimental data, and, in this way, we increased the reliability of the simulations. The Schottky barrier heights at the In/CZTS and Au/CZTS interfaces were set from the evaluation of the I-V characteristics (Figure 3.35). The band-gap energy was set from the results of

30 ms: almost neutral state, level occupied by holes, increase of the negative space charge

up to 7 s: homogeneous rapid increase of the negative space charge (hole de-trapping)

after 7 s: increase of the negative space charge continues and hole trapping close to the cathode begins
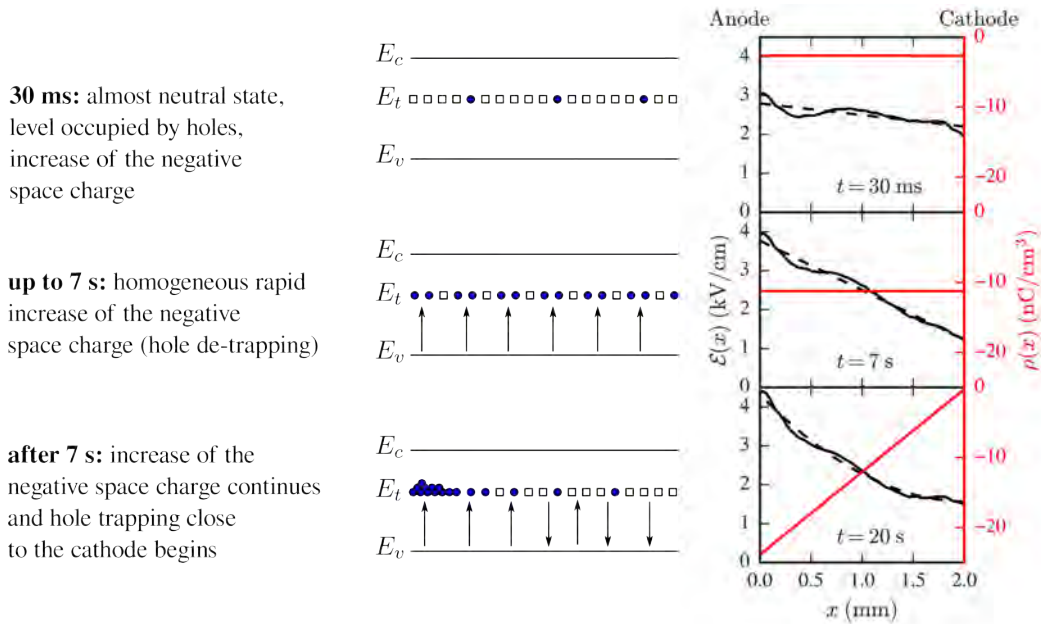
Figure 3.54: Scheme of hole trap occupation with corresponding electric field $\mathcal{E}(x)$ (solid black curves) and space charge density $\varrho(x)$ (red lines) distributions. Estimations of $\varrho(x)$ have been calculated using equation 3.3 from linear (30ms and 7 s) and parabolic (20 s) fits of $\mathcal{E}(x)$ (dashed cures).
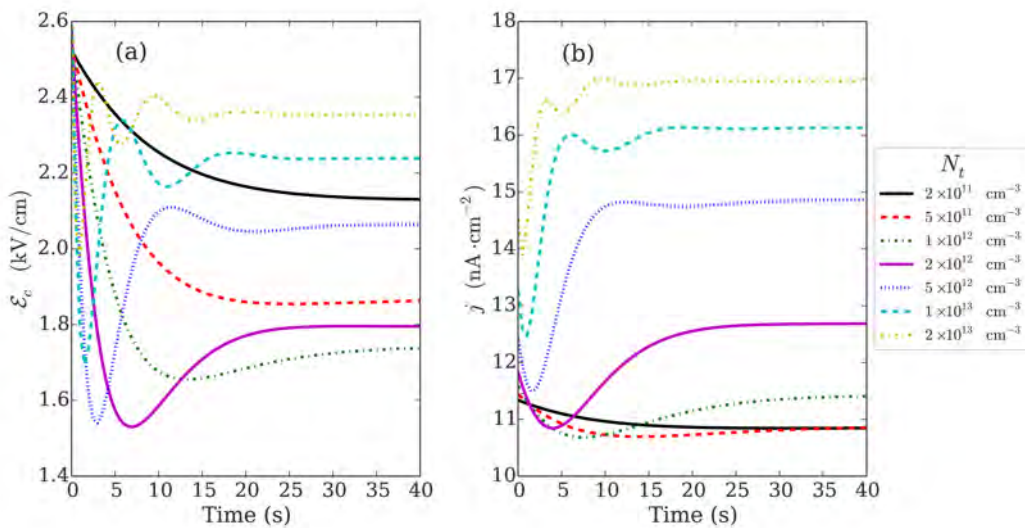
Figure 3.55: Simulation of $\mathcal{E}_c(x)$ and the current density ȷ. Dependence on the deep level concentration N_t. All other simulation paramenters are fixed to the values from Tables 3.7 and 3.6.

82

Table 3.8: General conditions used in the simulations of temporal and temperature evolutions of the electric field and current in the sample CZTS #7

Bias on In electrode (V)	800
Sample properties:	
Thickness (mm)	2.68
Bandgap energy (eV)	1.52
Fermi level energy (eV)	$E_F = E_c - 0.727$
Schottky barrier height (eV)	$\phi_{Au} = 0.96 / \phi_{In} = 0.90$

ellipsometry measurements (Figure 3.2). The Fermi level position was calculated according to the equation (3.1) $E_F = E_c - 0.727$. The energies of the deep levels were set based on results of the evaluation of temperature and time evolution of the electrical field by the Pockels effect. For simulation, we have chosen two deep levels, E_1 and E_2, which were observed by electrical and optical measurements (see sections 3.1.1, 3.3.2 and 3.3.5). The capture cross-sections of deep levels were used as fitting parameters. We applied the experimentally determined values of the electron capture cross-section of the level E_1 and the hole capture cross-section of the level E_2 as initial values for fitting. The resulting optimal values (Table 3.9) are $1-2$ orders of magnitude smaller. These sets of fitting parameters presented in Table 3.9 lead to a very good agreement between experiment and simulated data (Figure 3.56). According to simulation results, the level E_1 acts as a recombination center with a higher capture cross-section for electrons than for holes. The deep level E_2 is in the model a pure hole trap, and this fact is demonstrated by setting the capture cross-section for holes as 0 cm^2. For the numerical purpose of the calculation, it is represented by a minimal nonzero value of 10^{-25} cm^2.

The computed evolution of the total space charge Q and simulated evolution of total space charge Q^{sim} are depicted in Figure 3.57. The Q^{sim} exhibits the overshoot similar to the $Q(t)$ dependence evaluated from experiment. On the other hand the total space charge evolution for sample #3-CZT can be describe as a mono-decay exponential function (Figure 3.53). It confirms our prediction that the number of deep levels responsible for time evolution of electric field can be determined from the time behaviour of the total space charge.

The results of the simulation demonstrate that the electrical current is predominantly formed by the flow of injected free holes due to the band bending upwards at the interfaces. The Au/CZTS interface blocks electrons when positive bias is applied on the In contact. The In/CZTS interface injects the holes into the volume of the sample. The damped oscillatory character with undershoots of both the electric current and of the electric field under the cathode is caused by the change of occupancy of deep levels over time. The computed deep level's occupancies by electrons are depicted in Figure 3.58. The presented profiles and their evolution in time can be described by the following series of processes.

At first, holes are injected from the In anode within 0.1 sec after application of the bias and are captured on both deep levels. This effect causes a strong decrease in the occupation of both levels, especially at positions close to the anode (see the dashed lines showing the occupancy profiles after 0.13 sec in Figures 3.58(a) and 3.58(b)). The simplified scheme describing these processes is plotted in Figu-

Table 3.9: Parameters of the deep levels used in the simulations

Deep levels:	E_1	E_2
Energy (eV)	$E_c - 0.836$	$E_c - 0.697$
Concentration (cm^{-3})	2.8×10^{11}	5.4×10^{11}
σ_n (cm^2)	5.0×10^{-13}	1.0×10^{-25}
σ_p (cm^2)	7.5×10^{-16}	7.0×10^{-15}
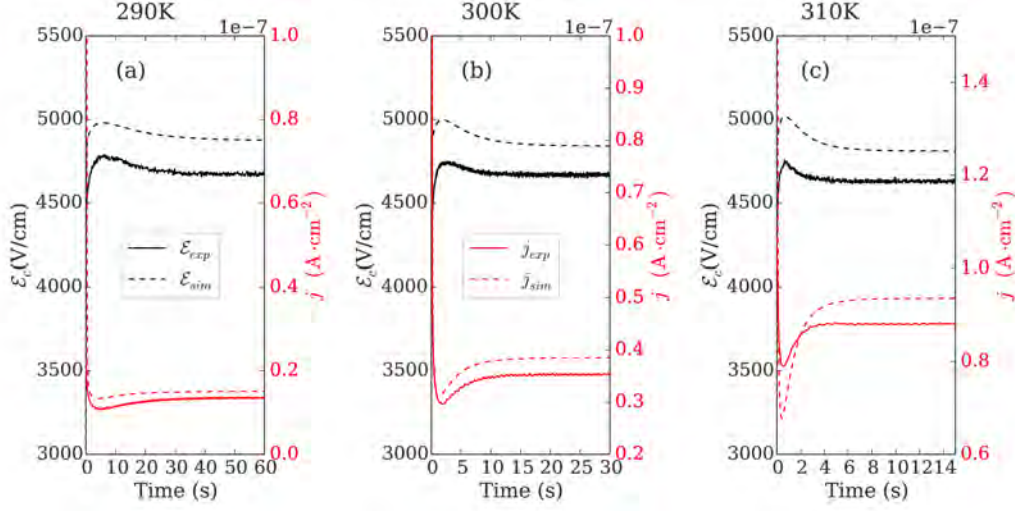
Figure 3.56: Time evolution of the electric field under the cathode (solid black line) and the electric current (solid red line) after switching on the bias at different temperatures. The numerical simulation of the electric field evolution under the cathode is represented by a black dashed line, and the current is represented by a red dashed line.
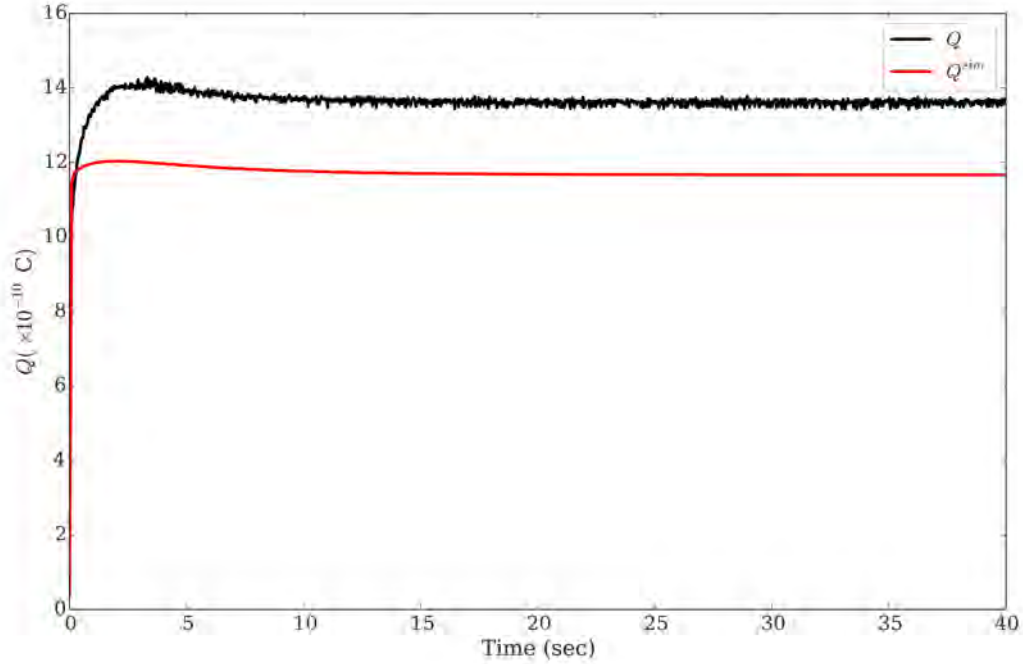
Figure 3.57: Time evolution of the total space charge Q (black solid line) and simulated total space charge Q^{sim} (red solid line).

84

re 3.59(a). It leads to an increase in the positive space charge in the sample. Due to the formed positive space charge, the electric field under the cathode increases. After that, the higher electric field depletes the holes from the volume near the cathode, which leads to a higher emission of captured holes from the deep level E_2 accompanied by an increase of its occupancy (see profiles after 1.9 sec and 4 sec in Figure 3.58(b) and schemes in Figure 3.59(b). This process causes the subsequent decrease of the positive space charge, which induces a decrease of the electric field below the cathode. The electrical current increases due to the higher amount of free holes.

Graph 3.60(a) shows that the deep level E_1 is monotonously discharged over time (black squares with dashed line), it is caused by electron transfers from the level. On the other hand, the integrated occupancy of the deep level E_2 exhibits an undershoot, which induces the overshoot in the electric field. The profiles of the free holes in the valence band are depicted in Figure 3.60(b).
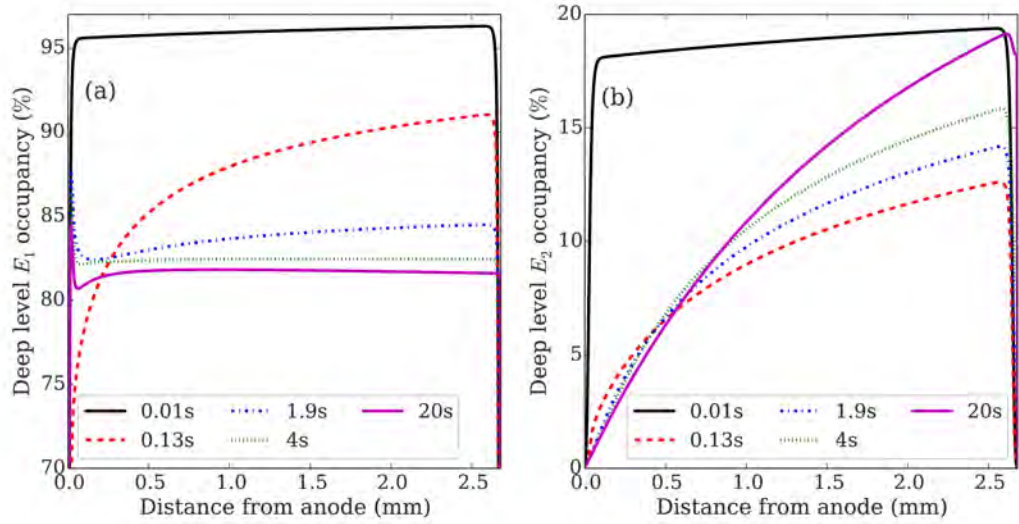
Figure 3.58: Graph (a) shows the deep level E_1 occupancy, The deep level E_2 occupancy is depicted in Graph (b).

In order to clarify the role of both deep levels E_1 and E_2 on detector performance, we performed a simulation of the electron mobility-lifetime product for two cases- in the first one, we included only the deep level E_1; in the second case, we included both deep levels. We observed that the mean average over the sample thickness (Figure 3.61) of the electron $\mu\tau^{E_1}$ product is 0.59×10^{-3} cm^{2}V^{-1}. The electron mean average $\mu\tau^{E_1+E_2}$ product for the case with both levels is 1.16×10^{-3} cm^{2}V^{-1}, which agrees with the experimentally determined value $\mu\tau_e^{exp} = 1.10 \times 10^{-3}$ cm^{2}V^{-1}. The experimental $\mu\tau^{exp}$ product was evaluated by a procedure involving a non-constant electric field [34].

Therefore, the electron $\mu\tau$ product is higher for the case with both levels due to the presence of the deep hole level E_2. This level communicates dominantly with the valence band and acts as a hole trap. It reduces the concentration of free holes and in this way also transitions of electrons from the recombination trap E_1 to the valence band. The occupancy of the level E_1 with electrons is increased, transitions of electrons from the conduction band to the level E_1 are decreased, and the mobility-lifetime product of electrons is increased if level E_2 is present.

85
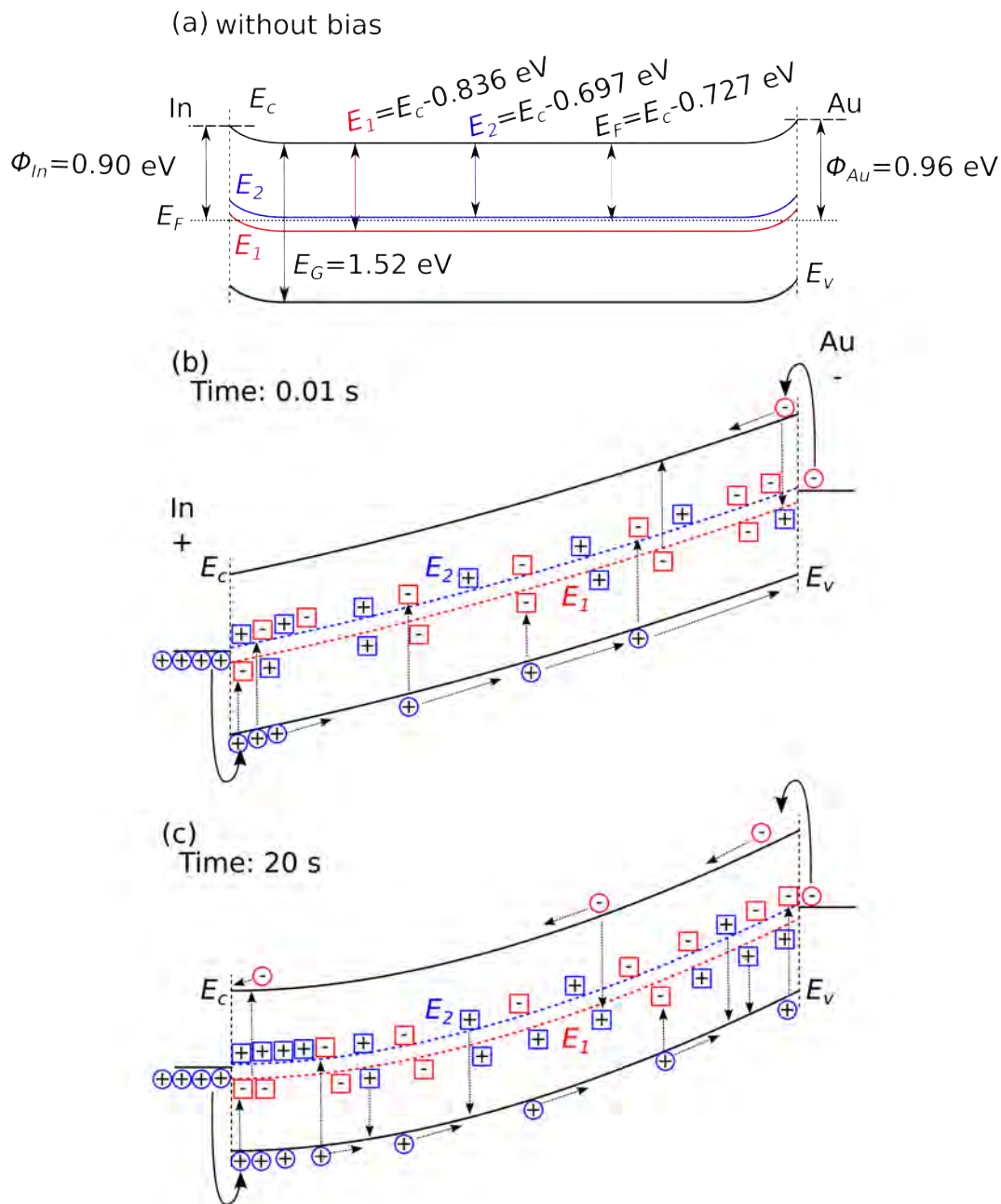
Figure 3.59: Scheme (a) shows the energy diagram of the In/CZTS/Au structure without applied bias. The Schottky barrier heights, the Fermi level energy and energies of deep levels are determined from experiments. A simplified scheme of carrier trapping and de-trapping is depicted in Figure (b,c). Scheme (b) is plotted for time 0.01 s after bias application. The carriers are injected from the contact into the bulk, where they are trapped at the deep levels. Scheme (c) shows the steady- state at 20 s after switching on the bias.
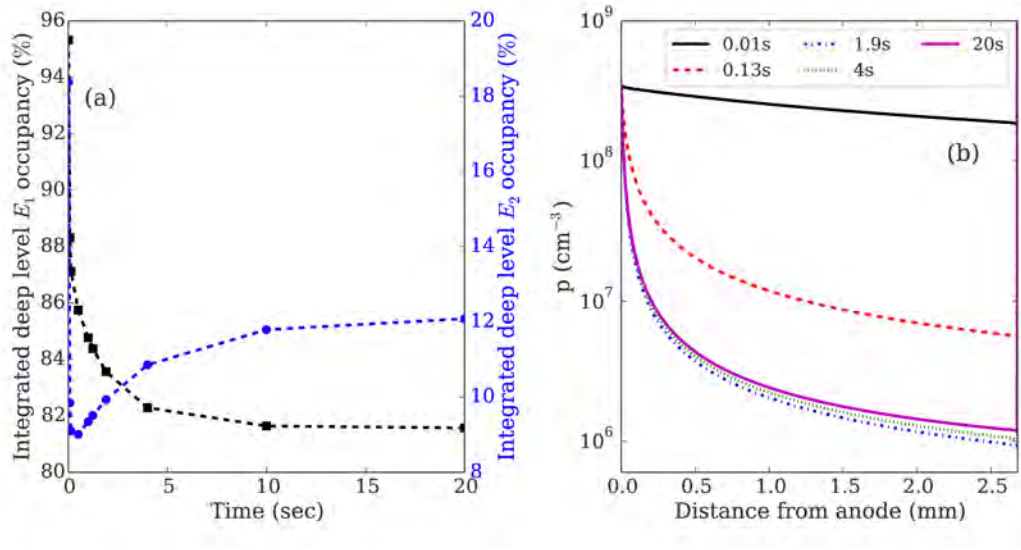
Figure 3.60: Graph (a) exhibits the integrated deep level occupancy for the deep level E_1 as back squares and for the deep level E_2 as blue circles. The distribution of free holes in the valence band is plotted in Graph (b).
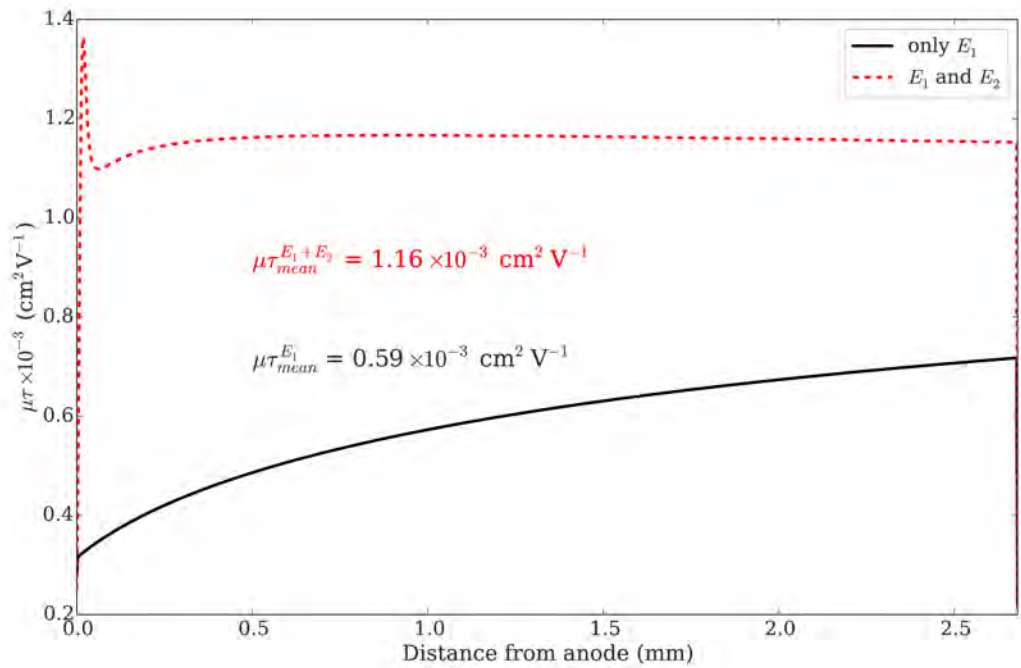
Figure 3.61: The profiles of the electron $\mu\tau$ product based on simulation with and without the deep level E_2.

Conclusion

This thesis is focused on the evaluation of deep levels that influence a charge transport in various CdTe based materials for the detection of high energy X-ray and gamma-ray radiation. Various methods were used to obtain a complex view of the sample properties.

At first, the spectroscopic ellipsometry measurements and I-V characteristics were measured on CdTe, CdZnTe, CdTeSe and CdZnTeSe samples. It was proven that the energy band-gap depends on the composition of the crystal as it was predicted. The samples resistivities were characterized, which also with assuming the sample energy band-gap allowed defining the Fermi level positions. It was observed that Au contact bends band upward at all high-resistivity samples. In case of CTS sample, the Au contact acts as an Ohmic contact. The In should bend band downward due to the model based on the difference of the work functions (Section 1.8). Although, the I-V measurement of CZTS demonstrates that the band is bent upward at In-CZTS interface. It should be induced by surface states. The results about samples energy band-gaps, resistivities, and Schottky barrier heights are summarized in Section 3.1.

The influence of the low-temperature annealing in ambient air on CdTe:In and CdTe:Cl samples, especially the effect on their surface and bulk properties, was studied (Section 3.2.1). The surface composition was characterized by ellipsometry measurements. The oxide layer thickness on the side surfaces of the detector increases after annealing which corresponds with a decrease of the leakage current. The bulk current also decreases after annealing as the leakage current, but in this case it is caused by increasing of Schottky barrier height. We conclude that low-temperature annealing can be used to improve metal-semiconductor interfaces.

The treatment of CZT sample by higher temperature and bias voltage induces a stable change of the electric field and the space charge distribution at room temperature. This process is reversible and the probable source of the behaviour is an electro-migration.

The deep levels in three samples responsible for the dynamics of the electric field were analyzed by a complex approach involving the optical and temporal and temperature measurements of the inner electric field using the electro-optic Pockles effect. A new approach of the evaluation of deep levels based on the time behaviour of the space charge is presented.

We observed the difference in steady-state space charge of CdZnTe and CdZnTeSe samples. The CZT samples exhibit the negative space charge, however, the CZTS sample indicates a positive space charge. This difference is related to the opposite band bends at In contact.

Another difference is that we detected only one deep level in the CZT sample responsible for the time evolution of the inner electric field. Whereas the CZTS sample contains two main deep levels close to the midgap responsible for the evolution of the electric field. It was demonstrated by different behaviour of the space charge evolution in time. We found a single exponential character of the space charge evolution in the case of CZT sample, on the other hand, the space charge evolution exhibits an overshoot in CZTS sample which can be

described by double exponential function. The hole deep level $E_t = E_v + 0.86$ eV is connected with the negative space charge in CZT. We detected the hole deep level $E_t = E_v + 0.83$ eV and the electron deep level $E_t = E_c - 0.85$ eV which is responsible for accumulation of the positive space charge and in CZTS. We observed the theoretically predicted energy shift of the second ionization level of the cadmium vacancy towards the conduction band in CZTS ($E_t = E_v + 0.83 = E_c - (E_G - 0.83) = E_c - 0.69$ eV) relative to CZT ($E_t = E_v + 0.77 = E_c - (E_G - 0.77) = E_c - 0.82$ eV).

The optically active deep level at $E_c - 1.10$ eV in CZT and at $E_c - 1.18$ eV in CZTS which is responsible for optically induced polarization was detected by infrared spectral scanning method. We assume that the observed energy shift is connected with the addition of Se into the matrix. Also, we demonstrate the possibility of the light induced depolarization of samples using the hole trap at $E_t = E_v + 0.83$ eV and $E_t = E_v + 0.77$ eV in case of CZTS and CZT, respectively.

Using numerical simulation, we proved that observed non-monotonic time evolution of the electric field distribution in CZT is caused by a space charge oscillation on a single hole trap. On the other hand, the simulations in the case of CZTS time evolution of the electric field and electrical current show presence of two main deep levels. One deep level acts as a recombination level, and one acts as a deep hole trap level. The hole trap increases the mobility-lifetime product of electrons by decreasing the concentration of free holes and, therefore, increases the electron occupancy of the deep recombination trap. We conclude that the deep levels in CZTS have a favorable structure for high electric-charge transport, which is critical for producing high-performance X-ray and gamma-ray detectors.

Bibliography

[1] R. Triboulet a P. Siffert. *CdTe and Related Compounds.* Elsevier, Amsterdam, 1.vyd. edition, 2010. ISBN 978-0-08-096513-0.

[2] Arnold Burger, Larry Franks, Ralph B. James, Michael Fiederle, Krishna C. Mandal, Ramesh M. Krishna, Rahmi O. Pak, a Mohammad A. Mannan. Characterization of high-resistivity CdTe and $Cd_{0.9}Zn_{0.1}Te$ crystals grown by Bridgman method for radiation detector applications. *Proceedings of the SPIE*, pages 92131L–, 2014. URL: `http://proceedings.spiedigitallibrary.org/proceeding.aspx?doi=10.1117/12.2063054`.

[3] T. Takahashi a S. Watanabe. Recent progress in CdTe and CdZnTe detectors. *IEEE Transactions on Nuclear Science*, 48(4):950–959, Aug 2001. ISSN 0018-9499.

[4] W. L. Rance, J. M. Burst, D. M. Meysing, C. A. Wolden, M. O. Reese, T. A. Gessert, W. K. Metzger, S. Garner, P. Cimo, a T. M. Barnes. 14%-efficient flexible CdTe solar cells on ultra-thin glass substrates. *Applied Physics Letters*, 104(14):143903, 2014. URL: `https://doi.org/10.1063/1.4870834`.

[5] Arnold Burger, Michael Groza, Yunlong Cui, Utpal N. Roy, Damian Hillman, Mike Guo, Longxia Li, Gomez W. Wright, a Ralph B. James. Development of portable CdZnTe spectrometers for remote sensing of signatures from nuclear materials. *physica status solidi (c)*, 2(5):1586–1591, 2005. URL: `https://onlinelibrary.wiley.com/doi/abs/10.1002/pssc.200460839`.

[6] Huy Q. Le, Justin L. Ducote, a Sabee Molloi. Radiation dose reduction using a CdZnTe-based computed tomography system: Comparison to flat-panel detectors. *Medical Physics*, 37(3):1225–1236, 2010. URL: `https://aapm.onlinelibrary.wiley.com/doi/abs/10.1118/1.3312435`.

[7] W. Akutagawa, K. Zanio, a J.W. Mayer. CdTe as a gamma detector. *Nuclear Instruments and Methods*, 55:383 – 385, 1967. ISSN 0029-554X. URL: `http://www.sciencedirect.com/science/article/pii/0029554X67901474`.

[8] P. Horodyský a P. Hlídek. Free-exciton absorption in bulk CdTe: temperature dependence. *physica status solidi (b)*, 243(2):494–501, 2006. ISSN 1521-3951.

[9] Glenn F. Knoll. *Radiation detection and measurement.* John Wiley, Hoboken, N.J., 4th ed edition, c2010. ISBN 04-701-3148-9.

[10] Makram Hage-Ali a Paul Siffert. Chapter 6 Growth Methods of CdTe Nuclear Detector Materials. *Semiconductors for Room Temperature Nuclear Detector Applications*, pages 219–257, 1995. URL: `https://linkinghub.elsevier.com/retrieve/pii/S0080878408627453`.

[11] H. L. Malm a M. Martini. Polarization Phenomena in CdTe Nuclear Radiation Detectors. *IEEE Transactions on Nuclear Science*, 21(1):322–330, Feb 1974. ISSN 0018-9499.

[12] Niraula, A Nakamura, T Aoki, Y Tomita, a Y Hatanaka. Stability issues of high-energy resolution diode type CdTe nuclear radiation detectors in a long-term operation. *Nuclear Instruments and Methods in Physics Research Section A: Accelerators, Spectrometers, Detectors and Associated Equipment*, 491(1-2):168–175, 2002. ISSN 01689002. URL: https://linkinghub.elsevier.com/retrieve/pii/S0168900202011750.

[13] R.B. James, T.E. Schlesinger, Jim Lund, a Michael Schieber. Chapter 9 $Cd_{1-x}Zn_xTe$ Spectrometers for Gamma and X-Ray Applications. *Semiconductors for Room Temperature Nuclear Detector Applications*, pages 335–381, 1995. URL: https://linkinghub.elsevier.com/retrieve/pii/S0080878408627489.

[14] T.E. Schlesinger, J.E. Toney, H. Yoon, E.Y. Lee, B.A. Brunett, L. Franks, a R.B. James. Cadmium zinc telluride and its use as a nuclear radiation detector material. *Materials Science & Engineering R*, 32(4-5):103–189, 2001.

[15] A. Tanaka, Y. Masa, S. Seto, a T. Kawasaki. Zinc and selenium co-doped CdTe substrates lattice matched to HgCdTe. *Journal of Crystal Growth*, 94(1):166 – 170, 1989. ISSN 0022-0248. URL: http://www.sciencedirect.com/science/article/pii/0022024889906155.

[16] Carl J. Johnson, Baars, a Randolph E. Longshore. Recent Progress In Lattice Matched Substrates For HgCdTe EPITAXY. *Proceedings SPIE 1106, Future Infrared Detector Materials*, pages 56–, 1989. URL: http://proceedings.spiedigitallibrary.org/proceeding.aspx?doi=10.1117/12.960629.

[17] KiHyun Kim, JinKi Hong, a SunUng Kim. Electrical properties of semi-insulating $CdTe_{0.9}Se_{0.1}$:Cl crystal and its surface preparation. *Journal of Crystal Growth*, 310(1):91 – 95, 2008. ISSN 0022-0248. URL: http://www.sciencedirect.com/science/article/pii/S0022024807008615.

[18] U. N. Roy, A. E. Bolotnikov, G. S. Camarda, Y. Cui, A. Hossain, K. Lee, W. Lee, R. Tappero, G. Yang, R. Gul, a R. B. James. High compositional homogeneity of $CdTe_xSe_{1-x}$ crystals grown by the Bridgman method. *APL Materials*, 3(2):026102, 2015. URL: https://doi.org/10.1063/1.4907250.

[19] U. N. Roy, E Bolotnikov. A, G.S. Camarda, Y. Cui, A. Hossain, K. Lee, W. Lee, R. Tappero, Ge Yang, Y. Cui, A. Burger, a R. B. James. Compositional homogeneity and X-ray topographic analyses of $CdTe_xSe_{1-x}$ grown by the vertical Bridgman technique. *Journal of Crystal Growth*, 411:34–37, 2015. ISSN 00220248.

[20] Thomas A. M. Fiducia, Budhika G. Mendis, Kexue Li, Chris R. M. Grovenor, Amit H. Munshi, Kurt Barth, Walajabad S. Sampath, Lewis D. Wright, Ali Abbas, Jake W. Bowers, a John M. Walls. Understanding the role of selenium in defect passivation for highly efficient selenium-alloyed cadmium telluride solar cells. *Nature Energy*, 4(6):504–511, 2019. ISSN 2058-7546.

[21] Y.V Bezsmolnyy. Comparative analysis of radiation-sensitive properties of detectors based on CdTe and $Cd_{1-X}Zn_xTe_{1-Y}Se_y$ single crystals grown by the vertical Bridgman technique. *Nuclear Instruments and Methods in Physics Research Section A: Accelerators, Spectrometers, Detectors and Associated Equipment*, 458(1):461 – 463, 2001. ISSN 0168-9002. Proc. of the 11th Internat. Workshop on Room Temperature Semiconductor X- and Gamma-Ray Detectors and Associated Electronics.

[22] Utpal N. Roy, Giuseppe S. Camarda, Yonggang Cui, Rubi Gul, Ge Yang, Anwar Hossain, Ralph B. James, Jakub Zázvorka, Václav Dědič, Jan Franc, Vincenzo Lordi, Joel B. Varley, Michael Fiederle, Arnold Burger, Larry Franks, Ralph B. James, a Stephen A. Payne. Crystal growth of CdZnTeSe (CZTS) gamma detectors. *Hard X-Ray, Gamma-Ray, and Neutron Detector Physics XIX*, pages 33–, 2018-1-15. URL: `https://spiedigitallibrary.org/conference-proceedings-of-spie/10392/2276955/Crystal-growth-of-CdZnTeSe-CZTS-gamma-detectors--a-promising/10.1117/12.2276955.full`.

[23] U. N. Roy, G. S. Camarda, Y. Cui, R. Gul, G. Yang, a R. B. James. Charge-transport properties of as-grown $Cd_{1-x}Zn_xTe_{1-y}Se_y$ by the traveling heater method. *AIP Advances*, 8(12):125015, 2018. URL: `https://doi.org/10.1063/1.5064373`.

[24] U. N. Roy, G. S. Camarda, Y. Cui, R. Gul, A. Hossain, G. Yang, J. Zázvorka, V. Dědič, J. Franc, a R. B. James. Role of selenium addition to CdZnTe matrix for room-temperature radiation detector applications. *Scientific Reports*, (1), 2019. ISSN 2045-2322. URL: `http://www.nature.com/articles/s41598-018-38188-w`.

[25] Christian-Albrechts-University of Kiel. `http://www.tf.uni-kiel.de/matwis/amat/semi_en/kap_5/backbone/r5_1_4.html`.

[26] R. Triboulet, G. Neu, a B. Fotouhi. Growth and characterization of the complete $Cd_{1-x}Zn_xTe$ alloy series. *Journal of Crystal Growth*, 65(1):262 – 269, 1983. ISSN 0022-0248. URL: `http://www.sciencedirect.com/science/article/pii/0022024883900581`.

[27] P. Cheuvart, U. El-Hanani, D. Schneider, a R. Triboulet. CdTe and CdZnTe crystal growth by horizontal bridgman technique. *Journal of Crystal Growth*, 101(1):270 – 274, 1990. ISSN 0022-0248. URL: `http://www.sciencedirect.com/science/article/pii/002202489090980Y`.

[28] M. Bruder, H.-J. Schwarz, R. Schmitt, H. Maier, a M.-O. Möller. Vertical Bridgman growth of $Cd_{1-y}Zn_yTe$ and characterization of substrates for use in $Hg_{1-x}Cd_xTe$ liquids phase epitaxy. *Journal of Crystal Growth*, 101(1):266 – 269, 1990. ISSN 0022-0248. URL: http://www.sciencedirect.com/science/article/pii/002202489090979U.

[29] R. B. Lauer a Ferd Williams. Photoelectronic Properties of Graded Composition Crystals of IIVI Semiconductors. *Journal of Applied Physics*, 42(7):2904–2910, 1971. URL: https://doi.org/10.1063/1.1660647.

[30] F. P. Doty, J. F. Butler, J. F. Schetzina, a K. A. Bowers. Properties of CdZnTe crystals grown by a high pressure Bridgman method. *Journal of Vacuum Science & Technology B: Microelectronics and Nanometer Structures Processing, Measurement, and Phenomena*, 10(4):1418–1422, 1992. URL: https://avs.scitation.org/doi/abs/10.1116/1.586264.

[31] H.L. Glass, A.J. Socha, C.L. Parfeniuk, a D.W. Bakken. Improvements in production of CdZnTe crystals grown by the Bridgman method. *Journal of Crystal Growth*, 184-185:1035 – 1038, 1998. ISSN 0022-0248. URL: http://www.sciencedirect.com/science/article/pii/S0022024898802169.

[32] K. Hecht. Zum Mechanismus des lichtelektrischen Primarstromes in isolierenden Kristallen. *Zeitschrift fur Physik*, vol. 77(3-4):235–245, 1932.

[33] Z. He. Review of the Shockley–Ramo theorem and its application in semiconductor gamma-ray detectors. *Nuclear Instruments and Methods in Physics Research Section A: Accelerators, Spectrometers, Detectors and Associated Equipment*, vol. 463(1-2):250–267, 2001.

[34] Š. Uxa, R. Grill, a E. Belas. Evaluation of the mobility-lifetime product in CdTe and CdZnTe detectors by the transient-current technique. *Journal of Applied Physics*, vol. 114(issue 9):094511–, 2013. URL: http://scitation.aip.org/content/aip/journal/jap/114/9/10.1063/1.4819891.

[35] R. Matz a M. Weidner. Charge collection efficiency and space charge formation in CdTe gamma and X-ray detectors. *Nuclear Instruments and Methods in Physics Research Section A: Accelerators, Spectrometers, Detectors and Associated Equipment*, vol. 406(issue 2):287–298, 1998.

[36] D. J. Friedman, I. Lindau, a W. E. Spicer. Noble-metal–CdTe interface formation. *Phys. Rev. B*, 37:731–739, Jan 1988. URL: https://link.aps.org/doi/10.1103/PhysRevB.37.731.

[37] Csaba Szeles. CdZnTe and CdTe materials for X-ray and gamma ray radiation detector applications. *physica status solidi (b)*, 241(3):783–790, 2004. URL: https://onlinelibrary.wiley.com/doi/abs/10.1002/pssb.200304296.

[38] J. M. Francou, K. Saminadayar, a J. L. Pautrat. Shallow donors in CdTe. *Phys. Rev. B*, 41:12035–12046, Jun 1990. URL: https://link.aps.org/doi/10.1103/PhysRevB.41.12035.

[39] A. Castaldini, A. Cavallini, B. Fraboni, P. Fernandez, a J. Piqueras. Deep energy levels in CdTe and CdZnTe. *Journal of Applied Physics*, vol. 83(issue 4):2121–2126, 1998. URL: `http://scitation.aip.org/content/aip/journal/jap/83/4/10.1063/1.366946`.

[40] L. C. Isett a Pranab K. Raychaudhuri. Deep levels in nCdTe. *Journal of Applied Physics*, 55(10):3605–3612, 1984. URL: `https://doi.org/10.1063/1.332960`.

[41] A. Zerrai a G. Bremond. Properties of the titanium related level in $Cd_{0.96}Zn_{0.04}Te$ crystals. *Journal of Applied Physics*, 84(10):5554–5559, 1998. URL: `https://doi.org/10.1063/1.367997`.

[42] R.E. Kremer a W.B. Leigh. Deep levels in CdTe. *Journal of Crystal Growth*, 86(1):490 – 496, 1988. ISSN 0022-0248. URL: `http://www.sciencedirect.com/science/article/pii/002202489090764C`.

[43] M. Fiederle, D. Ebling, C. Eiche, D.M. Hofmann, M. Salk, W. Stadler, K.W. Benz, a B.K. Meyer. Comparison of CdTe, $Cd_{0.9}Zn_{0.1}Te$ and $CdTe_{0.9}Se_{0.1}$ crystals: application for - and X-ray detectors. *Journal of Crystal Growth*, 138(1):529 – 533, 1994. ISSN 0022-0248. URL: `http://www.sciencedirect.com/science/article/pii/002202489490863X`.

[44] X Mathew. Photo-induced current transient spectroscopic study of the traps in CdTe. *Solar Energy Materials and Solar Cells*, 76(3):225–242, 2003-03-31. ISSN 09270248. URL: `https://linkinghub.elsevier.com/retrieve/pii/S0927024802002763`.

[45] J. Kubat, J. Franc, V. Dědič, E. Belas, P. Moravec, V. Babentsov, P. Höschl, a R. Grill. Photoconductivity Mapping of Semi-Insulating CdZnTe. *Nuclear Science, IEEE Transactions on*, 58(4):1953–1957, Aug 2011. ISSN 0018-9499.

[46] Raji Soundararajan, Kelvin G. Lynn, Salah Awadallah, Csaba Szeles, a Su-Huai Wei. Study of defect levels in CdTe using thermoelectric effect spectroscopy. *Journal of Electronic Materials*, 35(6):1333–1340, Jun 2006. ISSN 1543-186X. URL: `https://doi.org/10.1007/s11664-006-0264-0`.

[47] Z.C. Huang, E. Eissler, a C.R. Wie. Role of cadmium vacancy-related defects in CdTe nuclear detectors. *Nuclear Instruments and Methods in Physics Research Section B: Beam Interactions with Materials and Atoms*, 100(4):507 – 510, 1995. ISSN 0168-583X. URL: `http://www.sciencedirect.com/science/article/pii/0168583X95003665`.

[48] Cs. Szeles, Y. Y. Shan, K. G. Lynn, A. R. Moodenbaugh, a E. E. Eissler. Trapping properties of cadmium vacancies in $Cd_{1-x}Zn_xTe$. *Phys. Rev. B*, 55:6945–6949, Mar 1997. URL: `https://link.aps.org/doi/10.1103/PhysRevB.55.6945`.

[49] Nemanja Krsmanovic, Alan W. Hunt, Kelvin G. Lynn, Patrick J. Flint, Howard L. Glass, Ralph B. James, a Richard C. Schirato. Studies of

deep trapping levels in undoped and Sn-doped $Cd_{1-x}Zn_xTe$ by thermoelectric effect spectroscopy and thermally stimulated current. *Proceedings of SPIE*, 2000(4141):11–22, 2000. URL: `http://proceedings.spiedigitallibrary.org/proceeding.aspx?articleid=920279`.

[50] N. Krsmanovic, K. G. Lynn, M. H. Weber, R. Tjossem, Th. Gessmann, Cs. Szeles, E. E. Eissler, J. P. Flint, a H. L. Glass. Electrical compensation in CdTe and $Cd_{0.9}Zn_{0.1}Te$ by intrinsic defects. *Phys. Rev. B*, 62:R16279–R16282, Dec 2000. URL: `https://link.aps.org/doi/10.1103/PhysRevB.62.R16279`.

[51] V Dědič, J Franc, H Elhadidy, R Grill, E Belas, P Moravec, J Zázvorka, a P Höschl. Study of deep levels in high resistivity CdZnTe by discharge current measurement. *Journal of Instrumentation*, 8(01):C01008, 2013. URL: `http://stacks.iop.org/1748-0221/8/i=01/a=C01008`.

[52] J. Zázvorka, P. Hlídek, R. Grill, J. Franc, a E. Belas. Photoluminescence of CdTe:In the spectral range around 1.1eV. *Journal of Luminescence*, 177:71 – 81, 2016. ISSN 0022-2313. URL: `http://www.sciencedirect.com/science/article/pii/S0022231315300314`.

[53] E. Molva, J. L. Pautrat, K. Saminadayar, G. Milchberg, a N. Magnea. Acceptor states in CdTe and comparison with ZnTe. General trends. *Phys. Rev. B*, 30:3344–3354, Sep 1984. URL: `https://link.aps.org/doi/10.1103/PhysRevB.30.3344`.

[54] F. Molva, J. P. Chamonal, a J. L. Pautrat. Shallow Acceptors in Cadmium Telluride. *physica status solidi (b)*, 109(2):635–644, 1982. URL: `https://onlinelibrary.wiley.com/doi/abs/10.1002/pssb.2221090222`.

[55] D. M. Hofmann, P. Omling, H. G. Grimmeiss, B. K. Meyer, K. W. Benz, a D. Sinerius. Identification of the chlorine A center in CdTe. *Phys. Rev. B*, 45:6247–6250, Mar 1992. URL: `https://link.aps.org/doi/10.1103/PhysRevB.45.6247`.

[56] K. D. Tovstyuk, V. G. Deybuk, S. V. Melnichuk, a N. K. Tovstyuk. 3d-Impurity Levels in CdTe and ZnSe. *physica status solidi (b)*, 130(2):K153–K156, 1985. URL: `https://onlinelibrary.wiley.com/doi/abs/10.1002/pssb.2221300263`.

[57] E. Molva, K. Saminadayar, J.L. Pautrat, a E. Ligeon. Photoluminescence studies in N, P, As implanted cadmium telluride. *Solid State Communications*, 48(11):955 – 960, 1983. ISSN 0038-1098. URL: `http://www.sciencedirect.com/science/article/pii/0038109883905392`.

[58] A. Sarem, B.A. rlowski, a S. Kuźmiński. Surface Photovoltage Spectroscopy of $Cd_{0.97}Fe_{0.03}Se$ and $Cd_{0.97}Fe_{0.03}Te$ Crystals. *Acta Physica Polonica A*, 79(2-3):183–186, 1991. ISSN 0587-4246. URL: `http://przyrbwn.icm.edu.pl/APP/PDF/79/a079z2p06.pdf`.

[59] P. Moravec, M. Hage-Ali, L. Chibani, a P. Siffert. Deep levels in semi-insulating CdTe. *Materials Science and Engineering: B*, 16(1):223 – 227, 1993. ISSN 0921-5107. URL: `http://www.sciencedirect.com/science/article/pii/092151079390049S`.

[60] Chianping Ye a Joseph H. Chen. Studies of defects in n-type CdTe by charge transient spectroscopy. *Journal of Applied Physics*, 67(5):2475–2481, 1990. URL: `https://doi.org/10.1063/1.345497`.

[61] W. Jantsch, G. Brunthaler, a G. Hendorfer. Constant Photo-EPR: A New Method for Deep Level Characterization. In *Defects in Semiconductors 14*, volume 10 of *Materials Science Forum*, pages 515–520. Trans Tech Publications, 1 1986.

[62] V. Babentsov, V. Corregidor, J.L. Castano, M. Fiederle, T. Feltgen, K.W. Benz, a E. Dieguez. Compensation of CdTe by Doping With Gallium. *Crystal Research and Technology*, 36(6):535–542, 2001. URL: `https://onlinelibrary.wiley.com/doi/abs/10.1002/1521-4079%28200107%2936%3A6%3C535%3A%3AAID-CRAT535%3E3.0.CO%3B2-R`.

[63] V. Babentsov, J. Franc, E. Dieguez, M.V. Sochinskyi, a R.B. James. Unique Deep Level in Spectroscopic CdZnTe: Compensation, Trapping, and Polarization. *Nuclear Science, IEEE Transactions on*, 59(4):1531–1535, Aug 2012. ISSN 0018-9499.

[64] M. A. Berding. Annealing conditions for intrinsic CdTe. *Applied Physics Letters*, 74(4):552–554, 1999. URL: `https://doi.org/10.1063/1.123142`.

[65] Ido, A., R. Triboulet, a Y. Marfaing. Deep level structure and compensation mechanism in In-doped CdTe crystals. *Journal of Physics and Chemistry of Solids*, 48(9):781–790, 1987. ISSN 00223697. URL: `https://linkinghub.elsevier.com/retrieve/pii/002236978790028X`.

[66] J. E. Toney, B. A. Brunett, Schlesinger, E., F. P. Doty, a R. B. James. Optical and Electrical Characterization of Copper-and Chlorine-Doped Cadmium Zinc Telluride. *MRS Proceedings*, 487, 1997. ISSN 1946-4274. URL: `http://journals.cambridge.org/abstract_S1946427400233526`.

[67] F. Debbag, G. Bastide, a M. Rouzeyre. Thermal ionisation and photoionisation properties of deep traps in n-type CdTe. *Solid State Communications*, 67(1):1 – 5, 1988. ISSN 0038-1098. URL: `http://www.sciencedirect.com/science/article/pii/0038109888900026`.

[68] Yia-Chung Chang a Ralph B. James. Theoretical studies of Cd vacancies and vacancy-chlorine complexes in CdTe and $Cd1 - x Zn x Te$. pages 381–. URL: `http://proceedings.spiedigitallibrary.org/proceeding.aspx?doi=10.1117/12.366603`.

[69] K. H. Kim, A. E. Bolotinikov, G. S. Camarda, A. Hossain, R. Gul, G. Yang, Y. Cui, J. Prochazka, J. Franc, J. Hong, a R. B. James. Defect levels of semi-insulating CdMnTe:In crystals. *Journal of Applied Physics*, 109(11):113715, 2011. URL: `https://doi.org/10.1063/1.3594715`.

[70] S Sze a Kwok Kwok Ng. *Physics of semiconductor devices*. Wiley-Interscience, Hoboken, N.J., 3rd ed. edition, c2007. ISBN 978-0-471-14323-9.

[71] A.I.Anselm. *Úvod do teorie polovodičů*. Academia, 1967.

[72] H.Frank. *Fyzika a technika polovodičů*. SNTL, 1990.

[73] Peter Capper. *Properties of narrow gap cadmium-based compounds*. INSPEC, the Institution of Electrical Engineers, London, 1994 edition, 1994. ISBN 08-529-6880-9.

[74] W. Shockley a W. T. Read. Statistics of the Recombinations of Holes and Electrons. *Phys. Rev.*, 87:835–842, Sep 1952. URL: `https://link.aps.org/doi/10.1103/PhysRev.87.835`.

[75] R. N. Hall. Electron-Hole Recombination in Germanium. *Phys. Rev.*, 87:387–387, Jul 1952. URL: `https://link.aps.org/doi/10.1103/PhysRev.87.387`.

[76] J.Franc a P.Höschl. *Fyzika polovodi%vů pro optoelektroniku I, elektronické skriptum*. 2007. poslední úprava dne 11. ledna 2007. URL: `http://semiconductors.mff.cuni.cz/files/courses/Francskriptum.pdf`.

[77] Max Born a Emil Wolf. *Principles of optics*. Cambridge University Press, New York, 7th expanded ed edition, 1999. ISBN 05-216-4222-1.

[78] Eugene Hecht. *Optics*. Addison-Wesley, Reading, Mass., 4th ed edition, c2002. ISBN 978-080-5385-663.

[79] D. Bale a C. Szeles. Nature of polarization in wide-bandgap semiconductor detectors under high-flux irradiation. *Physical Review B*, vol. 77(issue 3):–, 2008. URL: `http://link.aps.org/doi/10.1103/PhysRevB.77.035205`.

[80] M. Strassburg, Ch. Schroeter, a P. Hackenschmied. CdTe/CZT under high flux irradiation. *Journal of Instrumentation*, vol. 6(issue 01):C01055–C01055, 2011-01-01. URL: `http://stacks.iop.org/1748-0221/6/i=01/a=C01055?key=crossref.8ae3c0cbcda95b40b4c7d652a1d233a5`.

[81] J. Franc, V. Dědič, J. Zázvorka, M. Hakl, R. Grill, a P. J. Sellin. Flux-dependent electric field changes in semi-insulating CdZnTe. *Journal of Physics D: Applied Physics*, vol. 46(issue 23):235306–, 2013-06-13. URL: `http://stacks.iop.org/0022-3727/46/i=23/a=235306?key=crossref.39e660462de02cc0a00abce9fda157c1`.

[82] A. Cola a I. Farella. The polarization mechanism in CdTe Schottky detectors. *Applied Physics Letters*, vol. 94(issue 10):102113–, 2009. URL: `http://scitation.aip.org/content/aip/journal/apl/94/10/10.1063/1.3099051`.

[83] R. T. Tung. Recent advances in Schottky barrier concepts. *Materials Science and Engineering: R: Reports*, 35(1–3):1 – 138, 2001. ISSN 0927-796X. URL: `http://www.sciencedirect.com/science/article/pii/S0927796X01000377`.

[84] R. T. Tung. The physics and chemistry of the Schottky barrier height. *Applied Physics Reviews*, 1(1):011304, 2014. URL: `https://doi.org/10.1063/1.4858400`.

[85] H.A. Bethe a Massachusetts Institute of Technology. Radiation Laboratory. *Theory of the Boundary Layer of Crystal Rectifiers*. Report (Massachusetts Institute of Technology. Radiation Laboratory). Radiation Laboratory, Massachusetts Institute of Technology, 1942. URL: `https://books.google.com/books?id=AGKTGwAACAAJ`.

[86] W. Schottky. Halbleitertheorie der Sperrschicht. *Die Naturwissenschaften*, 26(52):843–843, 1938. ISSN 0028-1042. URL: `http://link.springer.com/10.1007/BF01774216`.

[87] C.R. Crowell a S.M. Sze. Current transport in metal-semiconductor barriers. *Solid-State Electronics*, 9(11):1035 – 1048, 1966. ISSN 0038-1101. URL: `http://www.sciencedirect.com/science/article/pii/0038110166901274`.

[88] J. Zázvorka, J. Franc, P. Moravec, E. Jesenská, L. Šedivý, J. Ulrych, a K. Mašek. Contactless resistivity and photoconductivity correlation to surface preparation of CdZnTe. *Applied Surface Science*, 315:144 – 148, 2014. ISSN 0169-4332. URL: `http://www.sciencedirect.com/science/article/pii/S0169433214016328`.

[89] Jakub Pekárek, Eduard Belas, a Jakub Zázvorka. Long-Term Stable Surface Treatments on CdTe and CdZnTe Radiation Detectors. *Journal of Electronic Materials*, 46(4):1996–2002, Apr 2017. ISSN 1543-186X. URL: `https://doi.org/10.1007/s11664-016-5065-5`.

[90] J Zázvorka, P Hlídek, J Franc, J Pekárek, a R Grill. Photoluminescence study of surface treatment effects on detector-grade CdTe:In. *Semiconductor Science and Technology*, 31(2):025014, dec 2015. URL: `https://doi.org/10.1088%2F0268-1242%2F31%2F2%2F025014`.

[91] K. Nakazawa, K. Oonuki, T. Tanaka, Y. Kobayashi, K. Tamura, T. Mitani, G. Sato, S. Watanabe, T. Takahashi, R. Ohno, A. Kitajima, Y. Kuroda, a M. Onishi. Improvement of the CdTe diode detectors using a guard-ring electrode. *IEEE Transactions on Nuclear Science*, 51(4):1881–1885, Aug 2004. ISSN 0018-9499.

[92] A. E. Bolotnikov, C. M. H. Chen, W. R. Cook, F. A. Harrison, I. Kuvvetli, a S. M. Schindler. Effects of bulk and surface conductivity on the performance of CdZnTe pixel detectors. *IEEE Transactions on Nuclear Science*, 49(4):1941–1949, Aug 2002. ISSN 0018-9499.

[93] B.E.A.Saleh a M.C.Teich. *Základy fotoniky, svazek 2*. Matfyzpress, 1994. ISBN 80-85863-02-2.

[94] B.E.A.Saleh a M.C.Teich. *Základy fotoniky, svazek 4*. Matfyzpress, 1996. ISBN 80-85863-00-6.

[95] Susumu Namba. Electro-Optical Effect of Zincblende. *J. Opt. Soc. Am.*, 51(1):76–79, Jan 1961. URL: `http://www.osapublishing.org/abstract.cfm?URI=josa-51-1-76`.

[96] B.A. Paez. Thermoelectric Power and Hall Effect Measurements in Polycrystalline CdTe Thin Films. *physica status solidi (b)*, 220(1):221–225, 2000. ISSN 1521-3951.

[97] G. Badano, A. Million, B. Canava, P. Tran-Van, a A. Etcheberry. Fast Detection of Precipitates and Oxides on CdZnTe Surfaces by Spectroscopic Ellipsometry. *Journal of Electronic Materials*, 36(8):1077–1084, 2007. ISSN 1543-186X.

[98] J. Zázvorka, J. Franc, M. Statelov, J. Pekárek, M. Veis, P. Moravec, a K. Mašek. Optical and electrical study of CdZnTe surfaces passivated by KOH and NH$_4$F solutions. *Applied Surface Science*, 389:1214 – 1219, 2016. ISSN 0169-4332.

[99] Jakub Zázvorka, Jan Franc, Lukáš Beran, Pavel Moravec, Jakub Pekárek, a Martin Veis. Dynamics of native oxide growth on CdTe and CdZnTe X-ray and gamma-ray detectors. *Science and Technology of Advanced Materials*, 17(1):792–798, 2016. PMID: 27933118.

[100] M Rejhon, J Franc, V Dědič, J Kunc, a R Grill. Analysis of trapping and de-trapping in CdZnTe detectors by Pockels effect. *Journal of Physics D: Applied Physics*, vol. 49(issue 37):375101–, 2016-09-21. ISSN 0022-3727.

[101] M Rejhon, J Franc, J Zázvorka, V Dědič, a J Kunc. Influence of low-temperature annealing on Schottky barrier height and surface electrical properties of semi-insulating CdTe. *Semiconductor Science and Technology*, 32(8), 2017-08-01. ISSN 0268-1242. URL: `http://stacks.iop.org/0268-1242/32/i=8/a=085007?key=crossref.f137b4ec3fa95942bdd955c621c194c1`.

[102] M. Rejhon, V. Dědič, L. Beran, U. N. Roy, J. Franc, a R. B. James. Investigation of deep levels in CdZnTeSe crystal and their effect on the internal electric field of CdZnTeSe gamma-ray detector. *IEEE Transactions on Nuclear Science*, 66(8):1952–1958, Aug 2019. ISSN 0018-9499.

[103] J. Pousset, I. Farella, S. Gambino, a A. Cola. Subgap time of flight: A spectroscopic study of deep levels in semi-insulating CdTe:Cl. *Journal of Applied Physics*, 119(10), 2016.

[104] M. Pavesi, A. Santi, M. Bettelli, A. Zappettini, a M. Zanichelli. Electric Field Reconstruction and Transport Parameter Evaluation in CZT X-Ray Detectors. *IEEE Transactions on Nuclear Science*, 64(10):2706–2712, Oct 2017. ISSN 0018-9499.

[105] J. Franc, V. Deědič, P. J. Sellin, R. Grill, a P. Veeramani. Radiation induced control of electric field in Au/CdTe/In structures. *Applied Physics Letters*, vol. 98(issue 23):232115, 2011.

[106] A. Musiienko, R. Grill, P. Moravec, G. Korcsmáros, M. Rejhon, J. Pekárek, H. Elhadidy, L. Šedivý, a I. Vasylchenko. Dual-wavelength photo-Hall effect spectroscopy of deep levels in high resistive CdZnTe with negative differential photoconductivity. *Journal of Applied Physics*, 123(16):161502, 2018.

[107] Linjun Wang, Wenbin Sang, Weimin Shi, Yongbiao Qian, Jiahua Min, Donghua Liu, a Yiben Xia. Electrical properties of contacts on p-type $Cd_{0.8}Zn_{0.2}Te$ crystal surfaces. *Nuclear Instruments and Methods in Physics Research Section A: Accelerators, Spectrometers, Detectors and Associated Equipment*, 448(3):581 – 585, 2000. ISSN 0168-9002.

[108] Xiaoqin Wang, Wanqi Jie, Huanyong Li, Qiang Li, a Zewen Wang. Effects of low-temperature annealing on Ohmic contact of Au/p-CdZnTe. *Nuclear Instruments and Methods in Physics Research Section A: Accelerators, Spectrometers, Detectors and Associated Equipment*, 560(2):409 – 412, 2006. ISSN 0168-9002.

[109] Kaushik Chattopadhyay, X. Ma, Jean-Olivier Ndap, Arnold Burger, Tuviah E. Schlesinger, Corin M. R. Greaves, Howard L. Glass, J. P. Flint, Ralph B. James, a Richard C. Schirato. Thermal treatments of CdTe and CdZnTe detectors. *Proceedings of the society of photo-optical instrumentation engineers*, 4141:303–308, 2000.

[110] T Ozaki, Y Iwase, H Takamura, a M Ohmori. Thermal treatment of CdTe surfaces for radiation detectors. *Nuclear Instruments and Methods in Physics Research Section A: Accelerators, Spectrometers, Detectors and Associated Equipment*, 380(1):141 – 144, 1996. ISSN 0168-9002.

[111] S.H. Park, J.H. Ha, J.H. Lee, H.S. Kim, Y.H. Cho, a Y.K. Kim. Effect of Thermal Annealing on the Metal-Semiconductor Contact of a CZT Schottky Detector. *Journal of the Korean Physical Society*, vol. 55(issue 6):2378–, 2009-12-15. ISSN 0374-4884.

[112] K. H. Kim, S. Hwang, P. Fochuk, L. Nasi, A. Zappettini, A. E. Bolotnikov, a R. B. James. The Effect of Low-Temperature Annealing on a CdZnTe Detector. *IEEE Transactions on Nuclear Science*, 63(4):2278–2282, Aug 2016. ISSN 0018-9499.

[113] S. Mergui, M. Hage-Ali, J.M. Koebel, a P. Siffert. Thermal annealing of gold deposited contacts on high resistivity p-type CdTe nuclear detectors. *Nuclear Instruments and Methods in Physics Research Section A: Accelerators, Spectrometers, Detectors and Associated Equipment*, 322(3):375 – 380, 1992. ISSN 0168-9002.

[114] L. S. Hirsch, K. S. Ziemer, M. R. Richards-Babb, C. D. Stinespring, T. H. Myers, a Thierry Colin. The use of atomic hydrogen for low temperature oxide removal from HgCdTe. *Journal of Electronic Materials*, 27(6):651–656, 1998. ISSN 1543-186X.

[115] J.P. Häring, J. G. Werthen, R. H. Bube, L. Gulbrandsen, W. Jansen, a P. Luscher. Study of cleaved, oxidized, etched, and heattreated CdTe surfaces. *Journal of Vacuum Science & Technology A: Vacuum, Surfaces, and Films*, 1(3):1469–1472, 1983.

[116] M. K. Bahl, R. L. Watson, a K. J. Irgolic. Xray photoemission studies of tellurium and some of its compounds. *The Journal of Chemical Physics*, 66(12):5526–5535, 1977.

[117] V. Dědič, M. Rejhon, J. Franc, A. Musiienko, a R. Grill. Space charge oscillations in semiinsulating CdZnTe. *Applied Physics Letters*, 111(10):102104, 2017. URL: https://doi.org/10.1063/1.4986841.

[118] J. Franc, V. Deědič, M. Rejhon, J. Zázvorka, P. Praus, J. Touš, a P. J. Sellin. Control of electric field in CdZnTe radiation detectors by above-bandgap light. *Journal of Applied Physics*, 117(16):– , 2015. URL: http://scitation.aip.org/content/aip/journal/jap/117/16/10.1063/1.4919073.

[119] K. H. Kim, J. H. Choi, A. E. Bolotnikov, G. S. Camarda, A. Hossain, G. Yang, Y. Cui, a R. B. James. New insight into the 1.1-eV trap level in CdTe-based semiconductor. *Journal of the Korean Physical Society*, vol. 62(issue 4):623–627, 2013.

[120] Mao-Hua Du, Hiroyuki Takenaka, a David J. Singh. Carrier compensation in semi-insulating Cd Te. *Physical Review B*, 77(9):094122, 2008. ISSN 1098-0121.

[121] Joel B. Varley, Amit Samanta, a Vincenzo Lordi. Descriptor-Based Approach for the Prediction of Cation Vacancy Formation Energies and Transition Levels. *The Journal of Physical Chemistry Letters*, 8(20):5059–5063, 2017. PMID: 28961000.

[122] R. Grill, J. Franc, H. Elhadidy, E. Belas, Š. Uxa, M. Bugar, P. Moravec, a P. Hoschl. Theory of Deep Level Spectroscopy in Semi-Insulating CdTe. *IEEE Transactions on Nuclear Science*, 59(5):2383–2391, Oct 2012. ISSN 0018-9499.

[123] M. Rejhon, J. Franc, V. Deědič, J. Pekárek, U. N. Roy, R. Grill, a R. B. James. Influence of deep levels on the electrical transport properties of CdZnTeSe detectors. *Journal of Applied Physics*, 124(23):235702, 2018. URL: https://doi.org/10.1063/1.5063850.

List of Figures

List of Tables

List of Abbreviations

Greek symbols

α	absorption coefficient *p. 14*
$\boldsymbol{\eta}$	the dielectric impermeability tensor *p. 24*
$\mathfrak{r}$	Pockels coefficient tensor *p. 25*
$\mathfrak{s}$	Kerr coefficient tensor *p. 25*
$\boldsymbol{\varepsilon}$	the dielectric tensor *p. 24*
χ	electron affinity *p. 20*
Γ	the phase shift *p. 27*
γ_n	a coefficient of the electron capture probability *p. 14*
γ_p	a coefficient of the hole capture probability *p. 14*
κ	extinction coefficient *p. 37*
λ	wavelength *p. 14*
λ_0	wavelength *p. 28*
μ	carrier mobility *p. 5*
μ_e	electron mobility *p. 5*
μ_h	hole mobility *p. 5*
ν	photon frequency *p. 14*
ϕ	a scalar electrostatic potential *p. 11*
ϕ_{B0}	Schottky barrier height *p. 20*
ϕ_M	work function of metal *p. 20*
ϕ_S	work function of semiconductor *p. 20*
ρ	space charge density *p. 12*
σ	conductivity *p. 11*
σ_n	capture cross-section for electrons *p. 13*
σ_p	capture cross-section for holes *p. 13*
τ	lifetime of carriers *p. 5*
τ_n	lifetime of the free electrons *p. 14*

113

τ_p	lifetime of the free holes *p. 14*
ε	permittivity *p. 12*
ε_0	vacuum permittivity *p. 12*
ε_r	relative permittivity *p. 12*
ϱ	resistivity *p. 11*

Latin Symbols

$\mathbf{D}$	the electric displacement *p. 24*
$\mathbf{E}$	the electric field *p. 11*
$\mathbf{F}$	force *p. 11*
$\mathbf{j_e}$	the electron current density *p. 11*
$\mathbf{j_h}$	the hole current density *p. 11*
$\mathbf{j}$	the total current density *p. 11*
$\mathbf{v_d}$	carrier velocity *p. 5*
$\mathcal{E}$	intensity of the electric field *p. 5*
$\mathcal{E}_{\frac{\pi}{2}}$	half-wave electric field *p. 28*
$\mathcal{I}$	Light intensity *p. 14*
$\mathcal{L}$	carrier drift length *p. 5*
$\mathcal{T}$	the intensity transmittance *p. 27*
n	refractive index *p. 37*
W	the total energy of electron *p. 12*
A	area of the contact *p. 22*
a	lattice constant *p. 3*
A^*	Richardson constant *p. 22*
d	detector thickness *p. 5*
e	the elementary charge *p. 11*
E_c	the conduction band *p. 9*
E_F	Fermi energy *p. 9*
E_G	the band-gap *p. 9*
E_t	deep level *p. 13*

114

115

Abbreviation

CdTeSe	Cadmium Telluride Selenide *p. 35*
CdZnTe	Cadmium Zinc Telluride *p. 35*
CdZnTeSe	Cadmium Zinc Telluride Selenide *p. 35*
Cl	Chlorine *p. 35*
CTS	cadmium telluride selenide *p. 4*
CZT	cadmium zinc telluride *p. 3*
CZTS	cadmium zinc telluride selenide *p. 4*
DLTS	deep level transient spectroscopy *p. 7*
EMA	effective medium approximation *p. 37*
etc	et cetera *p. 8*
HPB	High Pressure Bridgman Method *p. 4*
HV	high voltage *p. 34*
In	Indium *p. 35*
LED	Light-Emitting Diode *p. 29*
PhC	photoconductivity *p. 7*
PICTS	photo-induced current transient spectroscopy *p. 7*
PL	photoluminescence spectroscopy *p. 7*
RMS	Root mean square *p. 35*
TEES	thermoelectric effect spectroscopy *p. 7*
THM	Travelling Heater Method *p. 4*
VGF	Vertical Gradient Freeze Method *p. 4*

List of Publications

Published

1. Kunc, J., Rejhon, M., Dědič, V., Bábor, P. *Thickness of sublimation grown SiC layers measured by scanning Raman spectroscopy* (2019) Journal of Alloys and Compounds, pp. 607-612.

2. Rejhon, M., Kunc, J. *ZO phonon of a buffer layer and Raman mapping of hydrogenated buffer on SiC(0001)* (2019) Journal of Raman Spectroscopy, 50 (3), pp. 465-473.

3. Rejhon, M., Franc, J., Dědič, V., Pekárek, J., Roy, U.N., Grill, R., James, R.B. *Influence of deep levels on the electrical transport properties of CdZn-TeSe detectors* (2018) Journal of Applied Physics, 124 (23), art. no. 235702,

4. Vozda, V., Burian, T., Chalupský, J., Dědič, V., Hájková, V., Hlídek, P., Juha, L., Kozlová, M., Krůs, M., Kunc, J., Rejhon, M., Vyšín, L., Rocca, J.J., Franc, J. *Micro-Raman mapping of surface changes induced by XUV laser radiation in cadmium telluride* (2018) Journal of Alloys and Compounds, 763, pp. 662-669.

5. Rejhon, M., Franc, J., Dědič, V., Hlídek, P., Kunc, J. *The electroluminescent properties based on bias polarity of the epitaxial graphene/aluminium SiC junction* (2018) Journal of Physics D: Applied Physics, 51 (26), art. no. 265104, .

6. Musiienko, A., Grill, R., Moravec, P., Korcsmáros, G., Rejhon, M., Pekárek, J., Elhadidy, H., Šedivý, L., Vasylchenko, I. *Dual-wavelength photo-Hall effect spectroscopy of deep levels in high resistive CdZnTe with negative differential photoconductivity* (2018) Journal of Applied Physics, 123 (16), art. no. 161502, .

7. Kunc, J., Rejhon, M., Hlídek, P *Hydrogen intercalation of epitaxial graphene and buffer layer probed by mid-infrared absorption and Raman spectroscopy* (2018) AIP Advances, 8 (4), art. no. 045015,.

8. Kunc, J., Rejhon, M., Belas, E., Dědič, V., Moravec, P., Franc, J. *Effect of Residual Gas Composition on Epitaxial Growth of Graphene on SiC* (2017) Physical Review Applied, 8 (4), art. no. 044011,.

9. Dědič, V., Rejhon, M., Franc, J., Musiienko, A., Grill, R. *Space charge oscillations in semiinsulating CdZnTe* (2017) Applied Physics Letters, 111 (10), art. no. 102104,.

10. Rejhon, M., Franc, J., Zázvorka, J., Dědič, V., Kunc, J. *Influence of low-temperature annealing on Schottky barrier height and surface electrical properties of semi-insulating CdTe* (2017) Semiconductor Science and Technology, 32 (8), art. no. 085007,.

11. Pekárek, J., Dědič, V., Franc, J., Belas, E., Rejhon, M., Moravec, P., Touš, J., Voltr, J. *Infrared LED enhanced spectroscopic CdZnTe detector working under high fluxes of X-rays* (2016) Sensors (Switzerland), 16 (10), art. no. 1591,.

12. Rejhon, M., Franc, J., Dědič, V., Kunc, J., Grill, R. *Analysis of trapping and de-trapping in CdZnTe detectors by Pockels effect* (2016) Journal of Physics D: Applied Physics, 49 (37), art. no. 375101,.

13. Dědič, V., Franc, J., Rejhon, M., Grill, R., Zázvorka, J., Sellin, P.J. *Depolarization of a CdZnTe radiation detector by pulsed infrared light* (2015) Applied Physics Letters, 107 (3), art. no. 032105,.

14. Franc, J., Dědič, V., Rejhon, M., Zázvorka, J., Praus, P., Touš, J., Sellin, P.J. *Control of electric field in CdZnTe radiation detectors by above-bandgap light* (2015) Journal of Applied Physics, 117 (16), art. no. 165702,.

15. Dědič, V., Zázvorka, J., Rejhon, M., Franc, J., Grill, R., Sellin, P.J. *Temporal and temperature evolution of electric field in CdTe:In radiation detectors* (2014) Journal of Applied Physics, 116 (5), art. no. 053702,.

16. Rejhon, M., Dědič, V., Beran, L., Roy, U.N., Franc, J., James, R.B. *Investigation of deep levels in CdZnTeSe crystal and their effect on the internal electric field of CdZnTeSe gamma-ray detector* (2019) IEEE Transactions on Nuclear Science, 66(8), pp 1952 - 1958

Comments

The list above is a summary of my publication during my studies. The list of publication can be split into two separate groups. The first group is focused on graphene physics (publications 1.,2.,5.,7.,8.). The second group consists of articles 3.,4.,6.,9.,10.,11.,12.,13.,14.,15.,16., deals with the CdTe material and its application as X-ray or gamma-ray detector. This thesis is based on the results from the second group publications.

Here, I would like to comment on my contribution to publications related to the thesis. I prepared the samples for publications no. 3., 4., 9., 10., 12., 13., 14., 15. and 16. I modified an experimental Pockels set-up and made the main measurements myself or I participated in measurements (publications no. 3., 9., 11., 12., 13., 14., 15. and 16.). I did ellipsometry measurements, I-V characteristics and photoconductivity measurements in publications 3., 6., 10., 12. and 16. I simulated the evolution of the electric field and electric current in publications no. 3. and 9. In the end, I participated in discussions about the results of our measurements with all co-authors.